

HARVARD UNIVERSITY
Graduate School of Arts and Sciences



DISSERTATION ACCEPTANCE CERTIFICATE

The undersigned, appointed by the

Harvard John A. Paulson School of Engineering and Applied Sciences

have examined a dissertation entitled:

“Experimental and Computational Study of Flapping-Wing Dynamics
and Locomotion in Aerial and Aquatic Environments”

presented by: Yufeng Chen

candidate for the degree of Doctor of Philosophy and here by
certify that it is worthy of acceptance.

Signature _____

A handwritten signature in black ink, appearing to read 'R. Wood', written over a horizontal line.

Typed name: Professor R. Wood

Signature _____

A handwritten signature in black ink, appearing to read 'L. Mahadevan', written over a horizontal line.

Typed name: Professor L. Mahadevan

Signature _____

A handwritten signature in black ink, appearing to read 'S. Rubinstein', written over a horizontal line.

Typed name: Professor S. Rubinstein

Date: April 27, 2017

Experimental and Computational Study of Flapping-Wing Dynamics and Locomotion in Aerial and Aquatic Environments

A dissertation presented

by

Yufeng Chen

to

The School of Engineering and Applied Sciences

in partial fulfillment of the requirements

for the degree of

Doctor of Philosophy

in the subject of

Engineering Sciences

Harvard University

Cambridge, Massachusetts

April 2017

©2017 - Yufeng Chen

All rights reserved.

Thesis advisor

Robert J. Wood

Author

Yufeng Chen

**Experimental and Computational Study of Flapping-Wing
Dynamics and Locomotion in Aerial and Aquatic Environments**

Abstract

Flapping-wing flight is ubiquitous among natural flyers. Flying insects can perform incredible acrobatic maneuvers, such as rapid turning, somersault, and collision avoidance in cluttered environments. Unlike fixed wing aircrafts or rotorcrafts, these tiny creatures utilize highly unsteady aerodynamic phenomena to achieve extraordinary locomotive abilities.

Taking inspiration from biological flappers, we develop a robot capable of insect-like flight, and then go beyond biological capabilities by demonstrating multi-phase locomotion and impulsive water-air transition. In this dissertation, we conduct experimental and computational studies of flapping wing aerodynamics that aim to quantify fluid-wing interactions and ultimately distill scaling rules for robotic design. Comparative studies of fluid-wing interactions in air and water reveal remarkable similarities, which lead to the development of the first hybrid aerial-aquatic flapping wing robot. Further, we show that microrobots face unique challenges and opportunities due to the dominance of surface tension at the millimeter scale. By developing an impulsive mechanism that utilizes an electrochemical reaction, we demonstrate the first-ever water to air takeoff in a microrobot.

Contents

Title Page	i
Abstract	iii
Table of Contents	iv
Acknowledgments	viii
1 Introduction	1
1.1 A brief history of flight	1
1.2 Aerodynamics	3
1.3 Flapping wing micro-aerial vehicles	7
1.4 Contributions and Chapter organization	9
1.5 Nomenclature and notation	11
2 Flapping experiments and experiment driven optimization	12
2.1 Introduction	12
2.2 Experimental setup	13
2.3 Wing driver	15
2.3.1 Wing shape parametrization	16
2.3.2 Wing hinge	17
2.4 Time-resolved force measurement	17
2.5 Digital particle velocimetry	19
2.6 Extraction of wing kinematics	20
2.6.1 Flapping kinematics	20
2.6.2 Laser-based tracking	23
2.6.3 Area-based tracking	24
2.6.4 Airframe-based tracking	25
2.6.5 Tracking method comparison	27
2.7 Proof-of-concept, experiment-driven optimization	28
3 The influence of wing inertia and morphology on aerodynamic performance	32
3.1 Introduction	32

3.2	Influence of wing inertia	34
3.3	Influence of wing aspect ratio	38
3.4	Influence of wing area moment	41
3.5	Influence of wing leading edge sweep ratio (LESR)	44
3.6	Wing-actuator pairing	47
3.7	Result and discussion	49
4	Wing hinge influence on aerodynamic performance	51
4.1	Introduction	51
4.2	Hinge endurance	52
4.2.1	Hinge design and manufacture	52
4.2.2	Hinge failure	54
4.2.3	Hinge endurance	56
4.3	A quasi-steady model of passive wing pitching	58
4.4	Results and discussion	61
4.4.1	Accuracy of the quasi-steady model	61
4.4.2	Influence of phase shift δ on lift	65
5	Numerical models of flapping flight	69
5.1	Introduction	69
5.2	The Navier Stokes equation	70
5.3	2D CFD models	72
5.3.1	2D simulation with fully prescribed kinematics	73
5.3.2	2D simulation with passive pitching	76
5.4	3D CFD models	77
5.4.1	3D simulation with fully prescribed kinematics	78
5.4.2	3D Simulation with passive pitching	80
5.5	Model comparison	80
5.5.1	Comparison of numerical models and experiments	81
5.5.2	Vorticity field comparison	85
5.5.3	Numerical simulation with passive hinge rotation	89
5.5.4	Effect of relative phase shift	90
6	Flapping propulsion in aquatic environment	95
6.1	Introduction	95
6.2	Scaling analysis of aerial and aquatic flapping	97
6.3	Numerical simulation of aerial and aquatic flapping	98
6.3.1	Aerial flapping versus aquatic flapping	99
6.4	Experiment and discussion	103
6.4.1	Experimental setup	103
6.4.2	Experimental comparison	103

7	A dynamical model for aquatic locomotion	108
7.1	Introduction	108
7.2	Robot dynamical model	109
7.2.1	Coordinate system definition	110
7.2.2	Rigid body dynamics	110
7.2.3	A time-varying aerodynamic model	116
7.2.4	Contribution from wing flexures and actuators	121
7.3	Simulation results	122
7.3.1	Symmetric flapping	122
7.3.2	Asymmetric flapping	124
7.3.3	Body-wing coupling	126
7.3.4	Frequency variation	128
7.4	Experimental result	132
7.4.1	Experimental setup	132
7.4.2	Robot kinematic tracking	132
7.4.3	Model comparison	134
8	A flapping wing, hybrid aerial-aquatic microrobot	137
8.1	Introduction	137
8.2	Robot design and fabrication	139
8.2.1	Gas collection chamber fabrication	141
8.2.2	Balance beam fabrication	143
8.2.3	Buoyant outrigger fabrication	143
8.2.4	Sparker plate fabrication	144
8.2.5	Robot assembly	148
8.3	Robot air-water transition	148
8.4	Robot water-air transition	150
8.4.1	Surface tension force on an emerging robot	151
8.4.2	Underwater gas collection	153
8.4.3	Robot stability near the water surface	155
8.4.4	Robot impulsive takeoff	156
8.4.5	Effect of micro-openings on takeoff	158
8.5	Landing and post-takeoff hovering	167
9	Conclusion	169
9.1	Summary	169
9.2	Fluid mechanical interactions between multiple wings	171
9.3	Multiple winged designs and microrobotic modularity	171
9.4	Novel microrobotic applications	173
9.5	Concluding remarks	173
	Bibliography	174

Contents

A Robot wing fabrication	189
B Validation of numerical solver	198

Acknowledgments

First and foremost, I would like to thank my adviser, Professor Robert Wood, for his exceptional guidance and support. Rob has been an encouraging and inspiring mentor, and he offers me tremendous freedom in my study and research. He helps me to create and develop my own research project, providing not only resources but also insightful ideas. Working in the microrobotics lab has been an extremely challenging and rewarding experience.

I also want to thank my colleagues in the microrobotics lab, both for academic collaboration and personal interactions. Specifically, I want to thank everyone in the RoboBee team: Professor Alexis Lussier Desbiens, Professor Nicholas Gravish, Professor Pakpong Chirarattananon, Dr. Kevin Ma, Dr. Zhi Teoh, Pierre Duhamel, and Farrell Helbling. I want to thank Farrell and Hongqiang for being amazing colleagues and friends; I cannot finish the explosion experiments without their help, support, and encouragement.

Lastly, I would like to thank my parents for providing me education, opportunity, and unconditional support over the past 27 years. I want to thank my twin brother Steven, who has been a roommate, a competitor, a colleague, and a lifelong friend. Finally, I want to thank my girlfriend Yishan. She has been extremely supportive and caring, and has proofread almost all of my writings.

Chapter 1

Introduction

1.1 A brief history of flight

In the course of 350 million years, natural flyers have developed stunning aerial agility and acrobatics. With an over 2-meter wingspan, a bald eagle (*Haliaeetus leucocephalus*) (figure 1.1a) can soar on rising air current at 60km/h. When chasing after a prey, this amazing animal retracts its wings and dives to reach 160km/h. On the other end of the spectrum, insects such as honey bees (*Apis mellifera*) (figure 1.1b) and fruit flies (*Drosophila melanogaster*) have millimeter scale wing span. Flapping their wings at over 100 wingbeats per second, these tiny creatures can navigate within cluttered environment and demonstrate extreme maneuvers [22].

The beauty and freedom of flying creatures have long inspired mankind to develop flying vehicles. In 1783, French paper mill owners, the Montgolfier brothers, invented the first hot air balloon (figure 1.1c) that reached a height of 1,800 meters. In the subsequent years, hydrogen or helium filled airships (figure 1.1d) were developed for

reconnaissance or freight transport. However, utilities of lighter-than-air vehicles are limited due to fundamental limitations on speed, cruise altitude, and cost of transport [80].

The first functional heavier-than-air vehicle drew inspiration from birds soaring but not flapping. On December 17, 1903, the Wright brothers demonstrated the first powered flight of a 338 kg aircraft for 260 meters. This historical moment marked the beginning the modern aeronautics and led to a number remarkable breakthroughs in the following century. Today, the world's newest fixed wing passenger jet, a Boeing 787-9 airliner (figure 1.1e), can carry 420 passengers and fly over an astonishing distance of 14,000 km at 900 km/h.

Aside from developing fixed wing aircraft, humans have invented rotorcraft vehicles that are capable of vertical takeoff and hover. On November 13, 1907, French inventor Paul Cornu demonstrated the first untethered helicopter takeoff. Despite the advantages in takeoff and landing, modern helicopters (figure 1.1f) have significantly lower cruise speed and payload capacities compared with fixed wing vehicles. To integrate favorable aerodynamic properties of fixed wing and rotorcraft vehicles into one design, aerospace engineers have developed tiltrotor aircraft (figure 1.1g) in recent years.

In the last decade there has been growing interest in developing micro aerial vehicles (MAV). Owing to advances in brushless motor fabrication, sensor and processor miniaturization, electrically powered autonomous aerial vehicles became accessible to the consumer market. To date, quadrotors (figure 1.1h) are the most mature and popular platform for recreation and research. These vehicles can hover stably, maneuver

in dynamical environments [89], or even collaborate with each other in a multi-agent system [4].

However, modern micro aerial vehicles are far less agile and robust compared to their biological counterparts. As we continue to miniaturize rotorcraft towards the realm of insects, frictional effects significantly decrease motor and transmission efficiency. Unsteady aerodynamics and high lift mechanisms, which have been utilized by small insects with ease, have not been employed by modern vehicles. Inspired by these natural flyers, a number of flapping-wing vehicles have been developed [20, 32, 55, 100] to emulate the bio-mechanics of insects and birds and investigate flapping wing aerodynamics. Figure 1.1i shows the 400 grams Festo Smartbird that has a wingspan of 2 meters. In contrast, the AeroVironment Nanohumming bird (figure 1.1j) is a significantly smaller flapping wing vehicle. With a 10 cm wingspan, the vehicle weighs 19 grams.

1.2 Aerodynamics

The foundation of aerodynamics lies within the field of fluid mechanics, which originated from the desire of improving British naval ship designs in the 17th century. In 1687, Sir Isaac Newton devoted an entire book of his famous Principia towards fluid mechanics. In the publication he derived the sine-squared law of momentum transfer, which was widely adopted but later proved inaccurate by Leonard Euler [3]. Around 1840, French physicist Claude-Louis Navier and British mathematician Sir George Stokes published the famous Navier-Stokes equation, which aimed to describe the viscous interaction between an object and surrounding fluid.



Figure 1.1: Example illustrations of natural and artificial flyers. (a) The bald eagle, a large natural flyer that soars on air current to generate lift. (source: Rolf Hicker, thinglink). (b) The honey bee, a small natural flyer that generates lift by flapping its wings (source: National Geographic). (c) Hot air balloon is the first lighter-than-air aerial vehicle (source: Todd Sarouhan, Costa Rica Travel). (d) A modern helium filled airship has limited cruise speed and altitude (source: Christian Michel). (e) Boeing 787-9 is the most recent commercial jet that can fly 14,000 km at 900 km/h (source: Boeing. Co). (f) A helicopter is capable of vertical liftoff and hover (source: Aircraft Temp). (g) Boeing V-22 is a tiltrotor aircraft that combines the aerodynamic advantages of fixed wing and rotorcraft vehicles (source: David Jacobson). (h) Quadrotors are today’s most mature and popular unmanned aerial platforms for research and recreation (source: DJI Co., Ltd). (i) Festo Smartbird is a flapping wing aerial vehicle with a wingspan of two meters [32]. (j) AeroVironment NanoHummingbird is a 19 gram flapping wing aerial vehicle with onboard sensors and battery [55].

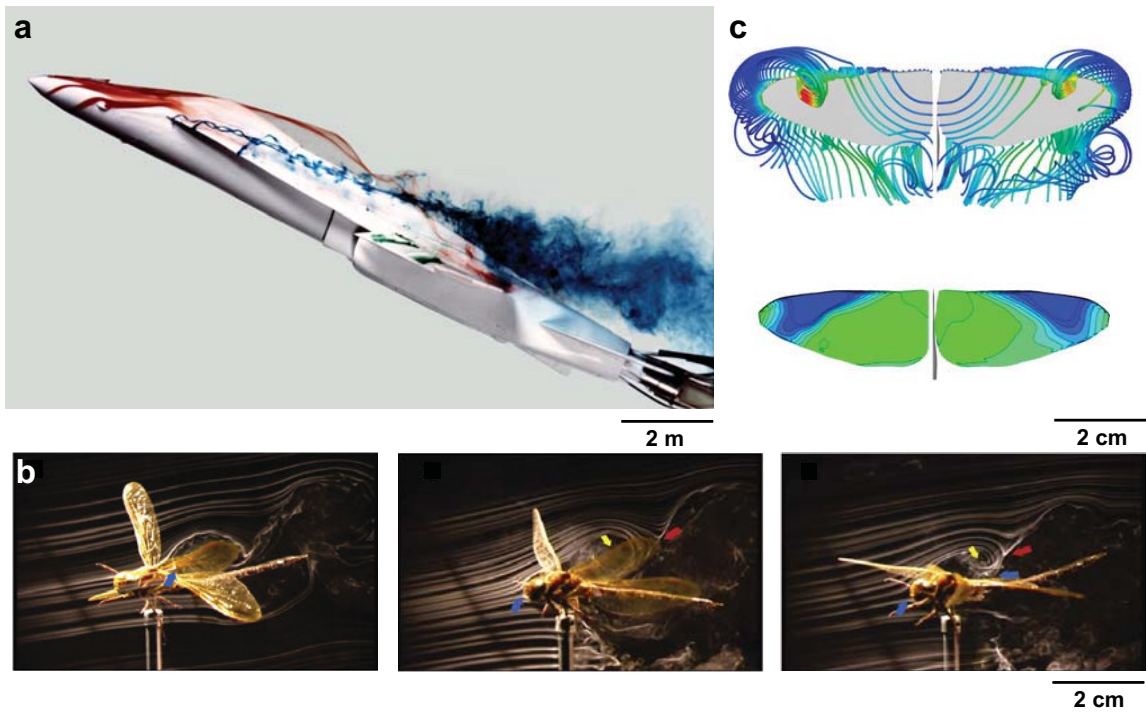


Figure 1.2: Examples of flow visualization and simulation. (a) Dye flow visualization of boundary layer detachment. In this experiment a F-18 fighter jet model is mounted at a large angle of attack [34]. (b) Streakline visualization of dragonfly flight vortex shredding [87]. (c) Simulated streamline and pressure profile on a pair of flapping hawkmoth wings [72].

In the 20th century, the development of aerial vehicles lead to remarkable progress in the field of aerodynamics. In 1902, German mathematician Martin Wilhelm Kutta and Russian scientist Nikolay Yegorovich Zhukovsky published Kutta-Joukowski circulation theorem, which relates inviscid, irrotational flow to lift force on a circular arc. This work laid the foundation for classical aerodynamics. In 1904, German physicist Ludwig Prandtl published boundary layer theory, which concerns the viscous effect on lift force generation and flow detachment (figure 1.2a). Based on these discoveries, thin airfoil theory was developed as a guideline for aerial vehicle designs. Today, the field of aerodynamics employs knowledge from classical fluid mechanics, thermodynamics, and mathematics to investigate flights that are supersonic, turbulent, or highly unsteady.

Flapping-wing flight is a common mode of insect locomotion which is characterized by complex and unsteady aerodynamic phenomena. As visualized in tethered [51] and untethered flight [35] measurements, the flow field around a flapping insect wing at intermediate Reynolds numbers ($50 \leq Re \leq 1000$) is highly unsteady and vortical. Figure 1.2b shows the unsteady flow generated by a tethered dragonfly [87]. Periodic flapping motion generates larger time-averaged lift and drag forces than those of an equivalent translating airfoil [58], suggesting that unsteady mechanisms are important to insect flight at small scales.

In several studies, [23, 24, 27] researchers have found that the most important feature of flapping flight involves the development of a strong leading edge vortex (LEV) during the wing translation phase. Figure 1.2c shows the simulated vortex structures and pressure profiles on a pair of flapping hawkmoth wings [72]. The LEV

corresponds to a low-pressure region on the wing upper surface, and it is responsible for the observed high lift. As shown in both experimental and computational studies [8, 93], the growth and shedding of the LEV is sensitive to the flapping kinematics. In addition, the interaction between shed vortices and a flapping airfoil significantly influences the flapping kinematics and dynamics [2]. Using a dynamically-scaled robotic wing, [24] Dickinson et al. (1999) characterized unsteady phenomena such as rotational circulation and delayed stall. Wang et al. [93] corroborated this observation through constructing and solving 2D computational fluid dynamics (CFD) models. Recent experimental studies [58] and computational work have focused on subtle phenomena such as LEV stability, wing–wing interactions, and 3D flow patterns [86]. Computationally intensive 3D CFD simulation [103] was developed to study unsteady 3D effects. Meanwhile, computationally inexpensive quasi-steady blade element [79] models were also proposed to explore how kinematic parameters influence maneuverability and flight stability [91] (Wang & Chang 2013).

1.3 Flapping wing micro-aerial vehicles

Advances in the understanding of flapping-wing aerodynamics, together with progress in fabrication technology and control theory, led to the design and successful flight of numerous flapping-wing micro-aerial-vehicles [55, 59, 65]. Among these artificial flyers, the Harvard RoboBee is the smallest, weighing merely 80 mg – comparable to that of a honey bee (*Apis Mellifera*). This robot utilizes two piezoelectric actuators that independently flap the wings at approximately 120 Hz. Although tethered for power, the RoboBee can demonstrate stable hovering flight through external



Figure 1.3: Novel RoboBee demonstrations. (a) A RoboBee perches on vertical surface through reinforcement learning. (b) A RoboBee sticks to a natural leaf through electrostatic adhesion. (c) A RoboBee swims in water. The functionalities demonstrated in (a), (b), and (c) are difficult to achieve in fixed wing aerial vehicles.

feedback. This work shows the exciting potential of future robotic insects in a variety of applications: assisted agriculture, search and rescue, and reconnaissance.

Owing to their small physical size and weight, robotic insects possess a number of abilities that are absent in larger flyers. Due to diminishing inertial forces at the millimeter scale, microrobots are more resilient to impact events such as crash landing or collision with obstacles. This advantage makes microrobots particularly suitable for navigating in cluttered or confined environments. Furthermore, microrobots can easily land on vertical surfaces [15] (figure 1.3a) or even perch on overhangs [42] (figure 1.3b) by exploiting substantial surface effects. This ability conserves energy and greatly extends MAVs' mission time.

Flapping-wing micro-aerial vehicles harness unsteady aerodynamics for lift and drag generation. Surprisingly, flapping-wing propulsion is also observed within aquatic species such as zooplankton [69]. Besides from being agile flyers, flapping-wing creatures are equivalently mobile swimmers. The underlying fluid mechanic connections between aerial and aquatic environments motivate us to explore the swimming capability of flapping-wing robotic insects [11] (figure 1.3c).

1.4 Contributions and Chapter organization

The goal of this dissertation is to investigate the underlying physical principles of flapping-wing flight and enable novel functionalities within flapping-wing micro-aerial vehicles. With the purpose of improving vehicle payload and efficiency, we integrate experimental and computational methods toward studying flapping-wing aerodynamics. We develop an automated, high-throughput experimental process that efficiently evaluates and analyzes flapping-wing kinematics and dynamics. The experimental results are further investigated by high fidelity numerical models, which aim to quantify fluid-structure interactions and ultimately distill new design rules. Comparative study of fluid-wing interactions in air and water shows remarkable similarities and leads to the development of the first hybrid aerial, aquatic flapping-wing robotic insect.

Chapter 2 describes an experimental approach towards studying flapping-wing flight kinematics and dynamics. We introduce the hardware setup and software implementation that enable concurrent measurements of flapping kinematics, dynamics, and the corresponding fluid flow. The collected data is incorporated into an experimental control loop for further optimization.

In Chapter 3, we experimentally quantify the influence of wing morphology and inertia on flapping-wing flight performance. Further, the experiments give rise to a scaling relationship between flapping frequency and wing size. Through improving wing inertia and morphology, we achieve a significant increase of robot payload.

In Chapter 4, we experimentally explore the relationship between wing hinge stiffness, passive pitching kinematics, and aerodynamic performance. We further

develop a simple quasi-steady model that estimates optimal wing hinge stiffness given desired flapping frequency. This study improves hinge lifespan and simplifies the wing characterization process.

Chapter 5 focuses on investigating flapping-wing fluid mechanics and interpreting the experimental results obtained in Chapter 4. We implement two dimensional (2D) and three dimensional (3D) numerical models to examine induced flow structures such as leading edge vortex and downwash. Comparison between numerical simulation, quasi-steady modeling, and experimental measurements identifies the strengths and weaknesses of each approach. The numerical studies elucidates the relationship between vortex strength, pitching dynamics, and wing hinge stiffness.

In Chapter 6, we explore the similarities of flapping-wing propulsion in aerial and aquatic environments. A frequency scaling analysis suggests fluid-wing interactions in air and water are characterized by similar Reynolds numbers. 3D computational fluid dynamical (CFD) simulations further predict nearly identical flow structures and passive pitching dynamics. These scaling and numerical predictions are corroborated by conducting single wing flapping experiments in air and water.

Whereas Chapter 6 focuses on the fluid mechanics of a single wing, Chapter 7 considers the dynamical properties of the entire robot. We develop a system level, time-varying model to investigate robot aquatic locomotion. Dynamical simulations and robot swimming experiments show strong body-wing coupling adversely influences vehicle upright stability. The robot becomes passively stable as flapping frequency increases, which further suggests the need to reduce wing area.

In Chapter 8, we demonstrate robot transitions between air and water. Microrobot

water entry and takeoff are difficult because surface tension force far exceeds robot weight. To achieve air-water transition, we coat the robot airframe with a surfactant to reduce surface tension. We further develop an impulsive takeoff method based on electrolysis and oxyhydrogen combustion reactions. Lightweight and multi-functional devices are designed and fabricated for electrolysis and detonation. This results in the first microrobot capable of aerial hovering, air-water transition, swimming, water surface takeoff, and landing.

We conclude with a discussion on ongoing research and future directions of flapping-wing vehicles. Towards achieving autonomous outdoor flight, micro-aerial vehicles need to integrate onboard sensors, power circuitry, and a battery. We propose novel structural configurations and designs that may lead to improvements in vehicle stability and aerodynamic efficiency.

1.5 Nomenclature and notation

Throughout this dissertation we adopt the following convention:

- Bold letters denote vector quantities and $\hat{\cdot}$ to denote unit vectors. $\mathbf{0}$ denotes a vector of all 0s. For the special unit vector that's parallel to a particular coordinate axis, we write the vector as \mathbf{e}_i without hat. It means the vector is 1 at the i^{th} entry and 0 everywhere else.
- Upper case letters represent matrix quantities. Specifically, R denotes a 3×3 rotation matrix.

Chapter 2

Flapping experiments and experiment driven optimization

2.1 Introduction

The aerodynamics of flapping-wing flight are inherently unsteady [60]. Both biological and robotic studies of lift generation by flapping-wings have highlighted several important lift-enhancing unsteady aerodynamic mechanisms such as a stable leading-edge vortex (LEV), added mass, wing-wing interactions, and wake capture (see [78] for a review). Modeling approaches based on the quasi-steady blade element method provide good estimates for the scaling of MAV flight metrics [97], but quasi-steady models can't account for unsteady aerodynamic phenomena which may be important in enhancing lift capacity or flight efficiency [29].

An alternative approach is to employ a high-throughput experiment in which many parameters can be systematically varied. This data-driven experimental approach can

enhance the design process for wing shape, material properties and stroke kinematics for which there may be a multitude of suitable operating points. Furthermore, with the ability to rapidly vary parameters we can use the outcomes of previous trials to inform future parameters, thus optimizing the experimental design.

In this chapter, we describe an experimental apparatus that facilitates rapid acquisition and analysis of data on MAV and insect wing performance. Specifically, we develop wing design algorithms and motion tracking methods that significantly improve data collection efficiency. The collected data for force, electrical power, resultant fluid flow, and wing kinematics are incorporated into an experimental control loop for parameter optimization. This high-throughput experimental apparatus enables detailed investigation on fluid structure interaction in subsequent chapters.

2.2 Experimental setup

We develop an experimental setup that commands flapping-wing motion and measures multiple aerodynamic metrics. The system mainly consists of a millimeter-scaled wing driver, capacitive force sensors, high speed cameras, a continuous-wave laser and an enclosing vacuum chamber. Figure 2.1a, c illustrate the overall experimental setup. Figure 2.1b, d show the configuration of wing driver and the force sensors. Besides from controlling flapping motion based on input test parameters, this apparatus measures flapping kinematics, instantaneous lift and drag forces, power expenditure, and induced fluid flow. In the following sections, we describe hardware fabrication and software implementation of each experimental component.

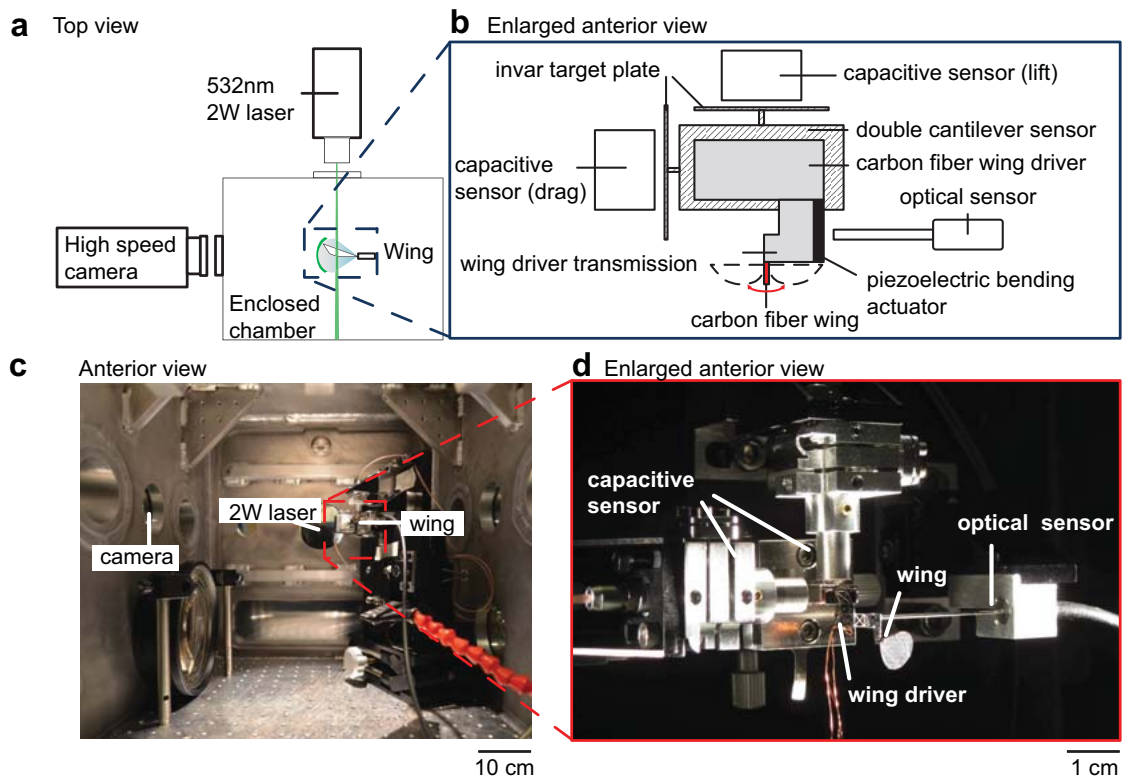


Figure 2.1: Illustration of the experimental setup. (a) Schematics of the experimental setup. The top view shows laser and camera placement with respect to the wing driver. (b) Schematics of the force sensors, the wing driver, and the optical sensor placement. (c) Photograph of the experimental set-up. (d) Photograph of the sensor and wing driver placements. These pictures correspond to the schematics in (a) and (b).

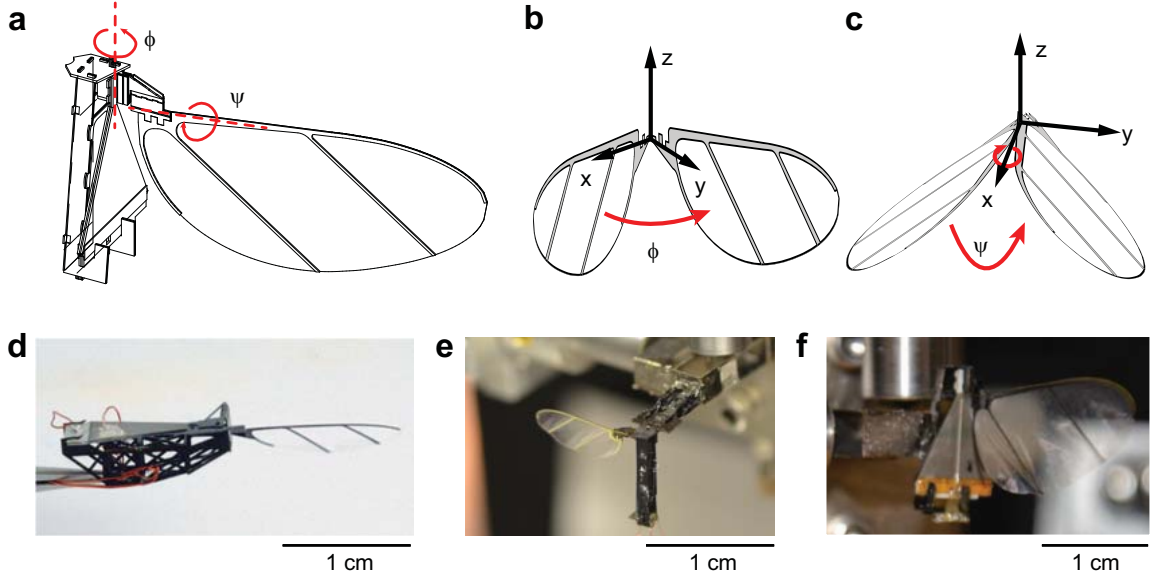


Figure 2.2: Flapping kinematics definition and wing drivers. (a) Illustration of the two rotational degrees of freedom. (b) Illustration of the wing stroke rotation. (c) Illustration of the wing pitch rotation. (d) An over-powered wing driver. (e) A RoboBee half. (f) A scaled up RoboBee half.

2.3 Wing driver

We perform flapping-wing experiments using a single active degree of freedom wing driver. Wing motion is actuated by a piezoelectric bimorph actuator which is coupled to the wing through a four-bar transmission. The piezoelectric actuator is configured in a simultaneous drive mode with both a bias and signal voltage controlled by a high-voltage amplifier. The signal voltage, $V(t)$, drives the piezoelectric motion and the constant bias voltage held at $V_{bias} = \max V(t)$, sets the offset position. In all experiments we set $V(t)$ to be sinusoidal with functional form $V(t) = V_A \sin(2\pi ft)$, where f is stroke frequency and V_A controls wing stroke amplitude.

Wings are attached to the driver through a slot that holds them in place during experiments but allows for easy removal and replacement. As shown in figure 2.2a,

the flapping motion has two degrees of freedom. Wings are actively rotated through a stroke angle, $\phi(t)$ (figure 2.2b). The pitching angle, $\psi(t)$ (figure 2.2c), is not actively controlled but instead rotates passively about the leading edge in response to inertial and aerodynamic loads.

Throughout our studies we use three different wing drivers (figure 2.2d-f) to investigate flapping flight. Figure 2.2d shows a custom designed wing driver with an oversized actuator. This wing driver can be approximated as an ideal displacement source that has negligible actuator-wing coupling. Alternatively, we also adapt flight worthy robots for dynamic measurements. As shown in figure 2.2e, f, half robots are mounted on the force sensor to characterize wing and wing hinge performance. We use a RoboBee half (figure 2.2e) to investigate wind disturbance influence on lift and drag production. We use a scaled RoboBee half (figure 2.2f) to investigate actuator and wing pairing.

2.3.1 Wing shape parametrization

The wing morphology design is based on Ellington’s study of insect wing shape parameterization [28]. An insect wing shape can be fully described using a physical scale, a dimensionless function, and two dimensionless numbers. The physical scale is often chosen to be the wing span. The dimensionless function prescribes the leading edge profile as a function of the spanwise coordinate r . The dimensionless parameters are the aspect ratio, the ratio between wing span and mean chord, and the second moment of area, \hat{r}_2 , that strongly correlates with the center of area \hat{r}_1 . Ellington showed that most insects have an \hat{r}_2 that falls in the range of 0.4 to 0.6, and utilizing

a quasi-steady model he further argued that lift is proportional to \hat{r}_2^2 . In this experiment, \hat{r}_2 is set to 0.55. Values of \hat{r}_2 higher than 0.6 lead to paddle-shaped wings which experience excessive deformation in flapping experiments.

The wings used in our experiments are made of carbon fiber frames and polyester membrane using the Smart Composite Microstructures processes [99]. We develop an automated design algorithm that significantly improve design efficiency and consistency. A detailed description of wing design and fabrication can be found in Appendix I. We explore wing morphology influence on flapping flight performance in Chapter 3.

2.3.2 Wing hinge

The RoboBee uses passive flexure hinges to generate pitch rotation during flapping. This process, inspired by the interplay of aerodynamic, inertial, and elastic forces that determine the motion of insect wings [6], reduces the number of actuators required to create the desired wing motion. The wing hinge stiffness has a large impact on wing pitching kinematics, which further influence lift and drag production. In Chapter 4, we discuss hinge stiffness influence on force production and the impact of hinge geometry on its lifetime.

2.4 Time-resolved force measurement

The wing driver is mounted on a dual-axis force sensor (figure 1b, d) that measures instantaneous lift and drag forces. The custom sensor consists of four parallel dual cantilever modules arranged in a series-parallel configuration. The structure

converts a load into displacements in the vertical and horizontal directions, and the displacements in both directions are measured by two (D-510.021, PISeca) capacitive sensors. We calibrate the sensors by hanging weights, and the sensitivities are found to be -84.6 and 85.5 V/mN for the lift and drag axes respectively.

In most experiments, we are mainly interested in comparing time-averaged lift and drag forces under different input parameters. In some experiments, we investigate effects of specific flow structures (leading edge or shed vortices) by comparing instantaneous force measurements. In those cases, the measured lift and drag signals are post-processed by a band pass filter to eliminate influence from actuator movement and sensor resonance. The filter range is determined by the flapping frequency. The wing inertial contribution is compensated by measuring the flapping kinematics. On the lift axis, the formula is given by

$$F_{aero} = ma_z - mg - F_{sensor}, \quad (2.1)$$

where a_z is the z-component of the wing inertial acceleration. We can compute a_z as

$$a_z = r_{com,z}(\cos(\psi)\dot{\psi}^2 + \sin(\psi)\ddot{\psi}), \quad (2.2)$$

where $r_{com,z}$ is the wing center of mass position in the vertical direction. Details of flapping kinematics and motion tracking are described in the section 2.6.

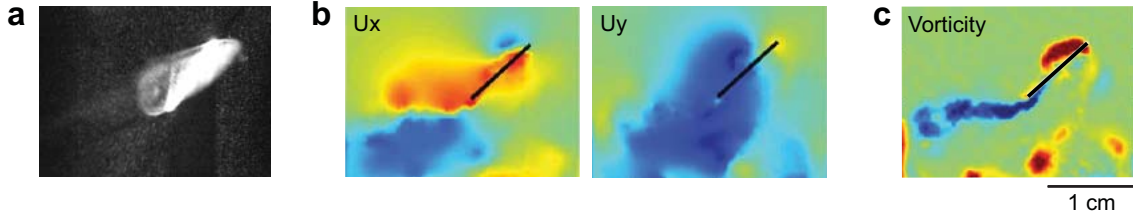


Figure 2.3: Particle velocimetry setup. (a) A sample flow image captured by the high speed camera. (b) Sample PIV images of the x, y components of the fluid velocity field. (c) The vorticity field corresponding to the velocity field in (b).

2.5 Digital particle velocimetry

Well-described fluid structures, such as leading and trailing edge vortices, are associated with aerodynamic force generation during flapping-wing flight. To observe these features, we measure the fluid flow surrounding the flapping-wing using digital PIV techniques [98].

Figure 2.3a illustrates the PIV setup. A 532 nm, 2 W laser sheet illuminates a vertical plane positioned at mid-wingspan, parallel to the camera image plane. The laser sheet allows for visualization of fluid flow along a two-dimensional plane. Image frame acquisition is triggered by the xPC target through digital pulses, so that frame acquisition and other sensor measurements are synchronized.

We capture 50 video frames per flapping period and repeat for 40 periods. The repetitive image frames are captured at the same phase within a period. Figure 2.3a shows a sample image captured by the high speed camera. For the set of replicate images with identical phase, we compute the median image and subtract it from each original image. This operation removes the wing from the original ones. The background images are further processed to obtain velocity and vorticity fields.

The velocity fields are determined from PIV by dividing an image into small

image patches on a square grid and registering the relative motion of objects in the image patches between times t and $t + \delta t$. Object motion between the time steps is determined by locating the peak of the cross-correlation between the images. We use a Fourier-based approach to compute the correlation peak between PIV images in a custom Matlab routine [33]. Figure 2.3b shows the x and y components of the velocity field. We further differentiate the velocity field to compute the vorticity field, which reveals important flow structures such as the leading and trailing edge vortices. Figure 2.3c shows a sample vorticity field.

2.6 Extraction of wing kinematics

2.6.1 Flapping kinematics

During hovering, insect wings typically have three degrees of freedom [29]. However, the motion that is normal to the stroke plane (i.e. ‘stroke plane deviation’) is usually very small. In our robotic design (figure 2.4a), we make the simplifying approximation that the kinematics of a flapping-wing has two degrees of freedom: stroke and hinge rotations (i.e. wing pitching).

As shown in figure 2.4b, the experimental measurement shows that the pitch motion is close to a pure sinusoid, where the amplitude of the second harmonic component is approximately 19% that of the fundamental harmonic. While this small but noticeable component does not have a large effect on force production, it offers interesting insight into the role of insect steering muscles. In a previous study, Dickson et al. measured the flapping kinematics of a flying *Drosophila* (figure 9 of Dickson, Straw

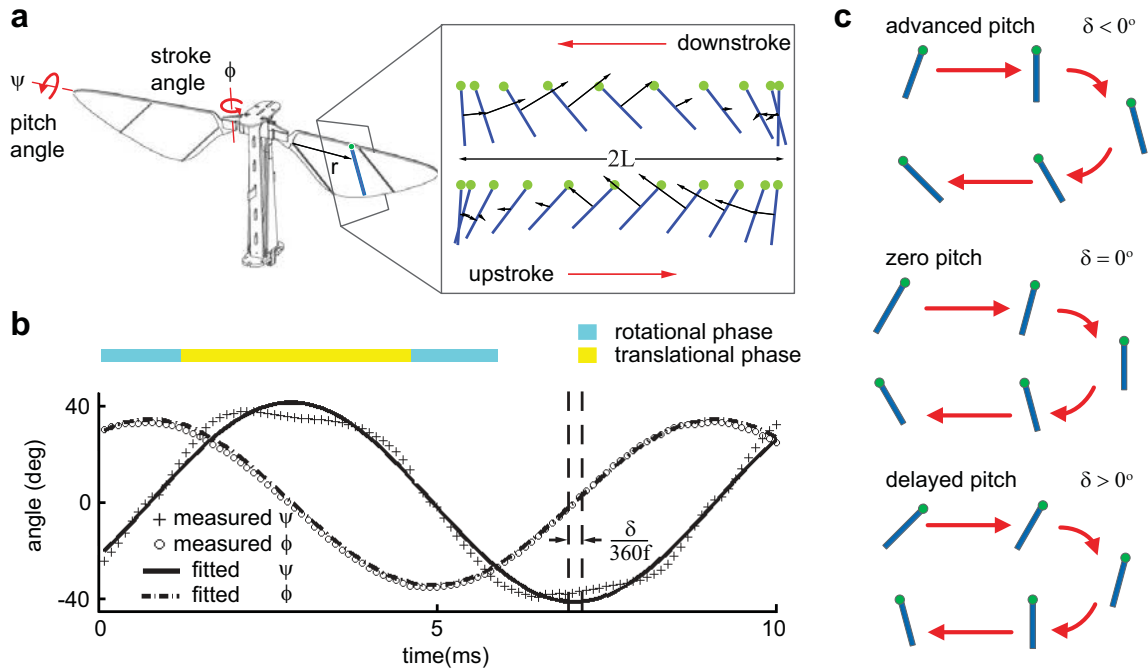


Figure 2.4: flapping-wing kinematics. (a) Wing stroke (ϕ) and hinge (ψ) motion. The motion of a thin rectangular segment along the wing chord is projected onto a 2D plane. (b) Experimental kinematics extraction shows that stroke and hinge motion are well approximated by pure sinusoids. A flapping period is broken down into translational (yellow) and rotational (blue) phases. (c) Passive wing pitch rotation is described by a phase shift parameter δ , with $\delta < 0^\circ$ corresponding to advanced pitch and $\delta > 0^\circ$ corresponding to delayed pitch.

& Dickinson [25]). In our experimental measurement, we observe similar stroke ($\phi(t)$) and pitch ($\psi(t)$) motion. In particular, $\psi(t)$ has noticeable flattened peaks in both measurements. This similarity implies that fruit fly steering muscles may function similarly to a linear torsional spring.

To the first order, we approximate the stroke and pitch motion as purely sinusoidal:

$$\begin{aligned} \phi &= \phi_{\max} \cos(2\pi ft) \\ \psi &= \psi_{\max} \sin(2\pi ft + \delta) \end{aligned}, \tag{2.3}$$

where ϕ_{\max} is the stroke amplitude, ψ_{\max} is the hinge amplitude, f is the flapping frequency and δ is the relative phase. Figure 2.4c illustrates that $\delta < 0^\circ$ corresponds to advanced pitch rotation and $\delta > 0^\circ$ corresponds to delayed pitch rotation. In quasi-steady blade element models and 2D CFD models, the angular stroke motion is approximated by the translational motion of a thin blade element located a distance r from the wing root. As shown in figure 2.4a, the amplitude of the wing chord translational motion is given by $L = r\phi_{\max}$.

As shown in figure 2.4b, the flapping period can be further decomposed into the translational phase and the rotational phase. The translational phase refers to the wing motion during midstroke at an approximately constant angle of attack. The rotational phase occurs during wing pitch reversal at the transition between down and up strokes.

Wing tracking has traditionally been done manually, or semi-manually where a user fits 3D wing model to video frames [28, 35, 62]. Our experimental setup gives rise to a number of simplifying assumptions that facilitate tracking. In the following

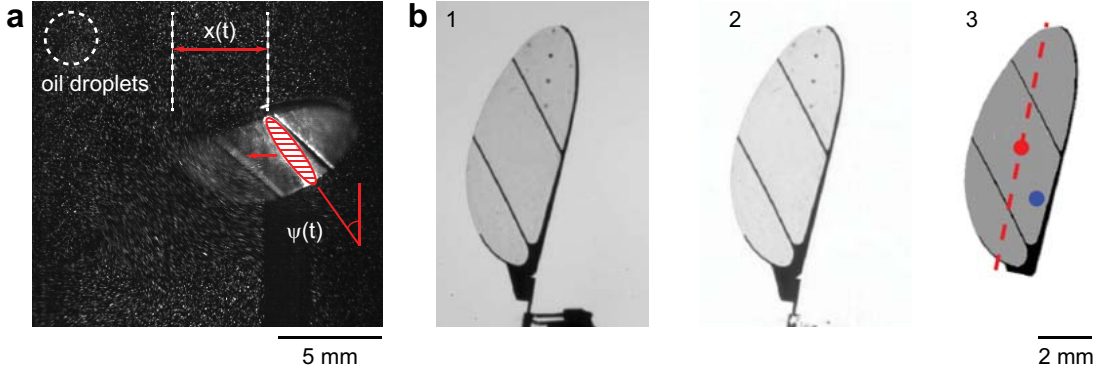


Figure 2.5: Laser-based and area-based tracking methods. (a) Wing kinematics tracking of $x(t)$ and $\psi(t)$ from a laser illuminated image. (b) Wing kinematics tracking through background thresholding (b-2) and wing root removal (b-3). (b-1) shows the original image captured by the camera.

sections, we describe a number of automated tracking methods that extract the kinematic parameters ϕ_{\max} , ψ_{\max} , and δ . In Chapters 3 and 4, we explore the relationship between flapping kinematics and dynamics.

2.6.2 Laser-based tracking

The PIV setup allows simultaneous flow measurements and wing kinematics tracking. In addition to revealing fluid flow, the laser sheet imaging system also illuminates a thin bright elliptical region of the wing (Figure 2.5a). By tracking the position and orientation of the wing-laser intersection we are able to track the wing stroke and hinge angle.

We track the wing stroke position along the sheet laser plane, $x(t)$, and the hinge angle projected along the laser plane, $\psi(t)$, with a custom automated image segmentation and tracking algorithm. The tracking algorithm segments the foreground image through a series of morphological operations. We first threshold the image, then per-

form morphological closing and opening operations to remove spurious points and fill holes in the wing region. In the foreground image, we locate all connected components and retain only the largest component which is the wing–laser intersection (the ellipse in figure 2.5a). In this setting, a connected component is defined as an isolated white region in a binary image where the background color is black. From the wing–laser intersection component we determine the wing centroid and orientation, $\psi(t)$. The horizontal distance of the wing leading edge from the wing root in the laser plane is $x(t)$ (figure 2.5a). From $x(t)$ we compute the wing stroke angle $\phi(t) = \arctan(x(t)/l_0)$, where l_0 is the distance from wing root to wing–laser intersection at $\phi = 0$.

2.6.3 Area-based tracking

This method measures wing stroke and pitch kinematics by tracking the projection of a wing on the camera image plane. Given an image sequence, the background is subtracted from every raw image (figure 2.5b-1, 2). Next, the wing area is extracted through thresholding. By pre-specifying the wing stroke axis location and its distance to the wing base, the algorithm can easily remove hinge and transmission from the image (figure 2.5b-3). Based on the post-processed image, the algorithm computes the wing area centroid, the wing spar centroid, and the wing principal axis (figure 2.5b-3). Orientation of the wing principal axis represents the stroke angle.

The wing pitch angle ψ is calculated by comparing the projected wing area to the original one. We let A_{cam} , A_W and A_{LE} denote the projected area on the image plane, the original wing area, and leading edge cross-sectional area. A_W and A_{LE} are manually specified for a given wing design. The projected area A_{cam} can be related

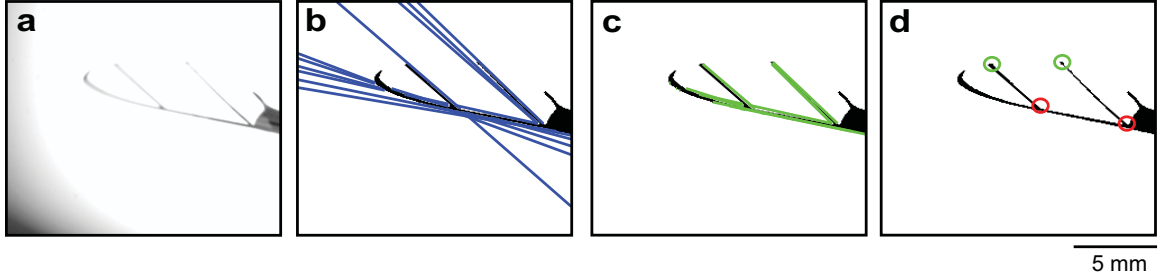


Figure 2.6: Airframe based tracking method. (a) The original image captured by the high speed video camera. (b) A hough transform detects line segments in the picture. (c) The endpoints of the Hough transformed lines are projected to the thresholded image. (d) Intersection points and endpoints are computed to identify wing leading edge points and trailing edge points.

to A_W , A_{LE} and ψ :

$$A_{cam} = A_W \sin \psi + A_{LE} \cos \psi. \quad (2.4)$$

Rearranging the preceding equation and approximating $\cos \psi$ as $\sqrt{A_W^2 - A_{cam}^2}/A_W$, the absolute value of the pitch angle can be expressed as:

$$\sin |\psi| = (A_{cam} - A_{LE} \frac{\sqrt{A_W^2 - A_{cam}^2}}{A_W}) \times \frac{1}{A_W}. \quad (2.5)$$

Finally, the sign of the pitch angle is resolved by comparing the wing leading edge centroid position to the wing area's centroid position (figure 2.5c).

2.6.4 Airframe-based tracking

This method measures wing stroke and pitch kinematics by tracking the wing airframe. Given a sequence of raw images (figure 2.6a), we first remove the background and threshold the image. Next, we compute the Hough transform of the binary image

to estimate major line segments. The blue lines in figure 2.6b show the lines found by Hough transform. These line segments terminate at the image border and may be skewed due to noise.

To track the leading edge spar and two diagonal wing spars, we project the endpoints of each Hough transformed line to the closest black pixel. The green lines in figure 2.6c show the Hough transformed lines after the endpoints are projected to the wing skeleton. These lines accurately represent the wing leading edge spar and diagonal spars. Finally, we compute the intersection of these lines and cluster the points to identify the spar intersections. The red circles in figure 2.6d show the computed intersection points. Finally, we locate the diagonal spar endpoints and label them as trailing edge points. These points are labeled green in figure 2.6d.

Knowing the wing geometry and having located the leading edge points (red) and trailing edge points (green), we can compute the kinematic parameter $\phi(t_i)$ and $\psi(t_i)$, where t_i represent the i^{th} frame. The rotation matrix from a standard reference frame to the current frame is given by:

$$\begin{pmatrix} x_1 \\ y_1 \\ z_1 \end{pmatrix} = \begin{pmatrix} \cos \phi & -\cos \psi \sin \phi & -\sin \psi \sin \phi \\ \sin \phi & \cos \psi \cos \phi & \sin \psi \sin \phi \\ 0 & -\sin \psi & \cos \psi \end{pmatrix} \begin{pmatrix} x_0 \\ y_0 \\ z_0 \end{pmatrix} \quad (2.6)$$

Here each tracked point gives (x_1, y_1) but does not provide depth information. We formulate a non-linear overdetermined system consisting of eight equations and two unknowns. This equation can be solved by numerical least squares methods.

2.6.5 Tracking method comparison

The kinematic tracking algorithms presented in the previous sections are designed for different experiments. In this section, we briefly compare method efficiency and accuracy.

The algorithm based on laser illumination allows simultaneous flow field measurement and wing tracking. Since the laser beam illuminates the wing cross-section in a dark background (figure 2.5a), it is straightforward to identify the wing chord and measure its position and orientation. Further, this method is computationally inexpensive. It is also robust to changes of wing designs because the local wing chord length has no effect on pitch or stroke angle tracking.

However, this method suffers a number of shortcomings. From an experimental perspective, it is inconvenient to operate a class-4 continuous waver laser in an open lab space. In addition, the laser beam must be carefully aligned to intersect the wing mid-span in every flapping experiment. Any manual misalignment introduces error in the stroke angle calculation. Finally, the tracking algorithm becomes less accurate at large stroke angles because the 2D laser plane is no longer orthogonal to the wing leading edge.

The algorithms based on wing area and airframe tracking require top view images instead of side views. Instead of using a bright laser beam, these setups use backlight illumination and capture the shadow projected onto the camera.

The method based on wing area tracking is the most accurate algorithm. However, this method requires meticulous adjustment to experiment lighting and manual calibration for each wing planform. The algorithm is computationally expensive because

it needs to compute the principal axes of multiple image segments. This method is suitable for experiments in which the planform remains unchanged. We will use this method for the study of wing hinge stiffness in Chapter 4.

The method based on wing airframe tracking has comparable accuracy and better robustness. This method does not need careful lighting adjustments because thresholding the wing membrane is no longer needed. By integrating the automated wing design algorithm, this tracking method can automatically adapt to wings of different morphologies. In addition, the algorithm implementation is carefully designed to avoid costly nonlinear calculations. Consequently, this method is seven times faster than the area based tracking method. Finally, this method can be easily generalized to multiple wings tracking in the same video. In Chapter 3, we use this method to study wing morphology influence on flapping performance.

2.7 Proof-of-concept, experiment-driven optimization

Our experimental apparatus allows efficient collection and analysis of flapping data. By integrating multiple simultaneous measurements of aerodynamic performance, we can perform analysis in near real-time, thus demonstrating unsupervised optimization.

To test the utility of our analysis-in-the-loop approach, we develop an optimization scheme to identify desired operational points for sinusoidal wing flapping during hovering. We implement a standard gradient descent algorithm which allows us to compare experimental optimization with theoretical predictions of performance. The

optimization statement can be defined as:

$$\begin{aligned} & \arg \min_{f, V_A} g(f, V_A) \\ & \text{s.t. } f \in [f_{\min}, f_{\max}] \quad , \\ & \quad V_A \in [V_{\min}, V_{\max}] \end{aligned} \quad (2.7)$$

where f and V_A are the driving frequency and voltage amplitude that are restricted to some set of safe operating conditions. The objective functions returns a scalar value based on input variables. The gradient descent routine is performed as follows: given an initial guess, we sample the vicinity of the starting position to compute local gradient

$$\nabla g = \begin{pmatrix} \frac{\partial g}{\partial f} \\ \frac{\partial g}{\partial V_A} \end{pmatrix}, \quad (2.8)$$

and then move in the gradient direction with step size δx . The local step size is inversely proportional to the norm of the local gradient, and it is restricted to a minimum value to reduce the number of steps taken. This algorithm terminates if $\|\delta x\|_2 < 1$. In our experiments, we find that the method converges after 4 – 15 steps. This method only finds local extrema, hence multiple runs are needed to search for the global maximum of a complex objective function. For each optimization attempt, we repeat the algorithm several times with different initial conditions.

Depending on the specific application, the objective function we aim to maximize varies. Classical choices include maximizing mean lift or mean lift to drag ratio, which correspond to maximizing vehicle payload or endurance. Additionally, in our set up, since it is difficult to quantify transmission loss, it may be advantageous to

minimize power input while satisfying a minimum mean lift threshold. As a first proof of principle for our analysis-in-the-loop method, we perform four optimization experiments allowing actuator voltage and frequency to vary: 1) maximize peak-to-peak drag force which is important for performing controlled flight maneuvers (figure 2.7a), 2) maximize mean lift force figure (2.7b), 3) maximize upstream suction velocity from PIV measurements (figure 2.7c), 4) seek an operating point which results in wing stroke amplitude of 40° , hinge amplitude of 17° , and stroke to stroke energy expenditure of 1 mJ (figure 2.7d).

The gradient descent optimization scheme to maximize drag force works well for a variety of initial conditions (Solid circles in figure 2.7a). Trajectories match our predictions (dashed lines in figure 2.7a) of a functional form $V_A f^2$ which is shown in the background of figure 2.7a. For lift optimization we choose a wing and actuation parameter range which has a non-trivial potential gradient with optimum lift occurring for intermediate actuation frequencies (figure 2.7b). All four trials converge to the correct frequency, however the first-order optimization routine is not robust enough to proceed to maximize amplitude. Near the maximum lift, the potential function is slowly varying along the direction of changing input voltage amplitude. The first-order routine does not converge to the local optimum due to discretization of the step size.

To validate PIV analysis-in-the-loop, we perform gradient descent optimization to maximize the suction velocity of the flapping wings. We find that six out of nine trials successfully converge to the optimum amplitude and frequency combination (figure 2.7c). Three trials which had initial conditions of high frequency and low amplitude do

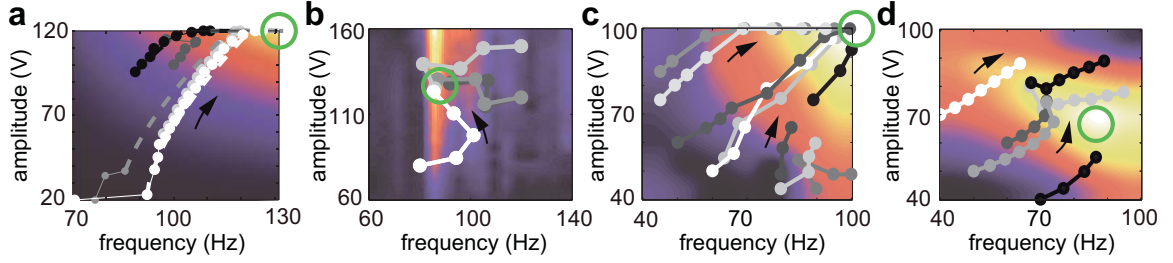


Figure 2.7: Optimization results for gradient descent to maximize peak drag force (a), maximize lift (b), maximize upstream fluid velocity (c), and tune for desired wing kinematics and power consumption set point (see text). Open green circles highlight desired maxima. Each circle represents an experiment and circle trajectories show the evolution of the optimization routine. Circles of different color correspond to different start points. Potential in (a) is generated from theoretical Af^2 function. Potential functions in (b-d) were generated in experiment, sampled in increments in 10 V and 10 Hz and interpolated.

not converge to the optimum (bottom right corner of figure 2.7c). Finally, we seek to determine the amplitude and frequency combinations which achieve wing kinematics of 40° stroke amplitude, 17° hinge amplitude, and which consume stroke-to-stroke energy of 1 mJ. This optimization routine incorporates synchronized high-speed video and actuator power measurements. All initial conditions converge towards the set point operating conditions (green circle in figure 2.7d), however optimization routines terminate early in the flat portion of the potential field near the maxima. This last example highlights the need to implement higher order optimization schemes.

In this chapter, we present an apparatus that can efficiently collect, analyze and optimize flapping-wing experiments. In the next chapter, we utilize this setup to investigate wing morphology influence on flapping performance.

Chapter 3

The influence of wing inertia and morphology on aerodynamic performance

3.1 Introduction

Recent advances in micro-fabrication technology and control methods have enabled a number of flapping-wing vehicles to achieve stable hovering flight [20, 55, 65]. However, achieving autonomous flight remains a difficult challenge for sub-gram micro-aerial vehicles. The Harvard RoboBee [65] is an 80 mg flapping wing robot that achieves hovering flight but relies on a tether to draw power from off-board amplifiers. A previous study aimed to increase payload capability by scaling up the actuator and wing size [66]. The scaled up RoboBee (figure 3.1) weighs 210 mg, has a wing span of 4.2 cm, and is capable of lifting 110 mg of payload. While this work al-

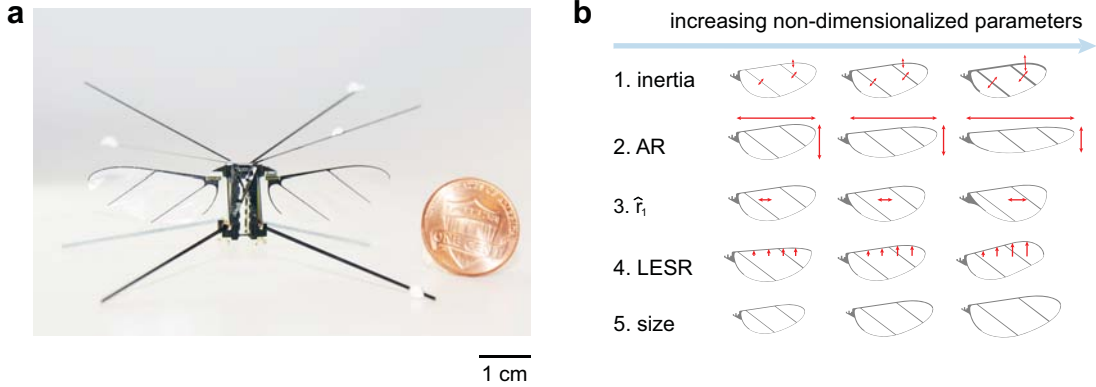


Figure 3.1: Wing driver platform and wing designs. (a) A recent RoboBee design weighing 210mg and capable of lifting 110mg of payload. (b) Illustration of different wing morphological and inertial parameters. (b-1) Change of wing spanwise and chordwise moment of inertia by varying spar thickness from 0.14mm to 0.29mm. (b-2) Change of aspect ratio AR from 3 to 5.5. (b-3) Change of spanwise first wing moment \hat{r}_1 from 0.49 to 0.55. (b-4) Change of leading edge sweep ratio ($LESR$) from 0.5 to 1.75. (b-5) Change of wing size from 94.5 mm^2 to 162 mm^2 .

lows the incorporation of onboard sensors and circuitry, the vehicle still cannot carry an onboard battery. Here we take an experimental approach towards improving the robot’s flapping performance and thus payload capacity.

Numerous previous studies on insect flight focus on either unsteady fluid mechanics [13, 24, 58] or influences of flapping kinematics [8, 21]. While these studies lead to useful design principles, most do not explore the influences of wing morphological and inertial parameter on flight performance. In this chapter, we study wing morphological and inertial parameter influence on flapping flight through designing and testing a suite of different wing and hinge pairs. We demonstrate that wing morphology has a large impact on lift enhancement and significantly changes the robot operating frequency. Through experimentation we improve the robot maximum mean lift by 37%, which is equivalent to approximately doubling the current payload capacity.

Wing properties	# 1	# 2	# 3	# 4	# 5	# 6
spar width (mm)	0.14	0.17	0.20	0.23	0.26	0.29
I_{xx} (mg·mm ²)	1.91	2.25	2.56	2.90	3.27	3.64
I_{zz} (mg·mm ²)	40.6	48.8	57.2	65.6	73.4	82.7

Table 3.1: Inertial properties of wings with different spar widths.

We adopt an existing setup for force measurement (figure 2.1) and kinematic tracking (figure 2.6). Further, we use one half of the scaled RoboBee as the wing driver (figure 2.2f). As discussed in Chapter 2, the wing morphology is fully prescribed by a physical scale R , a dimensionless function $y_{LE}(r)$, and two dimensionless quantities \hat{r}_1 and AR . The inertial parameters such as mass and moment of inertia can be changed by varying carbon fiber spar thicknesses. Figure 3.1 illustrates the parameters we modify. Figure 3.1b-1 shows how wing inertia can be changed by varying spar thickness. Figure 3.1b-2 shows how varying AR changes the wing spanwise to chordwise ratio. Figure 3.1b-3 shows how varying \hat{r}_1 shifts wing spanwise area moment toward the wing tip. Figure 3.1b-4 shows variation of the leading edge profile (LESR) by scaling it with a multiplicative factor in the range of 0.5 to 1.75. Finally, figure 3.1b-5 shows how we further vary wing size to investigate actuator-wing pairing. All wing design variations are scaled relative to the "baseline" wing design from a previous study [43].

3.2 Influence of wing inertia

In flapping-wing flight with passive pitching, stroke and pitch coupling is sensitively dependent on the effects of wing inertia [54, 59, 102]. We investigate the influence of wing inertia on system resonance by varying spar thickness while keeping

other morphological parameters constant. Table 3.1 shows the spar thickness, spanwise and chordwise moment of inertia of the wings used in experiments. The wing spanwise and chordwise inertia increase linearly as wing index increases. For each wing listed in table 3.1, we vary flapping frequency from 100 Hz to 140 Hz and driving voltage from 80 V to 150 V. To evaluate wing performance, we extract flapping kinematics, force measurements, and power consumption from each experiment.

While a previous study [97] predicts that a reduction of wing inertia improves performance, our result shows that the best performing wing does not have the minimum inertia. Wing spanwise and chordwise inertia affect stroke and pitch amplitude, which further affects lift production and power dissipation. Figure 3.2a shows the measured maximum lift from each wing. Figure 3.2b, c further show the corresponding driving frequency and power dissipation. Figure 3.2a shows that wing 4 generates the highest mean lift when driven at 140 Hz and the actuator consumes 23.1 mW power. Figure 3.2b shows that the flapping resonance decreases as wing inertia increases. Figure 3.2c shows that power dissipation decreases slightly as resonance frequency decreases. However, the drop in power dissipation is small compared to the reduction of mean lift.

The change of wing inertia also affects wing stroke and pitch motion. Figure 3.2d, e compare the experimentally measured wing stroke amplitude of wing 1 and wing 6. As the wing driver flaps a wing with small inertia, stroke amplitude varies slowly as driving frequency changes. This suggests that the wing driver behaves as a displacement source and the wing inertial contribution is small. As wing inertia increases, stroke amplitude varies noticeably as driving frequency changes. At higher

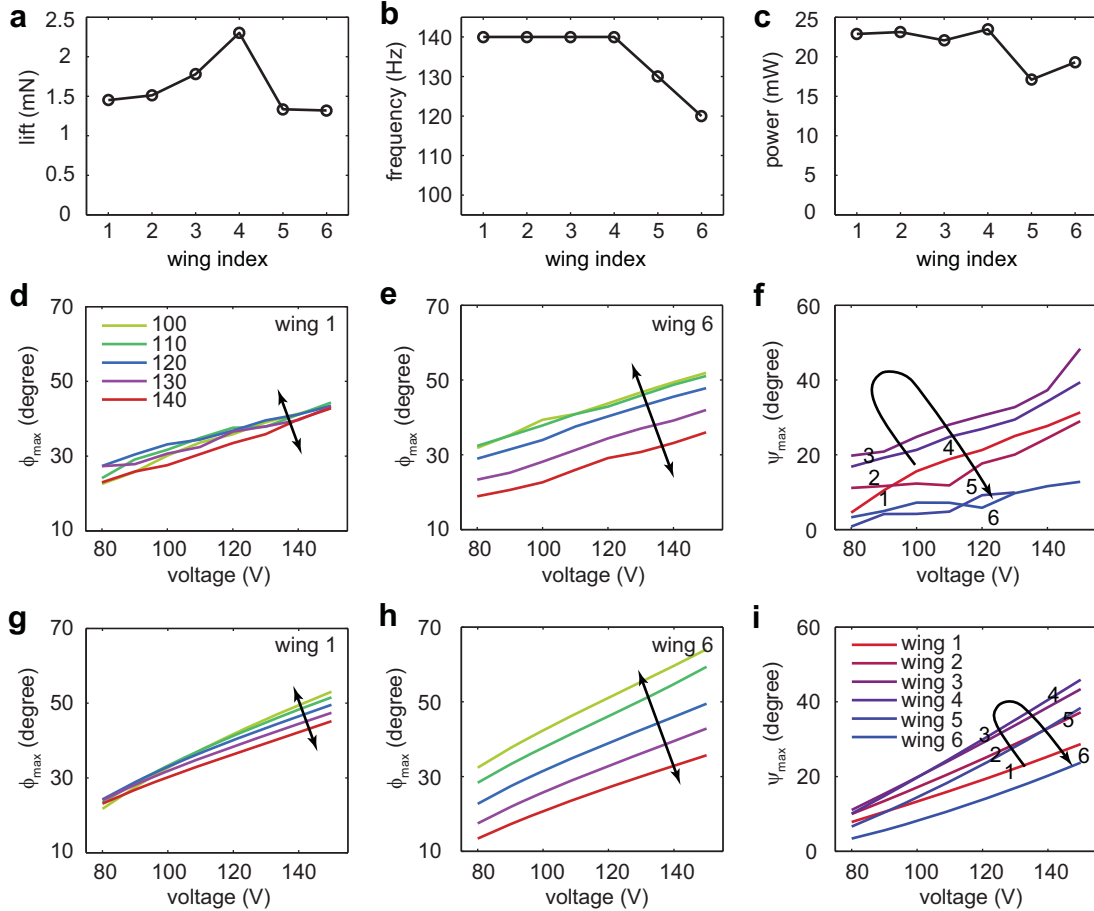


Figure 3.2: Wing inertia influence on aerodynamic performance, stroke and pitch kinematics. (a) Maximum mean lift versus wing number. (b) Driving frequencies at maximum mean lift versus wing number. (c) Power dissipation at maximum mean lift versus wing number. (d-e) Experimentally measured stroke amplitude ϕ_{\max} for the wings of smallest or largest spar width, respectively. (f) Experimentally measured pitch amplitude ψ_{\max} for all 6 wings at 140 Hz. (g-h) Simulated stroke amplitude ϕ_{\max} for the wings of smallest or largest spar width, respectively. (i) Simulated pitch amplitude ψ_{\max} for all 6 wings at 140 Hz. The arrows in (f) and (i) show maximum pitching is achieved at an intermediate wing inertia value.

driving frequencies, wing inertial effects become significant and consequently reduce stroke amplitude. Similarly, pitching kinematics also depend on wing inertia. Figure 3.2f shows the measured pitching amplitude ψ_{\max} for different wings when flapped at 140 Hz. The quasi-steady model estimates $C_L \propto \sin(2\alpha) = \cos(2\psi)$, which implies that mean lift directly correlates with pitching kinematics. While figure 3.2 shows that wing 4 generates the largest mean lift, figure 3.2a further illustrates that wing 4 has large pitch amplitude ψ_{\max} . Initially, ψ_{\max} increases as wing inertia increases, however ψ_{\max} falls sharply as wing inertia continues to increase.

We use a quasi-steady model to describe the wing inertia's effect on stroke and pitch coupling. We can formulate a system of coupled ordinary differential equations:

$$\begin{aligned} I_{zz}\ddot{\phi} + k_1\phi + F_D R_{\text{cop},x} &= F_{\text{act}} R_{\text{cop},x} \\ I_{xx}\ddot{\psi} + k_2\psi + d_2\dot{\psi} &= \tau_{\text{aero}} \end{aligned}, \quad (3.1)$$

where F_D is the drag force, τ_{aero} is the spanwise fluid torque, and F_{act} is the actuator input. Here we invoke the formula:

$$\begin{aligned} F_D &= (1.4 - \cos(2\alpha))b_1|\dot{\phi}|\dot{\phi} \\ \tau_{\text{aero}} &= b_2|\dot{\phi}|\dot{\phi}R_{\text{cop},z} \\ F_{\text{act}} &= F_a \cos(2\pi ft) \end{aligned}, \quad (3.2)$$

where $\alpha = \frac{\pi}{2} - \psi$ is the angle of attack. $R_{\text{cop},x}$ and $R_{\text{cop},z}$ are the x and z components of the center of pressure. We approximate $R_{\text{cop},x}$ using the first moment of wing shape:

$$R_{\text{cop},x} = \hat{r}_1 R. \quad (3.3)$$

From a previous study we found that $R_{\text{cop},z}$ is a strong function of α [10]. We approximate $R_{\text{cop},z}$ using a sigmoid function:

$$R_{\text{cop},z} = \left(0.25 + \frac{0.25}{1 + \exp\left(5 \times \left(1 - \frac{4}{\pi}\alpha\right)\right)}\right)\bar{c}. \quad (3.4)$$

Here we scale the sigmoid function such that we recover the thin airfoil limit at small α and the symmetric condition at $\alpha = \frac{\pi}{2}$. The coefficients b_1 , b_2 , k_1 , k_2 , d_2 , and F_a are manually adjusted to fit the measured data. This simple model intends to investigate the trend of inertia influence on flapping performance. It ignores unsteady effects such as added mass, wake capture, and rotational acceleration because in passive pitching simulations these extra terms may lead to excessive over-fitting. Here we use the model to demonstrate how the trend observed in Figure 3.2d-f is caused by stroke and pitch coupling. Figure 3.2g, h show the simulated stroke amplitude for wings 1 and 6. Similar to figure 3.2d, e, we observe that the stroke amplitude varies slowly with frequency for a low inertia wing and varies rapidly for a high inertia wing. Figure 3.2i shows simulated pitch kinematics of each wing when driven at 140Hz. Compared to figure 3.2f, we observe a similar trend in that a wing with intermediate moment of inertia has the maximum pitch amplitude.

3.3 Influence of wing aspect ratio

We investigate the influence of wing aspect ratio AR by varying this parameter while keeping wing area and spar thickness constant. Figure 3.3a shows the maximum mean lift as a function of AR . Figure 3.3b, c show the corresponding driving frequency

and power dissipation. We observe decreasing maximum mean lift and resonance frequency as AR increases. The maximum mean lift of the wing with $AR = 3$ is slightly lower than $AR = 3.5$ because its resonance frequency is expected to be higher than 140 Hz. At the highest driving frequency and voltage (140 Hz and 150 V), the pitch magnitude is 36° . We expect ψ_{\max} to continue to increase at higher driving frequencies. Consequently, we expect the maximum mean lift of the wing to be the highest for the wing with smallest AR .

The reduction of resonance frequency at large AR is partially contributed by the increase of wing chordwise moment of inertia. As wing aspect ratio increases, wing radius R increases and mean chord \bar{c} decreases. Consequently, the chordwise moment of inertia I_{zz} increases and the spanwise moment of inertia I_{xx} decreases. Figure 3.3d shows I_{zz} and I_{xx} as functions of AR . In section 3.2, both experimental results and the simplified quasi-steady model demonstrate that increasing wing inertia decreases wing resonance. Here we observe that the increase in AR increases I_{zz} , which affects the resonance of the wing stroke motion. Consequently, a wing with larger AR has a lower resonance frequency.

Further, wing structural stiffness decreases rapidly as AR increases. To first order, the wing bending stiffness can be modeled as that of a cantilever beam:

$$K = \frac{3EI_{zz}}{R^3}, \quad (3.5)$$

where E is the Young's modulus of carbon fiber and R is wing span. An increase of AR implies an increase of wing span R , and consequently leads to reduction of stiffness K . In addition, the quasi-steady model predicts a quadratic increase of

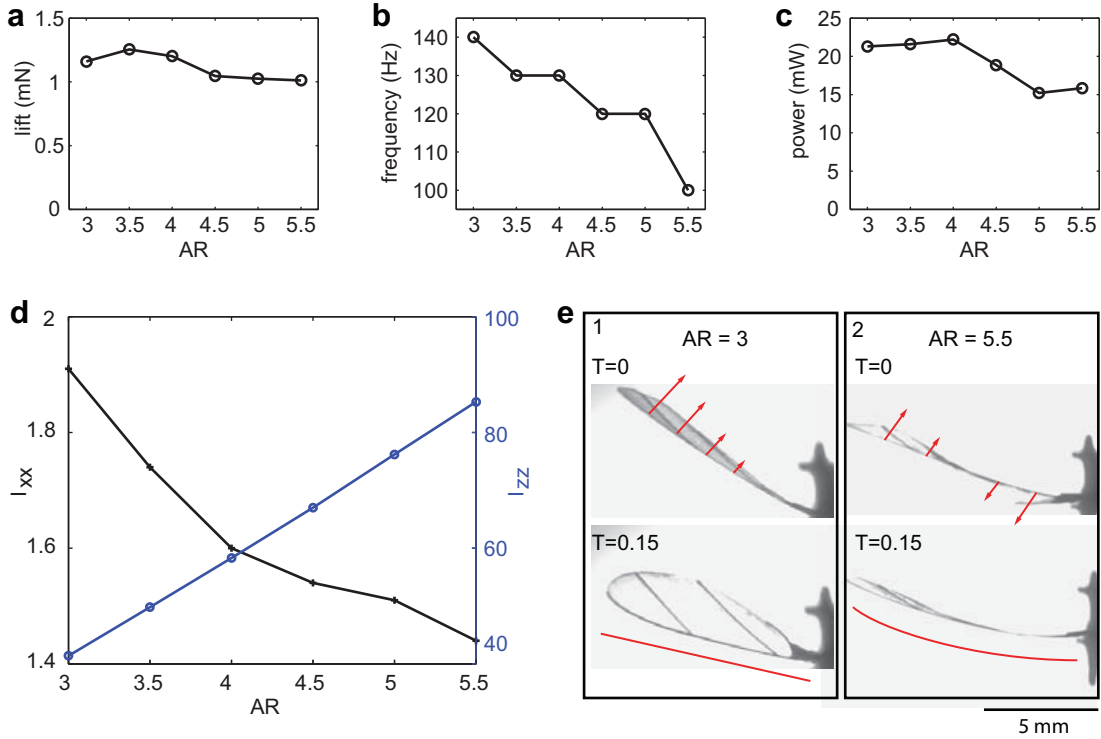


Figure 3.3: Wing aspect ratio influence on aerodynamic performance. (a) Maximum wing lift versus wing aspect ratio AR . (b) Driving frequencies at maximum mean lift versus AR . (c) Power dissipation at maximum mean lift versus AR . (d) Wing spanwise and chordwise moment of inertia as functions of aspect ratio. As AR increases, I_{xx} decreases and I_{zz} increases. (e) Aspect ratio influence on structural stiffness. (e-1) shows the wing with small aspect ratio ($AR=3$) behaves as a flat plate during rotation ($T=0$) and translation ($T=0.15$). (e-2) shows the wing with large aspect ratio ($AR=5.5$) has reduced structural stiffness. There is a torsional wave along wing span during pitching at $T=0$. The wing leading edge spar bends noticeably at $T=0.15$ as the wing stroke velocity increases.

aerodynamic force along the wing span. Consequently, we observe the large AR wings experience significant deformation at high driving frequencies. Figure 3.3e compares wing deformation between $AR = 3$ and 5.5. Figure 3.3e-1 shows a wing with $AR = 3$ being driven at 140 Hz and 150 V. We observe the wing as a flat, rigid plate at $T = 0$ and $T = 0.15$. Figure 3.3e-2 shows a wing with $AR = 5.5$ being driven at 120 Hz and 110 V. Although the operating frequency and voltage input are lower, we observe significant deformation. At $T = 0$, we observe a torsional wave propagating from wing tip to wing root. This twist is illustrated by the red arrows on figure 3.3e-2. In contrast, we do not observe large twisting for the wing with $AR = 3$. At $T = 0.15$, the wing tip accelerates and the force near the wing tip quickly grows. Consequently, we observe noticeable bending of the wing leading edge spar in the $AR = 5.5$ wing. This is illustrated by the curved red line in figure 3.3e-2. In contrast, the leading edge spar of the $AR = 3$ wing does not deform. This observation is illustrated by the red line segment in figure 3.3e-1. Hence, increasing the aspect ratio lowers the wing resonance frequency and adversely affects the wing's structural rigidity. While some previous studies [97] indicate adequate wing flexibility improves wing performance, excessive flexibility adversely affects wing lifespan. As driving frequency and voltage continue to increase, wing deformation increases and eventually the wing leading edge spar breaks under excessive aerodynamic loading.

3.4 Influence of wing area moment

In the previous section, we observe that increasing wing AR increases wing span-wise center of pressure and moment of inertia. Increasing I_{zz} leads to a reduction

of the flapping resonance frequency and adversely impacts structural stiffness. Here we investigate the effect of increased spanwise center of pressure without significantly changing the moment of inertia. This can be done by varying the first area moment \hat{r}_1 while holding other wing morphological parameters constant. Figure 3.4 compares the performance of wings with \hat{r}_1 in the range of 0.49 to 0.55. Figure 3.4a shows that mean lift increases as \hat{r}_1 increases. Figure 3.4b shows that the flapping resonance frequency remains at 140 Hz except for $\hat{r}_1 = 0.54$. The wing with $\hat{r}_1 = 0.54$ has a resonance frequency at 130 Hz because it experiences large deformation at 140 Hz due to the large aerodynamic loading. Figure 3.4c shows that power dissipation increases slowly as mean lift increases.

Here, flapping resonance frequency changes slowly because the change in wing inertia is small. Figure 3.4d shows the spanwise and chordwise moment of inertia as functions of \hat{r}_1 . From $\hat{r}_1 = 0.49$ to $\hat{r}_1 = 0.55$ the relative change of I_{xx} and I_{zz} is less than 15%. The increase of mean lift due to increased \hat{r}_1 can be explained by quasi-steady scaling. Equations (11) and (12) from [97] give

$$F_L = \frac{1}{2}\rho \frac{R^4}{AR} \frac{1}{2} \tilde{C}_L w^2 \phi_{max}^2 \hat{r}_2^2, \quad (3.6)$$

where

$$\tilde{C}_L = C_{Lmax} \frac{2}{\pi} \int_0^\pi \sin(2\alpha) \cos^2(t) dt. \quad (3.7)$$

Here the quasi-steady model suggests that mean lift is proportional to \hat{r}_2^2 . From Ellington's wing shape parametrization study, wing first and second moments \hat{r}_1 and

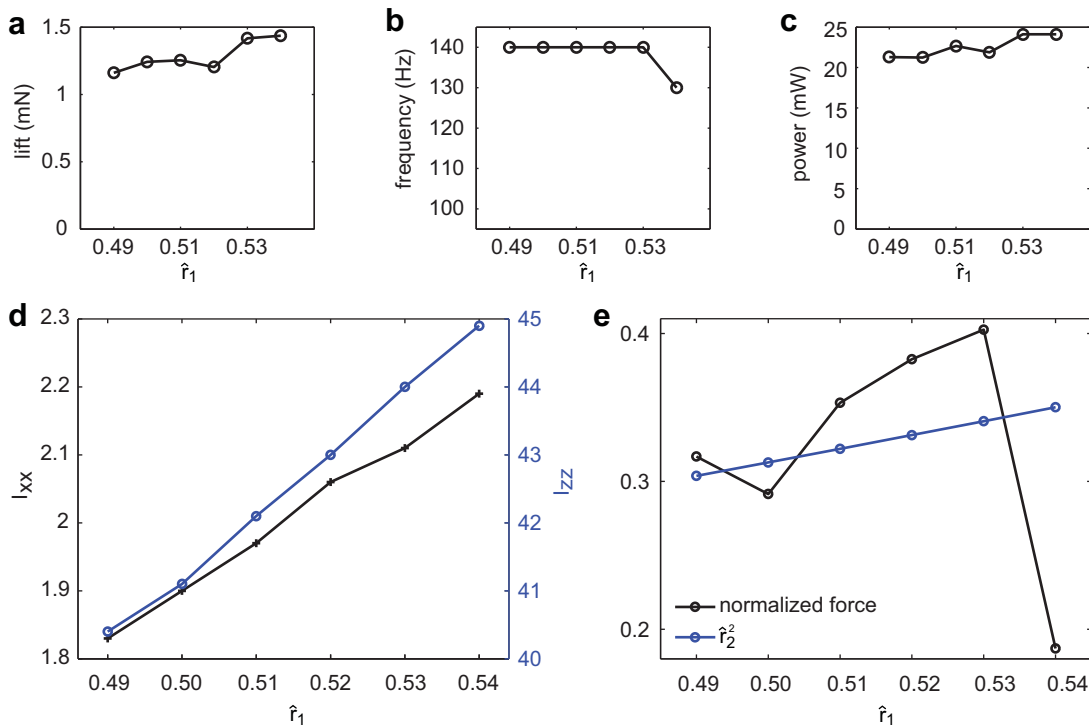


Figure 3.4: Wing area moment influence on aerodynamic performance. (a) Maximum wing lift versus wing first area moment \hat{r}_1 . (b) Driving frequencies at maximum mean lift versus \hat{r}_1 . (c) Power dissipation at maximum mean lift versus \hat{r}_1 . (d) Change of wing inertia as a function of \hat{r}_1 . Here I_{xx} and I_{zz} increase by less than 15%. (e) Comparison between quasi-steady scaling with normalized force measurements. Although the comparison shows a similar trend, there is noticeable deviation that maybe caused by ore influential parameters such as wing inertia.

\hat{r}_2 are related by the empirical function:

$$\hat{r}_2 = 0.929(\hat{r}_1)^{0.732}. \quad (3.8)$$

Figure 3.4e compares the normalized force $\frac{F_L}{\frac{1}{2}\rho\frac{R^4}{AR}\frac{1}{2}\tilde{C}_L w^2 \phi_{max}^2}$ and \hat{r}_2^2 as functions of \hat{r}_1 . We observe that the normalized force roughly follows the quasi-steady scaling relationship \hat{r}_2^2 . The wing with $\hat{r}_1 = 0.54$ is an outlier because its motion has large stroke and pitch amplitudes, and consequently leads to noticeable wing deformation.

3.5 Influence of wing leading edge sweep ratio (LESR)

We further explore the effect of wing leading edge sweep ratio on wing performance. There is noticeable spanwise flow along the leading edge of a flapping and rotating wing. As shown in 3D-CFD simulations, positive wing leading edge sweep can facilitate the growth of a wing tip vortex that enhances lift. However, varying the LESR changes the chordwise center of pressure, which affects wing pitching. Here we vary the wing leading edge profile by changing the sweep ratio from 0.5 to 1.75 in steps of 0.25. Figure 3.5a shows that mean lift decreases monotonically as sweep ratio increases. Figure 3.5b shows that the flapping resonance frequency is unaffected by changes in the wing sweep. Figure 3.5c shows small changes of power dissipation as wing sweep ratio increases.

We use quasi-steady scaling to describe the wing sweep influence on pitching dynamics. Figure 3.5d shows wing spanwise and chordwise moment of inertia as functions of the leading edge sweep ratio. The variation of I_{xx} and I_{zz} are less than

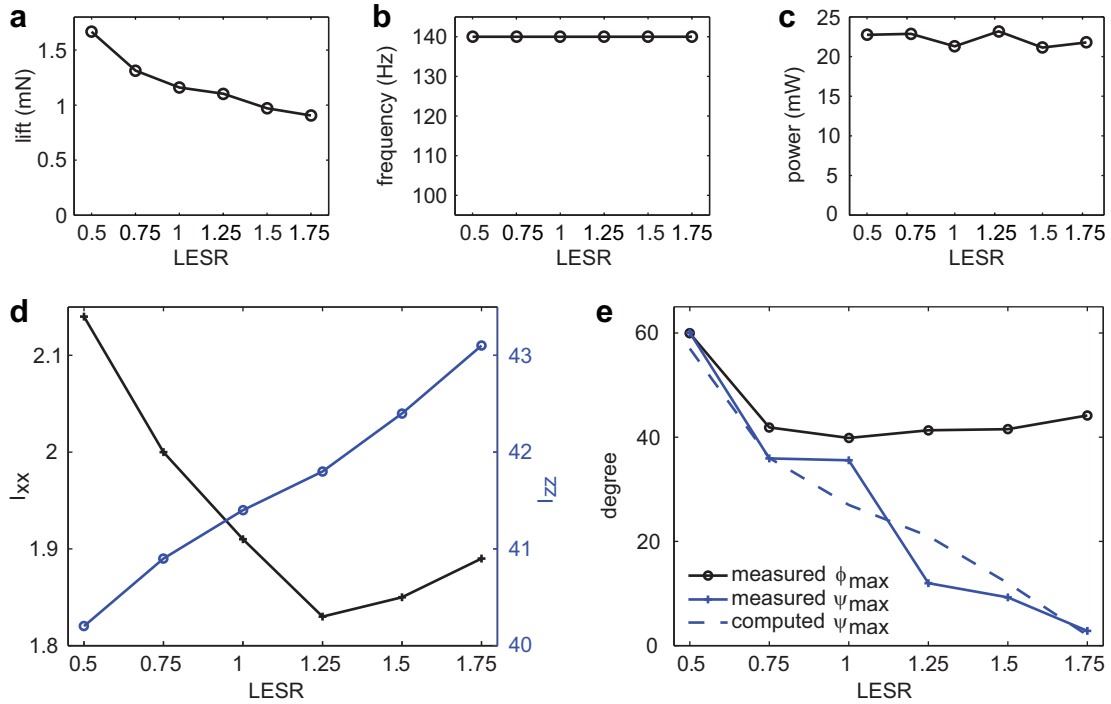


Figure 3.5: Wing leading edge sweep ratio influence on aerodynamic performance and pitching kinematics. (a) Maximum wing lift versus wing leading edge sweep ratio $LESR$. (b) Driving frequencies at maximum mean lift versus $LESR$. (c) Power dissipation at maximum mean lift versus $LESR$. (d) Change of wing inertia as a function of $LESR$. Here I_{xx} and I_{zz} increase by less than 15%. (e) Comparison of measured and simulated ψ_{max} based on measured stroke kinematics. Both the quasi-steady model and the measurement show that increased $LESR$ leads to decreased ψ_{max} .

15% and consequently the effect of changing wing inertia is small. Figure 3.5e shows stroke and pitch amplitude as a function of leading edge wing sweep ratio. Except the wing with the smallest wing sweep, the stroke amplitude (black) changes slowly as sweep ratio increases. In contrast, the measured pitch amplitude ψ_{\max} is very sensitive to wing sweep. We observe that ψ_{\max} monotonically decreases from 60° to 7° . This reduction in wing pitch can be explained using a quasi-steady model at mid-stroke. At mid-stroke, we impose

$$K\psi + I_{xx}\ddot{\psi} = \tau_f \quad (3.9)$$

where K is the wing hinge stiffness, I_{xx} is the spanwise moment of inertia, and τ_f is the aerodynamic pitch torque. At mid-stroke, τ_f is given by

$$\tau_f = 2\pi^2 \rho f^2 \phi_{\max}^2 \int_0^R r^2 c(r) C_f (r_{\text{cop}}(r, \alpha) - y_{LE}(r)) dr. \quad (3.10)$$

Here the force coefficient C_f is given by

$$C_f = (C_L(\alpha) \cos \alpha + C_D(\alpha) \sin \alpha). \quad (3.11)$$

C_L , C_D , and the local chordwise center of pressure r_{cop} can be calculated based on the method discussed in section 3.2. Given the relationship $\psi = \pi/2 - \alpha$, the only unknown in equation (3.10) is ψ . This nonlinear equation can be solved numerically to estimate ψ_{\max} . We use the measured stroke amplitude, flapping frequency, hinge stiffness, and wing shape as inputs to solve for ψ_{\max} . The result is shown as the dotted blue line in Figure 3.5e. Here the quasi-steady estimation gives the same trend as the experimental measurement.

3.6 Wing-actuator pairing

The scaled RoboBee (figure 1a) is designed using scaling analysis that does not consider wing-actuator pairing. Here we investigate wing-actuator pairing by varying wing size. Changing wing size has a large impact on wing inertia and system resonance frequency. A previous study [65] shows system resonance frequency can be approximated by the formula

$$f = \sqrt{\frac{k_{eq}}{T^2 I_{zz}}}, \quad (3.12)$$

where k_{eq} is the effective stiffness and T is the robot transmission ratio. k_{eq} is determined by the geometry and material property of compliant flexures and T is defined to be the ratio between stroke motion output and actuator tip displacement. This transmission ratio T is determined by the laminate material thickness. While it is possible to vary these parameters in the wing driver designs, it is practically difficult to build and test many wing drivers to study system resonance. Here we can easily study resonance by varying the wing inertial parameter I_{zz} .

Changes in wing spanwise moment of inertia directly impacts resonance frequency since I_{zz} is proportional to R^4 . This implies

$$f \propto \frac{1}{R^2}. \quad (3.13)$$

Equation (6.3) suggests that a decrease of wing size increases resonance frequency. From a system level perspective, changing wing radius also influences the net force

output. The RoboBee uses a four-bar linkage that can be modeled as

$$F_D = F_{act} \frac{L_3}{R_{cop,x}} \quad (3.14)$$

where F_{act} is the force output from the actuator, $R_{cop,x}$ is the spanwise center of pressure and L_3 is the effective effort arm length of the lever-like transmission. Assuming the magnitude of the output force F_{act} is limited by the electro-mechanical properties of the piezoelectric actuator, equation (3.14) implies that reducing the spanwise wing center of pressure $R_{cop,x}$ increases the amount of drag force F_D an actuator can drive against. Since the lift and drag forces are positively correlated, equation (3.14) suggests that reducing wing size leads to increased mean lift force.

However, reducing wing size also has negative effects. Firstly, the robot flexural transmission lifetime decreases as operating frequency increases. In addition, both aerodynamic efficiency and robot power dissipation increase as wing size shrinks and flapping frequency increases. Consider two differently sized wings that operate at different frequencies to generate identical lift. Equation (3.6) suggests

$$R_1^4 f_1^2 = R_2^4 f_2^2 \quad (3.15)$$

This relationship implies $\frac{1}{R^2} \propto f$. The aerodynamic efficiency is proportional to

$$\frac{\bar{F}_L}{\bar{P}_{aero}} \propto \frac{\bar{C}_L}{\bar{C}_D R f} \propto \frac{\bar{C}_L R}{\bar{C}_D} \quad (3.16)$$

In the last step of equation (3.16) we use the proportionality relationship between R

	wing 1	wing 2	wing 3	wing 4
wing area (mm ²)	162	135	108	94.5
\bar{F}_L (mN)	1.11	1.54	1.72	2.03
$f_{resonance}$ (Hz)	70	100	130	150
P_{aero} (mW)	23.7	31.9	40.7	54.8

Table 3.2: Wing size, maximum mean lift, flapping resonance frequency, and power dissipation.

and f . Consequently, lift per unit power decreases as wing span decreases.

To validate this system level scaling analysis, we make four wings of varying wing size and test their performance. Table 3.2 reports wing size, maximum mean lift, flapping resonance frequency and power dissipation. We observe that mean lift, flapping resonance frequency, and power dissipation increase as wing size is reduced. The qualitative relationship between flapping frequency and wing span is reported in a previous biological study [77].

3.7 Result and discussion

Our results show wing inertia influences stroke and pitch coupling, which further impacts mean lift by more than 60%. Increasing wing aspect ratio (AR) reduces system resonance and adversely affects structural stiffness. Wing shape parameters – first area moment (\hat{r}_1) and leading edge sweep ratio (LESR) – influence passive pitching. Finally, reducing wing size increases system operation frequency and mean lift at the cost of higher power consumption.

To improve mean lift, we design a new wing with smaller wing size and slightly thinner wing spars. Compared to the original wing, the wing span is reduced by 25% and the spanwise moment of inertia is reduced by 76%. In flapping experiments, we

find the resonance frequency of the new wing to be 150 Hz. The wing produces 2.48 mN of mean lift when driven at 190 V and the actuator consumes 36.5 mW power. The resonance frequency of the original wing is 80 Hz. This wing produces 1.81mN of mean lift when driven at 250 V and the actuator consumes 21.5 mW. The new wing produces 37% more lift and costs 70% more power dissipation. This is equivalent to doubling the robot payload capability and is a major improvement towards flight autonomy. Although this result implies the new wing is less efficient, it significantly improves mean lift without modifying actuator sizing and robot transmission. In addition, the robot operational voltage is significantly lowered, which gives much larger voltage margin for aerodynamic control and greater efficiency of the drive electronics.

In this chapter, we experimentally study the influence of wing morphological and inertial parameters on mean lift generation and power consumption. We designed and fabricated 36 different wings and test their efficiency with an at-scale robotic flapper. While our experimental studies aim to improve the performance of the Harvard RoboBee, the experimental results are directly applicable to other flapping-wing robotic designs. Having studied wing morphology and inertia, we will explore another robot parameter in the next chapter: the wing hinge. We will investigate the influence of wing hinge stiffness on passive pitching and force generation.

Chapter 4

Wing hinge influence on aerodynamic performance

4.1 Introduction

Flexure hinges are common components in small scale robots. Whereas articulation in larger scale robots has traditionally relied upon pin joints, bushings or bearings, the development of microrobots requires new techniques to manufacture joints to overcome unfavorable friction scaling. Flexure hinges exhibit negligible friction, and are compact and simple to manufacture using lamination and folding techniques [95, 99]. For these reasons, flexure hinges are a vital part in existing small biologically-inspired robotics, from running [5, 7, 48] to flying robots [65].

The wing hinge is especially important to the RoboBee [65]. Specifically, the wing pitch rotation is passively controlled by interactions between wing inertia, aerodynamic loading and restoring torque from the wing hinge. Hinge design directly

influences the pitching kinematics, which further impacts lift and drag production. In addition, the hinge needs to endure large deflections for over a million flapping periods. Consequently, the design and manufacture of wing hinge significantly influence robot aerodynamic performance and lifespan.

In this chapter, we explore wing hinge geometry influence on its lifespan and robot lift generation. We describe an experimental study that results in significant hinge endurance improvement. Further, we quantify the relationship between wing hinge stiffness and pitching dynamics, which leads to a design method for wing hinge pairing.

4.2 Hinge endurance

The RoboBee's wings flap at 100-250 Hz with a peak-to-peak angular deflection of 50°-100°. Over time, the repeated wing pitching motion causes hinge fatigue failure that requires tedious hinge replacement and robot recalibration. This failure usually occurs after ten minutes of cumulative flight time, which corresponds to 60,000 to 150,000 flapping periods. The RoboBee uses a polyimide film as the compliant wing hinge, which can be cycled to 10^7 times when the applied stress is limited to within 50MPa [41]. In this section, we examine hinge failure modes and propose designs that dramatically increase the hinge lifespan.

4.2.1 Hinge design and manufacture

The flexure hinges examined in this chapter are built with the SCM fabrication techniques [99], using a polyimide film as the flexible hinge and carbon fiber as the stiff

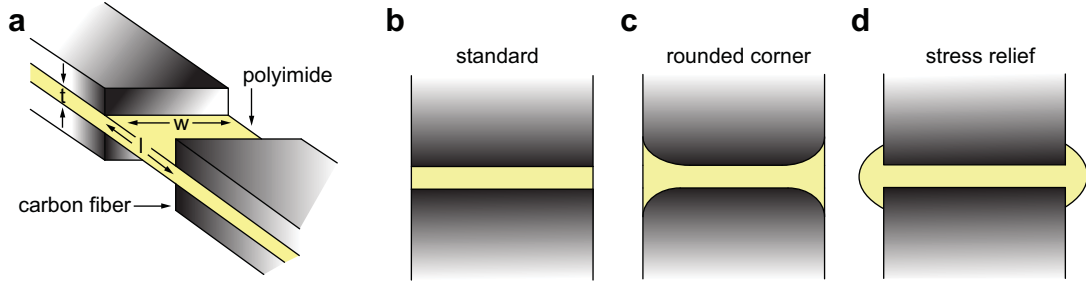


Figure 4.1: Illustration of wing hinge design and stress relieving features. (a) The wing flexure consists of a carbon fiber, polyimide, adhesive laminate. The flexure length, width, and thickness determine the hinge stiffness. (b) A standard wing hinge with a rectangular flexure. (c) A wing hinge with rounded corner. (d) A wing hinge with stress relief materials near the corners.

base and wing anchor. Figure 4.1a illustrates the cross section of a flexure laminate, whose polyimide geometry determines the hinge bending stiffness:

$$k = \frac{Et^3w}{12l}. \quad (4.1)$$

Here E is the Young's modulus of polyimide, l , w , and t are the flexure length, width, and thickness, respectively. In section 4.3, we will discuss the influence of hinge stiffness on flapping dynamics.

We hypothesize that hinge failure originates from the hinge corners (figure 4.1b), where stress concentration is the highest due to an abrupt change of material stiffness. To reduce this potential stress concentration, we propose several hinge corner designs such as rounded corners (figure 4.1c) and stress relief (figure 4.1d). Alternatively, we can reduce overall flexure stress by varying the hinge geometry. Assuming constant curvature along a bending hinge, we estimate the hinge stress by the following

equation:

$$\sigma = \frac{E\psi t}{2l}, \quad (4.2)$$

where ψ is the pitch angle. Equation (4.2) implies that the hinge stress can be reduced by decreasing the deflection angle, decreasing the flexure thickness, or increasing the flexure length. In our experiments, ψ cannot be easily changed without impacting aerodynamic performance. The flexure thickness cannot be altered easily because only certain polyimide film thickness are available ($7.5\mu\text{m}$, $12.7\mu\text{m}$, $25\mu\text{m}$). Therefore, we decide to reduce the hinge stress by increasing the hinge length. According to equation (4.1), we can maintain the same stiffness by proportionally increasing the hinge width. However, this scaling makes the wing hinge more susceptible to plastic deformation and buckling. In the following sections, we explore hinge failure modes and evaluate the effectiveness of each stress relieving method.

4.2.2 Hinge failure

To investigate hinge failure modes, we conduct flapping endurance experiments using the setup introduced in Chapter 2. The wing driver flaps a wing until cracks develop on the wing hinge. The cracks propagate on the wing hinge and eventually affect the pitching kinematics. The change of flapping kinematics leads to anomalous force profiles, which are immediately detected by the force sensors. Once the instantaneous maximum drag force exceeds 1.5 times of the initial measurements, the control software triggers the high speed cameras, saves the corresponding force measurements, and terminates the flapping experiments. Finally, we remove the wing hinge pair and image the damaged wing hinge using a scanning electron microscope

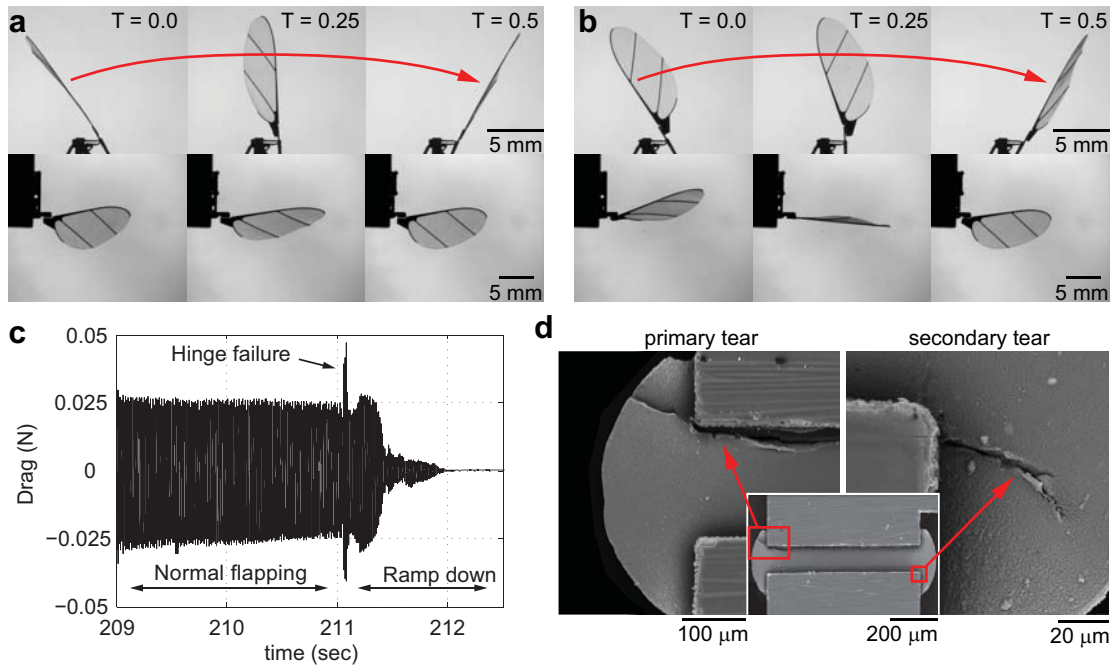


Figure 4.2: Hinge failure and its influence on flapping kinematics and force production. (a) Top and front view image sequence of typical flapping motion. (b) Top and front view image sequence of flapping motion with a torn hinge. (c) Drag force measurement of a hinge endurance test. The spike in drag measurement indicates hinge failures. (d) SEM images of a torn hinge. There is a primary tear at the upper left hinge corner and a secondary tear at the lower right hinge corner.

(SEM).

Figure 4.2 shows the results of a sample endurance experiment, in which the flapping frequency and the voltage amplitude are set to 120 Hz and 140 V. Figure 4.2a, b compares the flapping kinematics before and after hinge failure. In a typical flapping period (figure 4.2a), the pitching angle is small during stroke reversal ($T = 0.0$ and $T = 0.5$) and reaches a maximum during midstroke ($T = 0.25$). In contrast, the wing motion changes considerably as the crack propagates (figure 4.2b). Wing pitching becomes asymmetric in the beginning ($T = 0.0$) and end ($T = 0.5$) of a half flapping period, and the maximum pitch angle exceeds 90° . During wing midstroke ($T = 0.25$), the top and bottom part of the wing hinge collide, leading to force spikes along the drag axis. Figure 4.2c shows the corresponding force trace. Once the maximum drag force exceeds 0.04 N, the system terminates the flapping experiment.

Figure 4.2d shows the SEM images of a failed wing hinge. We observe a primary tear at the upper hinge corner closer to the wing tip (upper left corner of figure 4.2d). In addition, there is a smaller secondary tear at the lower hinge corner closer to the wing root (lower right corner of figure 4.2d). If the flapping experiment continues after the cracks appear, the wing hinge tears completely within 500-1000 flapping cycles.

4.2.3 Hinge endurance

To test the stress reducing features and the geometry scaling method, we conducted endurance tests for four different designs. These hinge designs include a standard rectangular hinge (figure 4.1b), a hinge with rounded corners (figure 4.1c),

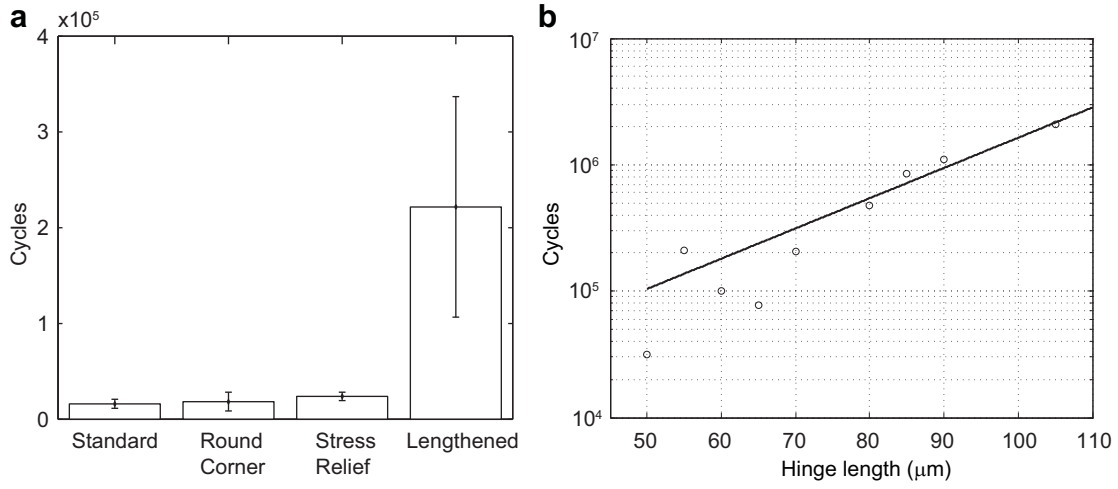


Figure 4.3: Results of the hinge endurance test. (a) Hinge lifespan of four designs. The hinge design with increased length lasts 13 times longer than the standard ones. (b) Hinge lifespan as a function of hinge length. The lifespan grows exponentially as length increases.

a hinge with extra stress relieving material (figure 4.1d), and a scaled hinge that is 30% longer and wider. The standard hinge dimension is set to $1.45\text{mm} \times 125\mu\text{m} \times 12.7\mu\text{m}$. For each design, eight identical prototypes are tested to reduce manufacturing variability. In every experiment, the wing is driven at 160 Hz until the hinge fails.

Figure 4.3a compares the lifespan of these designs. Compared to the standard hinge design, rounded corner and stress relief features do not lead to significant lifespan improvements. In contrast, the hinge design that is 30% longer and wider shows 13 times increase in mean lifespan without noticeably affecting the pitching kinematics.

To further quantify how hinge length affects flexure hinge life, hinges with lengths varying from $55 \mu\text{m}$ to $105 \mu\text{m}$ are tested until failure. Here the hinge widths are scaled accordingly to ensure the same stiffness. In these experiments, three hinges of the

same design are tested to reduce variability. Figure 4.3b shows hinge lifespan grows exponentially as hinge length increases, which implies that flexure endurance can be improved significantly through geometry scaling. We further extract the flapping kinematics from each experiment and find little difference in the pitch ($34\pm 4^\circ$) and stroke ($29.6\pm 1.2^\circ$) amplitudes. This result confirms that the present scaling designs do not significantly impact the off-axis hinge stiffness and flapping dynamics.

4.3 A quasi-steady model of passive wing pitching

Besides affecting the robot lifespan, the wing hinge design further influences the robot aerodynamic performance. Specifically, the passive wing pitch motion is affected by aerodynamic loading, hinge torque, and wing inertia. The resultant pitch kinematics impact lift and drag force production. In this section, we introduce a method for choosing the optimal wing hinge stiffness.

In previous studies, selecting the optimal wing hinge stiffness requires testing of multiple wing hinges over a wide range of robot operating conditions (driving voltage and frequency). This tedious process is both time consuming and detrimental to the robot actuator and transmission lifetime. We develop a quasi-steady model that reduces the number of experiments needed for the wing-hinge pairing process. In section 2.6.1, we approximate the flapping kinematics using four parameters: ϕ_{\max} , ψ_{\max} , f , and δ . Out of these parameters, the robot directly controls the stroke amplitude ϕ_{\max} and flapping frequency f . Assuming the relative phase δ is small in most experiments, we propose a model that predicts ψ_{\max} given wing shape, hinge stiffness k , and input parameters ϕ_{\max} and f . Concurrently, the model predicts F_L

and F_D at midstroke.

Our quasi-steady model is based on the blade element method used in numerous previous studies of insect flight (Dickinson et al. 1999; Sane & Dickinson 2001; Whitney & Wood 2010). The blade element method states that the instantaneous force on a translating wing chord is proportional to the local velocity squared. The total force on a translating wing is given by the integral along the wing span direction:

$$F_i(t) = \frac{1}{2}C_i(\alpha(t))\rho \int_{x_r}^{x_r+R} u^2(r,t)c(r)dr, \quad (4.3)$$

where ρ is the air density, $u(r,t)$ is the local wing chord velocity, x_r is the wing root location, $c(r)$ is the local chord length and i stands for either lift (L) or drag (D). The force coefficients C_i are functions of the angle of attack α , which is defined as $\alpha = \pi/2 - \psi$. Since we are only interested in modeling the wing pitching at midstroke, we ignore added mass and rotational circulation terms that are only important during stroke reversal. Consequently, we only use the translational term (equation 4.3) of the quasi-steady model to estimate the aerodynamic force and to predict the passive pitching at midstroke. In equation (4.3) the lift and drag coefficients C_L and C_D are substituted with Dickson's dynamically scaled measurements (figure 5 in Dickson et al. [25]).

Equation (4.3) assumes fully prescribed kinematics; however, in our application we need to solve a coupled fluid-wing system because the wing pitching is passive.

We impose angular momentum balance to solve for wing pitch:

$$\sum_i \boldsymbol{\tau}_i = I\boldsymbol{\omega} + \boldsymbol{\omega} \times I\boldsymbol{\omega}, \quad (4.4)$$

where $\sum_i \boldsymbol{\tau}_i$ is the sum of external torques, I is the moment of inertia tensor, and $\boldsymbol{\omega}$ is the angular velocity of the wing. At midstroke, α is a minimum if we assume $\delta = 0^\circ$. The spanwise component of equation (4.4) is:

$$k\psi - (F_L \cos \alpha + F_D \sin \alpha)R_{\text{cop}} = I_{xx}\ddot{\alpha} + (I_{yy} - I_{zz})\dot{\phi}^2 \cos \psi \sin \psi, \quad (4.5)$$

where k represents the hinge stiffness, R_{cop} is the mean chordwise center of pressure and I_{xx} is the effective rotational moment of inertia considering added mass contributions from the surrounding fluid. We obtain I_{xx} , I_{yy} , and I_{zz} from the CAD modeling software SolidWorks (SolidWorks, 2013, Troy, MI), and adopt the added mass corrections from Whitney & Wood [96].

Equation (4.3) and (4.5) form a coupled system that predicts lift, drag, and angle of attack based on kinematic and morphological inputs. While parameters such as hinge stiffness and wing inertia are straightforward to calculate, the center of pressure coefficient R_{cop} is difficult to model. Instead of using the sigmoid approximation in section 3.2, we experimentally measure R_{cop} for a given wing planform. R_{cop} can be calculated using measured kinematics at wing midstroke. We can substitute the

kinematic parameters into equation (4.5) and obtain:

$$R_{\text{cop}} = \frac{k(\pi/2 - \alpha_{\text{min}}) - 4\pi^2 f^2 I_{xx}(\pi/2 - \alpha_{\text{min}}) - 4\pi^2 f^2 (I_{yy} - I_{zz})\phi_{\text{max}}^2 \cos \alpha_{\text{min}} \sin \alpha_{\text{min}}}{F_L \cos \alpha_{\text{min}} + F_D \sin \alpha_{\text{min}}}. \quad (4.6)$$

To evaluate the performance of a particular wing, we first run several experiments to measure the hinge kinematics. Then we solve for R_{cop} as a function of α using equations (4.3) and (4.6). After $R_{\text{cop}}(\alpha)$ is computed, equations (4.3) and (4.6) can be used to simultaneously predict lift, drag, and wing pitching kinematics for other driving conditions and hinge stiffness. Due to the assumption that δ is small, equations (4.3) and (4.6) are only invoked at midstroke.

In summary, this proposed quasi-steady model assumes purely sinusoidal stroke and pitch motion with small phase shift δ . It reduces the number of wing hinge fabrication and flapping tests needed for the wing-hinge pairing process. However, the model ignores unsteady effects that maybe crucial for certain kinematic inputs. In the next section, we examine the model accuracy and discuss its shortcomings.

4.4 Results and discussion

4.4.1 Accuracy of the quasi-steady model

To examine the robustness of the quasi-steady model, a wing is driven at various input frequencies and voltage amplitudes. The wing is driven from 85 to 145 Hz in steps of 5 Hz, and the driving voltage is increased from 80 V to 130 V in units of 10 V. We define an operating point to be an input frequency and voltage pair. Four wing

Hinge label	w (mm)	l (μm)	t (μm)	k ($\mu\text{N m/rad}$)
soft	1.25	140	7.5	0.73
normal	1.25	80	7.5	1.4
stiff	1.25	45	7.5	2.4
very stiff	1.25	155	12.7	3.4

Table 4.1: Polymer hinge geometries and stiffnesses. Four hinges with varying stiffness values are designed and manufactured to study passive hinge rotation as a function of input stroke motion. The Young’s modulus of the flexure material (Kapton) is 2.5 GPa.

hinges with different stiffness values are built to study the interplay of aerodynamic and elastic hinge torques (table 4.1).

Assuming δ has negligible effect at midstroke, the quasi-steady model predicts α_{\min} during the translational phase. First, we quantify the relationship between two kinematic parameters: ϕ_{\max} and ψ_{\max} . Figure 4.4a compares ϕ_{\max} and ψ_{\max} at various testing conditions. Each curve in the graph represents a discrete frequency sweep (85–145 Hz) at a fixed drive voltage. Figure 4.4b shows the same data by plotting hinge angle as a function of wing tip velocity. It should be noted that all curves from figure 4.4a overlap in figure 4.4b, which suggests a universal relationship between maximum stroke velocity and maximum hinge angle. This observation confirms that the effect of the phase shift on the maximum translational lift is small at midstroke.

From the tracked wing kinematics we solve the quasi-steady model for the center of pressure $R_{\text{cop}}(\alpha)$. As shown in figure 4.5a, $R_{\text{cop}}(\alpha)$ is a monotonically increasing function of α .

The experimentally measured $R_{\text{cop}}(\alpha)$ can be used to further predict changes to the kinematic parameters as the hinge stiffness varies. From an experimental perspective, we aim to find the optimal hinge stiffness for a given wing planform. Rather than

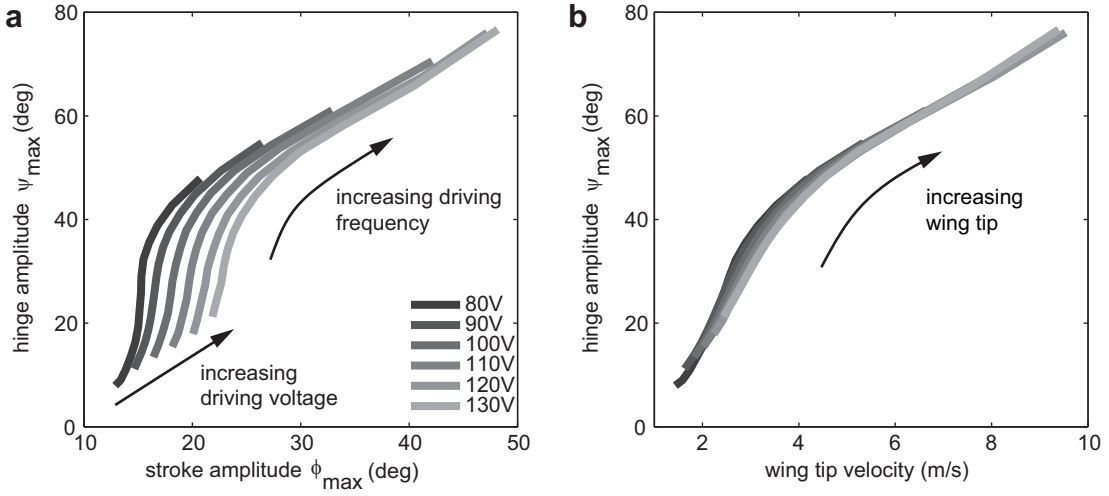


Figure 4.4: Hinge amplitude ψ_{\max} as a function of actively controlled kinematic parameters. (a) Maximum hinge angle versus maximum stroke angle at various input frequencies and voltage amplitudes. (b) Maximum hinge angle versus maximum stroke velocity. Both (a) and (b) use the same set of experimental data. The hinge stiffness for these experiments is $k = 1.4 \mu\text{Nm/rad}$.

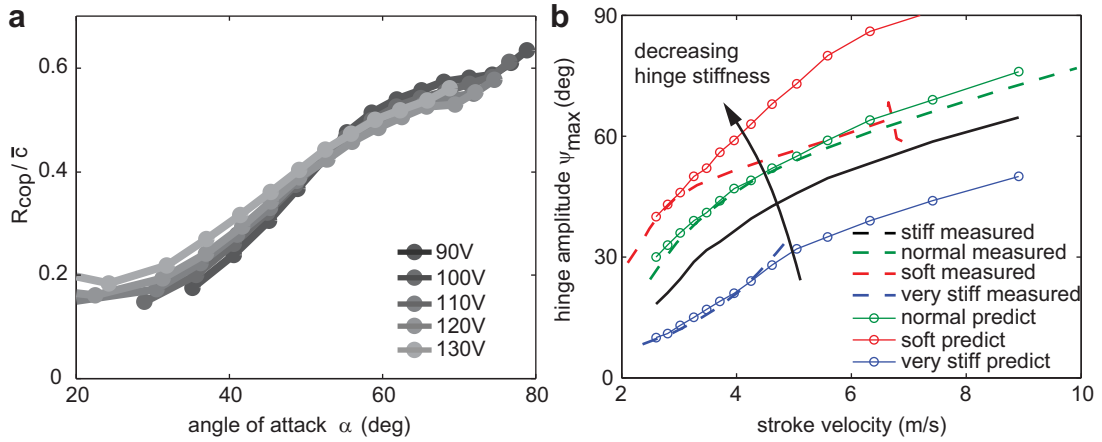


Figure 4.5: Quasi-steady model prediction based on measured R_{cop} . (a) Normalized center of pressure R_{cop}/\bar{c} versus minimum angle of attack α . The center of pressure is measured with respect to the wing leading edge and is normalized by the mean wing chord. Each curve represents a frequency sweep from 85 to 145 Hz at a fixed driving voltage. (b) Hinge angle prediction as function of wing tip velocity at different hinge stiffnesses. The relationship is measured for a particular wing-hinge pair (shown in black) to compute R_{cop} as a function of α . Using the R_{cop} function, the hinge angle function is predicted for the soft, normal and very stiff hinges (red, green, blue curves).

designing and testing a number of hinges, we can use the quasi-steady model to predict α_{\min} as the hinge stiffness changes. Accurate predictions of α_{\min} at varied hinge stiffnesses greatly reduce the number of experiments needed for wing or hinge characterization.

Figure 4.5b shows an example of using the quasi-steady model to predict α_{\min} and α_{\max} relationships for different wing hinges in various operating conditions. First, according to the procedure discussed in section 4.3, we measure α_{\min} for a wing with a stiff hinge (black curve). Next, we solve for $R_{\text{cop}}(\alpha)$ by invoking equation (4.6). Then we predict changes to α_{\min} when the hinge stiffness changes. Finally, we manufacture a number of hinges and run experiments to compare with the model prediction. As shown in figure 4.5b, the predictions for the normal and very stiff hinges (green and blue curves) show good agreement with the measurements. The error between maximum predictions and experimental measurements for the normal hinge is less than 4° (green curve). The maximum error for the very stiff hinge is also less than 4° for small stroke velocity (blue curve). However, the experimental measurement of wing tip velocity with the very stiff hinge does not exceed 5 m/s. The actuator dynamics limits the range for comparison of experiment and model for stiff hinges. However, the model does not include actuator dynamics and is thus not limited.

While predictions for the normal and very stiff hinges show good agreement with the experiments, the prediction for the soft hinge (red curve) in figure 4.5b is inaccurate at high stroke velocity. This discrepancy can be understood by observing the large phase shift δ for the soft hinge design at high flapping frequencies, as shown

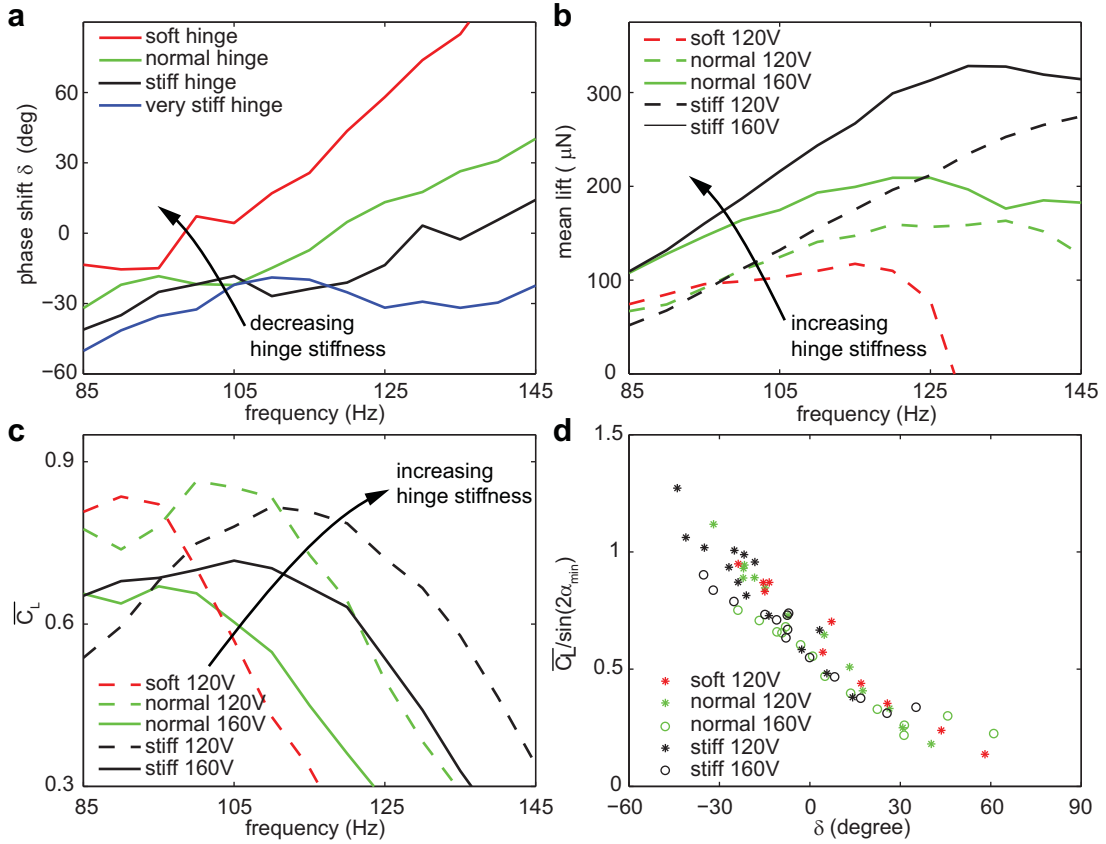


Figure 4.6: The influence of phase shift δ on mean lift. (a) Relative phase shift δ as a function of frequency for changing hinge stiffness. (b) Mean lift versus input frequency with changing hinge stiffness and driving voltage. (c) Mean lift coefficient versus input frequency. (d) Normalized mean lift coefficient versus δ . All panels show the same set of experimental data.

in figure 4.6a. In our quasi-steady model, we assume $\delta \approx 0^\circ$. Consequently, it is unsurprising that the model accuracy deteriorates at large δ .

4.4.2 Influence of phase shift δ on lift

Our experimental data shows the dependence of δ on the hinge stiffness and its effect on the mean lift. Figure 4.6a shows δ versus f for different hinge stiffness, where the driving voltage is fixed at 120 V. As the driving frequency increases or the

hinge stiffness decreases, we observe δ increases.

Figure 4.6b shows the mean lift versus the input frequency with changing hinge stiffness and driving voltage. Experimentally we observe that a stiffer hinge generates a higher mean lift. While the kinematic parameters ϕ_{\max} , ψ_{\max} , and δ are interdependent in our experiments, figure 4.6c, d show the effect of δ by normalizing away the effects of ϕ_{\max} and ψ_{\max} . Figure 4.6c shows the mean lift coefficient:

$$\overline{C}_L = \frac{\overline{F}_L}{\frac{1}{2}\rho u_{rms}^2 S}, \quad (4.7)$$

where u_{rms} is the root mean square velocity given by

$$u_{rms} = \sqrt{\frac{1}{T} \int_0^T u^2(t) dt}. \quad (4.8)$$

In equation (4.8), T is the flapping period and u is the instantaneous wing tip velocity. Here $u(t)$ is approximated as a pure sinusoid based on the measured ϕ_{\max} . All experiments show that increasing frequency corresponds to decreasing \overline{C}_L . Normalizing to \overline{C}_L removes the effect of varying ϕ_{\max} in different tests. We further remove the effect of ψ_{\max} in figure 4.6c. According to Dickson's formula, C_L is approximately proportional to $\sin(2\alpha)$; hence, we normalize all measured \overline{C}_L values by the corresponding measured α_{\min} values. Figure 4.6d shows $\overline{C}_L / \sin(2\alpha_{\min})$ versus δ for all experiments, which indicate negative correlation between \overline{C}_L and δ .

Figure 4.6d shows that $\overline{C}_L / \sin(2\alpha_{\min})$ reduces by a factor of 2 from $\delta = -30^\circ$ to $\delta = 40^\circ$, which suggests that δ has a large influence on the mean lift force. We further compare the relative importance of δ on mean lift to that of the other kinematic

parameters ϕ_{\max} , ψ_{\max} and f . Based on the quasi-steady model, the mean lift has a quadratic dependence on f , a linear dependence on ϕ_{\max} and a trigonometric dependence on ψ_{\max} . This suggests that the flapping frequency f is the most significant factor to the mean lift. Figure 4.6b shows the trend that the mean lift increases as the driving frequency and voltage increase. However, as f and ϕ_{\max} increase, δ also increases. As shown by the dotted red and green curves in figure 4.6b, the effect of δ gradually dominates at high frequency because the mean lift drops. Hence, the relative importance of ϕ_{\max} , ψ_{\max} , f , and δ depends on the system operating conditions. When ϕ_{\max} , ψ_{\max} , and f are small, increasing the flapping frequency is most effective to increase the lift. On the other hand, stiffening the wing hinge is more effective when δ exceeds 40° . For a flapping-wing vehicle, f and ϕ_{\max} are often limited by actuator and transmission designs. Meanwhile, δ and ψ_{\max} are mainly influenced by the choice of hinge stiffness. Considering the limits on actuation, the choice of appropriate hinge stiffness is crucial towards achieving large mean lift.

In summary, the quasi-steady model yields accurate predictions of the passive pitching angle ψ_{\max} for small or negative δ . The difference between quasi-steady prediction of ψ_{\max} and measurements is always smaller than 6° for $\delta < 40^\circ$. However, it does not account for unsteady mechanisms and fails at large δ .

Although the passive pitching experiments investigate the influence of δ on lift production, they are limited because we do not have independent control over δ and ψ_{\max} . To completely isolate the effect of δ , we need to vary δ while holding other kinematic parameters constant. This experimental limit motivates the need to develop high fidelity numerical models, in which stroke and pitch motion can be

independently prescribed. In the next chapter, we introduce 2D and 3D numerical models that investigate the flow structures unique to flapping flight.

Chapter 5

Numerical models of flapping flight

5.1 Introduction

In the previous chapters, we explore wing-structure interaction by experimentally varying the wing morphology and the hinge stiffness. While these experiments lead to significant performance improvements, they do not investigate the underlying flow structures related to flapping flight. Without studying the underlying physics, it is difficult to generalize the experimental results to other robotic flappers of different size and actuation design.

Thus far we have adopted the blade element method [96] and propose a quasi-steady model to interpret the flapping experiments with passive pitching. Although computationally simple, the quasi-steady model involves many fitting parameters and does not fully capture the underlying aerodynamics. For instance, the model assumes the system always remains in equilibrium despite that flapping flight is intrinsically unsteady. Consequently, the model does not concern flow history and induced flow

structures. These flow structures and their time evolution, such as the growth and shedding of the leading and trailing edge vortices, are unique and crucial to flapping flight [23, 27]. This theoretical limitation motivates us to develop high fidelity numerical models, which are derived from first principles to describe unsteady fluid-wing interactions.

In this chapter, we develop a number of computational models to investigate the flow structures associated with flapping flight. We compare the quasi-steady, the 2D, and the 3D numerical models to experimental measurements and examine the tradeoff between model complexity and computational cost. By exploring the relationship between flapping kinematics and induced flow, we offer insights to the experimental results observed in the previous chapters.

5.2 The Navier Stokes equation

The quasi-steady model ignores two fundamental properties of flapping flight: unsteadiness and viscous interaction. Derived from first principles, the Navier Stokes equation offers a complete description of fluid flow and fluid-solid interactions. We model flapping-wing flight through numerically solving the incompressible Navier Stokes equation, which has the form:

$$\rho \frac{\partial \mathbf{u}}{\partial t} + \rho(\mathbf{u} \cdot \nabla) \mathbf{u} = -\nabla p + \mu \nabla^2 \mathbf{u}, \quad (5.1)$$

$$\nabla \cdot \mathbf{u} = 0, \quad (5.2)$$

$$\mathbf{u}|_{wing} = (u, v)_{wing}, \quad (5.3)$$

$$p|_{\infty} = 0. \quad (5.4)$$

In equation (5.1), \mathbf{u} and p denote the fluid velocity field and the pressure field. The parameters ρ and μ denote the fluid density and viscosity. The term $\rho \frac{\partial \mathbf{u}}{\partial t}$ accounts for temporal unsteadiness; the term $\rho(\mathbf{u} \cdot \nabla) \mathbf{u}$ accounts for spatial convection; the term ∇p represents pressure contribution; and the term $\mu \nabla^2 \mathbf{u}$ describes viscous effects. Equation (5.2) states the incompressibility condition, which is enforced by solving the corresponding pressure field.

The boundary condition given by equation (5.3) describes the time-varying fluid-wing interactions. Due to this non-slip boundary condition, fluid on the wing surface moves at the same velocity as the wing. This boundary condition implies viscous effects are significant near the wing surface, and that viscous interaction contributes to boundary layer and vortex evolution. Finally, we set the far field pressure to zero to ensure the problem is well-posed.

This Navier Stokes equation is a non-linear, second order partial differential equation. Unlike the quasi-steady model, this equation does not involve any fitting parameters. In addition to solving both the flow field and the pressure field, we can

calculate the forces and torques on a flapping wing:

$$\begin{aligned}\mathbf{F} &= \int_{wing} \hat{\mathbf{n}} \cdot \boldsymbol{\sigma} da, \\ \mathbf{T} &= \int_{wing} \mathbf{r} \times (\hat{\mathbf{n}} \cdot \boldsymbol{\sigma}) da.\end{aligned}\tag{5.5}$$

Here $\hat{\mathbf{n}}$ is the wing surface normal, \mathbf{r} is the displacement from the wing root, and $\boldsymbol{\sigma}$ is the stress tensor:

$$\boldsymbol{\sigma} = -p\mathbf{I} + \frac{1}{2}\mu(\nabla\mathbf{u} + (\nabla\mathbf{u})^T).\tag{5.6}$$

The Navier Stokes equation does not have a closed-form solution. While a number of numerical methods [16, 40, 56, 84] have been developed for various applications, these methods are computationally expensive compared to the quasi-steady model. In the following section, we develop 2D and 3D numerical models and examine their accuracy and computational cost.

5.3 2D CFD models

The 2D CFD models approximate flapping flight by projecting the motion of a wing chord at midspan onto a 2D plane. As discussed in Chapter 2, this simplification approximates wing stroke motion as a sinusoidal planar translation with the amplitude $L = r_{mid}\phi_{max}$, where r_{mid} is half of the wingspan and ϕ_{max} is the stroke amplitude. Due to this kinematic approximation, the 2D model cannot investigate wing morphology influence and the flows parallel to the wingspan. On the other hand, it is computationally simpler compared to 3D numerical solvers. In the next section, we describe the numerical methods for solving the 2D model.

5.3.1 2D simulation with fully prescribed kinematics

The structure of the numerical solver is adopted from the method developed in Hesthaven & Warburton [47]. To solve this time dependent equation, each time step is decomposed into three stages. The first stage explicitly solves for an intermediate field $\tilde{\mathbf{u}}$ using a second order Adams-Bashforth method:

$$\frac{\frac{3}{2}\tilde{\mathbf{u}} - 2\mathbf{u}^n + \frac{1}{2}\mathbf{u}^{n-1}}{\Delta t} = -2(\mathbf{u}^n \cdot \nabla)\mathbf{u}^n + (\mathbf{u}^{n-1} \cdot \nabla)\mathbf{u}^{n-1}. \quad (5.7)$$

In the second stage, we impose the incompressibility condition to solve for the pressure field p . This step is formulated as an implicit Poisson problem with the Neumann boundary condition along the wing surface:

$$\begin{aligned} \frac{1}{\rho}\nabla^2 p^{n+1} &= \frac{3}{2\Delta t}\nabla \cdot \tilde{\mathbf{u}} \\ BC : \frac{1}{\rho}\hat{\mathbf{n}} \cdot \nabla p^{n+1} &= -2\hat{\mathbf{n}} \cdot \left(\frac{D\mathbf{u}^n}{Dt} - \nu\nabla^2\mathbf{u}^n\right) + \hat{\mathbf{n}} \cdot \left(\frac{D\mathbf{u}^{n-1}}{Dt} - \nu\nabla^2\mathbf{u}^{n-1}\right) \end{aligned} \quad (5.8)$$

In the third stage, we calculate the flow field by implicitly solving a Helmholtz equation with the Dirichlet boundary condition along the wing surface:

$$\begin{aligned} -\nabla^2\mathbf{u}^{n+1} + \frac{3}{2\nu\Delta t}\mathbf{u}^{n+1} &= \frac{3}{2\nu\Delta t}\left(\tilde{\mathbf{u}} - \frac{2\Delta t}{3\rho}\nabla p^{n+1}\right) \\ BC : \mathbf{u}^{n+1}|_{\partial\Omega} &= \mathbf{u}|_{wing} \end{aligned} \quad (5.9)$$

Since this method uses an explicit scheme for solving the non-linear advection step, it requires small time step to guarantee convergence. In contrast, the pressure projection and viscous correction steps are solved implicitly. These steps have less restriction on time step size but are computationally expensive.

We implement the nodal discontinuous Galerkin finite element method (DG-FEM) towards solving the equations. For the implicit steps, we adopt the internal penalty flux formulation to construct the positive definite Laplace operator. We use the open source package DistMesh [76] to generate the Delaunay triangulation mesh, in which smaller mesh elements are specified near the wing leading and trailing edges to resolve flow-structure details. The mesh radius is chosen to be 15 times the wing chord to reduce artificial boundary effects. In this nodal method, we interpolate the solution using fifth order Lagrange polynomials.

In this solver setup, the Laplace and Helmholtz operators are only dependent on the mesh geometry. In each time step, the numerical systems are solved implicitly using the identical operator. To improve the computational efficiency, we compute the Cholesky decomposition of the operators during solver initialization. Consequently, the mesh geometry must remain time independent. To account for the time varying boundary conditions induced by the flapping wing kinematics, we rewrite the Navier Stokes equation in a non-inertial system defined by (ξ, η) :

$$\begin{aligned} \frac{\partial \hat{\mathbf{u}}}{\partial t} + \nabla_{\xi} \hat{\mathbf{u}} \cdot \boldsymbol{\xi}_t + \nabla_{\xi} \cdot J^T \hat{\mathbf{u}} \hat{\mathbf{u}} &= -\frac{1}{\rho} J \nabla_{\xi} \hat{p} + \nu \nabla_{\xi}^2 \hat{\mathbf{u}} \\ \nabla_{\xi} \cdot (J^T \hat{\mathbf{u}}) &= 0 \end{aligned} \quad (5.10)$$

In equation (5.10), the velocity and the pressure fields $\hat{\mathbf{u}}$ and \hat{p} are functions of the moving coordinates that satisfy:

$$\begin{aligned} \hat{\mathbf{u}}(\xi, \eta, t) &= \mathbf{u}(x, y, t) \\ \hat{p}(\xi, \eta, t) &= p(\xi, \eta, t) \end{aligned} \quad (5.11)$$

Elements of the Jacobian matrix are defined as: $J_{ij} = \frac{\partial \xi_j}{\partial x_i}$. The boundary conditions are specified by the wing stroke and pitch motions defined in equation (2.3). To ensure that this is well-posed, we prescribe the wing stroke and pitch kinematics. This formulation allows us to independently vary the kinematic parameters ϕ_{\max} , ψ_{\max} and δ .

Once the fluid velocity field and the pressure field are solved, we can compute the force per unit length using equation (5.5). In the 2D formulation, the expanded form of equation (5.5) is given by:

$$\begin{aligned} f_L &= - \int_{wing} (-pn_y + \mu \frac{\partial u}{\partial y} n_x + \mu \frac{\partial v}{\partial x} n_y + 2\mu \frac{\partial v}{\partial y} n_y) dl \\ f_D &= - \int_{wing} (-pn_x + 2\mu \frac{\partial u}{\partial x} n_x + \mu \frac{\partial v}{\partial x} n_y + \mu \frac{\partial u}{\partial y} n_y) dl \end{aligned} \quad (5.12)$$

We can further compute the instantaneous chordwise lift and drag coefficient as:

$$\begin{aligned} C_L &= \frac{f_L}{\frac{1}{2} \rho u_x^2 c} \\ C_D &= \frac{f_D}{\frac{1}{2} \rho u_x^2 c} \end{aligned} \quad (5.13)$$

where u_x is the instantaneous leading edge speed and c is the local wing chord length. To predict the net force on a flapping wing, we need to substitute these force coefficients into the blade element method given by equation (4.3). Figure 5.1a illustrates the moving wing coordinates (ξ, η) , the inertial coordinates (x, y) , the definition of f_L and f_D and the fluid torque τ_f . Figure 5.1b shows an enlarged image of the computational mesh.

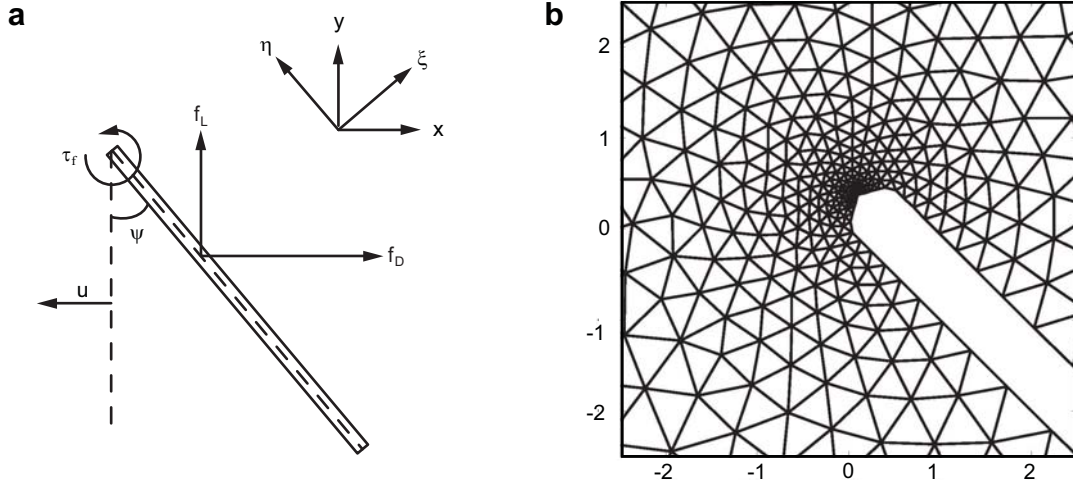


Figure 5.1: The setup of the 2D FEM-DG numerical solver. (a) A moving wing coordinate is defined by (ξ, η) and an inertial coordinate is defined by (x, y) . The direction of lift force always points upward, and the direction of drag force is always opposite to the stroke velocity u . (b) A zoomed-in image of the triangulated computational mesh. Finer elements are generated near the leading and trailing edges to resolve flow details. The mesh tip geometry in (b) facilitates convergence and does not compromise lift and drag accuracy.

5.3.2 2D simulation with passive pitching

To study fluid-wing interaction, we generalize the numerical model to account for wing passive pitching. At each computation time step, the incompressible Navier-Stokes equation is solved to obtain the instantaneous flow field and pressure field. The computed flow exerts fluid torque on a passive polymer hinge that is modeled as a torsional spring. Consequently, we can formulate an ordinary differential equation (ODE) that models the wing pitching:

$$i_{xx}\ddot{\psi} + k\psi + \tau_f = 0, \quad (5.14)$$

where k is the hinge stiffness and i_{xx} is the principal moment of inertia in the spanwise direction. This ODE is solved using a forward Euler method. This coupled PDE–ODE system allows us to numerically model the passive wing pitching motion.

In equation (5.14), i_{xx} is computed with respect to the wing leading edge using the parallel axis theorem and does not include an added mass correction as it is in the quasi-steady model. Since this is a 2D numerical model, i_{xx} and k are normalized to quantities per unit length. Here, i_{xx} is normalized by the wing span as $i_{xx} = I_{zz}/R$. Since the flapping motion has a 3D rotational component, it is important to adjust for 3D effects when setting the hinge stiffness. The normalized hinge stiffness value needs to be a function of the wing chord spanwise location and the wing shape; k should have the form of:

$$k = \frac{1}{\beta} \left(\frac{r}{R}\right)^2 \frac{K}{w}, \quad (5.15)$$

where K is the wing hinge stiffness, w is the hinge width, $r = R/2$ gives the spanwise scaling, and β is a dimensionless number that accounts for wing shape and other 3D effects. In the comparison between experiments and simulations, we experiment with several values of β and choose the best fitting value.

5.4 3D CFD models

While we primarily use 2D CFD models to study fluid-wing interactions, we also set up 3D CFD solvers and compare the similarities and differences between 2D and 3D simulations. In addition to describing flow structures shown in the 2D solver, the 3D model further considers spanwise flow and wing geometry influence. However, the

3D simulations are computationally expensive. In the following sections, we describe the 3D solver implementation.

5.4.1 3D simulation with fully prescribed kinematics

The 2D and the 3D models share similar computational structures. To generalize the numerical methods to the third dimension, we adopt 3D basis functions in a tetrahedron mesh. Figure 5.2 shows the wing mesh dimensions, the inertial coordinates (x, y, z) , the moving coordinates (ξ, η, ς) , and the wing surface mesh. The mesh radius is chosen to be 10 times the mean wing chord to avoid boundary effects. The 3D tetrahedral mesh is generated by the open source package gmsh [39]. The mesh consists of 140,000 tetrahedral elements and we use first-order Lagrange polynomials as the interpolation basis function. A first-order limiter based on Tu & Aliabadi [88] is implemented to remove artificial numerical oscillations. This 3D method has a first-order spatial convergence rate and a second-order temporal convergence rate.

While the explicit advection step is solved using the same method as that of the 2D solver, the implicit pressure and velocity updates are solved using iterative methods. Since the 3D solver involves significantly higher number of mesh elements, memory usage becomes a computational bottleneck. Direct Cholesky factorization can introduce large “fill-in” effect, which dramatically increases the memory storage. Instead, we use incomplete Cholesky factorization to compute a zero fill-in preconditioner. To solve the implicit Poisson and Helmholtz equations, we use the preconditioned conjugate gradient iterative method. Compared to the 2D model, the 3D simulation runtime and memory usage are over 30 times more costly. The 2D simulation requires

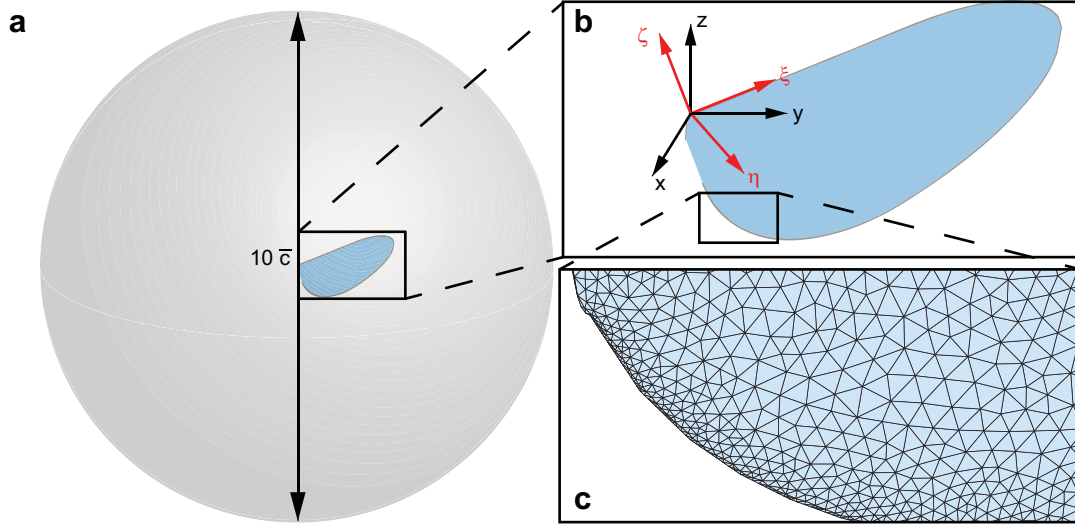


Figure 5.2: Computational mesh of 3D CFD simulations. (a) The spherical computational domain radius is 10 times the mean wing chord. (b) Definition of the inertial coordinate system (x, y, z) and the moving coordinate system (ξ, η, ζ) . Both have their origins at the leading edge of the wing root. (c) An enlarged view of the wing surface mesh. The computational mesh consists of 140,000 tetrahedral elements and 15,000 surface elements.

2 gigabytes of memory and spends approximately 2 hours per flapping period; the 3D simulation requires 50 gigabytes of memory and uses 3 days per flapping period. Details of solver validation are shown in appendix B.

Unlike the 2D numerical model, the 3D CFD model directly computes instantaneous forces without normalizing to chordwise lift or drag coefficients. By expanding equation (5.5), we obtain the expressions:

$$\begin{aligned}
 F_x &= - \int_{wing} \left((-p + 2\mu \frac{\partial u}{\partial x}) n_x + \mu \left(\frac{\partial u}{\partial y} + \frac{\partial v}{\partial x} \right) n_y + \mu \left(\frac{\partial u}{\partial z} + \frac{\partial w}{\partial x} \right) n_z \right) da \\
 F_y &= - \int_{wing} \left(\mu \left(\frac{\partial v}{\partial x} + \frac{\partial u}{\partial y} \right) n_x + (-p + 2\mu \frac{\partial v}{\partial y}) n_y + \mu \left(\frac{\partial v}{\partial z} + \frac{\partial w}{\partial y} \right) n_z \right) da \cdot \\
 F_z &= - \int_{wing} \left(\mu \left(\frac{\partial w}{\partial x} + \frac{\partial u}{\partial z} \right) n_x + \mu \left(\frac{\partial w}{\partial y} + \frac{\partial v}{\partial z} \right) n_y + (-p + 2\mu \frac{\partial w}{\partial z}) n_z \right) da
 \end{aligned} \tag{5.16}$$

Based on the coordinate system setup, the lift and drag magnitudes are given by:

$$\begin{aligned} F_L &= F_z \\ F_D &= \sqrt{F_x^2 + F_y^2} \end{aligned} \quad (5.17)$$

5.4.2 3D Simulation with passive pitching

To investigate fluid-wing interaction, we generalize the 3D solver to model passive pitching. We model the wing hinge as a torsional spring and formulate a coupled PDE-ODE system. The wing pitch component of the Euler angular momentum equation is given by:

$$K\psi + \tau_f = -I_{xx}\ddot{\psi} - (I_{yy} - I_{zz})\dot{\phi}^2 \cos\psi \sin\psi, \quad (5.18)$$

where K is the wing hinge stiffness, τ_f is the fluid torque along the wing pitch axis, and I_{xx} , I_{yy} , and I_{zz} are the wing principal moments of inertia. This second order ordinary differential equation describes the passive wing pitching motion. In each time step, the fluid torque τ_f is calculated based on the solutions of the velocity and the pressure fields. Next, τ_f serves as the input to equation (5.18), which calculates $\ddot{\psi}$. The solution of the wing pitching kinematics serves as the input to the PDE system for the next time step. This coupled PDE-ODE system describes the fluid-wing interaction mediated by a torsional hinge.

5.5 Model comparison

Our numerical model enables detailed studies of unsteady phenomena. In this section, we compare the measured and the computed lift to examine the accuracy of

the 2D and the 3D models. We also compare the measured the computed vorticity fields for a number of wings flapped with similar stroke but different pitch kinematics. Furthermore, we use the numerical simulator to explore portions of the parameter space that are not covered by our experimental setup. Through these numerical studies, we quantify the effects of the relative phase shift δ on the mean lift and drag coefficients $\overline{C_L}$ and $\overline{C_D}$.

5.5.1 Comparison of numerical models and experiments

First, we examine the similarities and differences between the 2D and the 3D models. In one of the flapping experiments we measure $\phi_{\max} = 34^\circ$, $\psi_{\max} = 43^\circ$, and $\delta = 0^\circ$ when the system is driven at 120 Hz. We use these kinematic parameters as the input and solve the 2D flow problem for the chord segment at wing midspan. Further, we use the 3D model to solve for the flow along the entire wing.

Figure 5.3a–f compare the 2D and 3D computed flow fields and pressure fields at wing midspan. The 2D and 3D flow fields are qualitatively similar although we observe stronger downwash in the 2D case. While the pressure profiles near the wing surface are similar, in the 2D case low-pressure regions are present in the wake. These low-pressure regions correspond to previously shed vortices. In the 3D case shed vortices decay much faster; hence, the wake does not have complex vortex structures.

Figure 5.3g, h show flow features that are unique to the 3D simulation. Figure 5.3g describes the spanwise flow at wing midspan, which is driven by the pressure gradient between the wing root and the wing tip. This flow weakens downwash because fluid momentum is dissipated in the spanwise direction. In addition, the spanwise flow

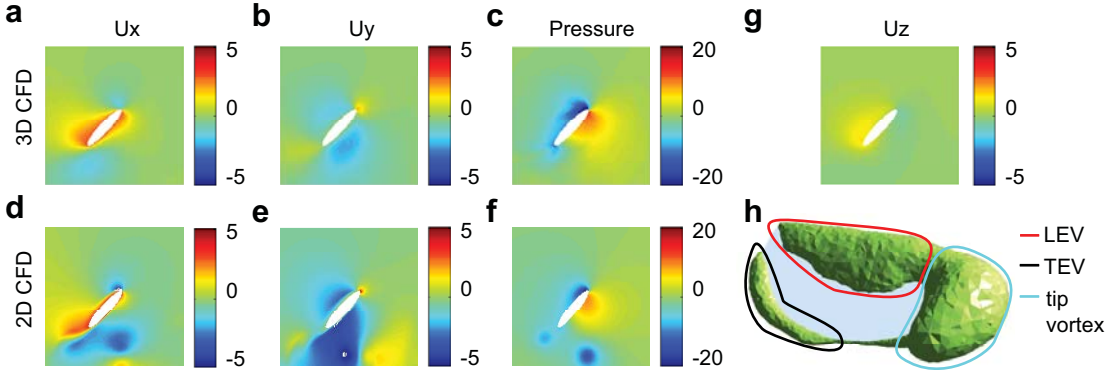


Figure 5.3: Qualitative comparison of 2D CFD and 3D CFD models. (a–f) Flow field and pressure field comparison; (a–c) show the 3D CFD results and (d–f) show the corresponding 2D CFD results. We show the solution on a chordwise plane at wing midspan. (g, h) Flow features that are unique to the 3D CFD model. In (g) it is shown that there is flow from wing root to wing tip on the upper wing surface. (h) The isovorticity contour near the wing surface, showing the LEV, the trailing edge vortex (TEV) and a tip vortex. The value of the isovorticity contour is 1200 s^{-1} . The units of the velocity fields U_x , U_y and U_z are m s^{-1} . The units of the pressure fields are N/m^2 . Both the 2D and 3D meshes use elliptical cross-sections for fair comparison. This meshing choice facilitates convergence of the numerical solver.

transports vorticity to the wing tip. Figure 5.3h shows the isovorticity contour along the wing surface. In addition to the LEV and TEV that are also observed in the 2D simulation, there is also a strong tip vortex on the upper wing surface.

The 3D simulation describes spanwise flow and shows the presence of a tip vortex. While these effects are ignored in the 2D simulation, the pressure profiles are qualitatively similar. We further compare computed lift forces with experimental measurements in figure 5.4a.

Figure 5.4a, c report the measured time varying lift force (red) and the simulated lift and drag forces. The green curves represent the 2D CFD simulations and the blue curves show the 3D CFD results. Both the 2D and 3D simulations show that primary lift and drag peaks occur early in the stroke deceleration phase. The growth

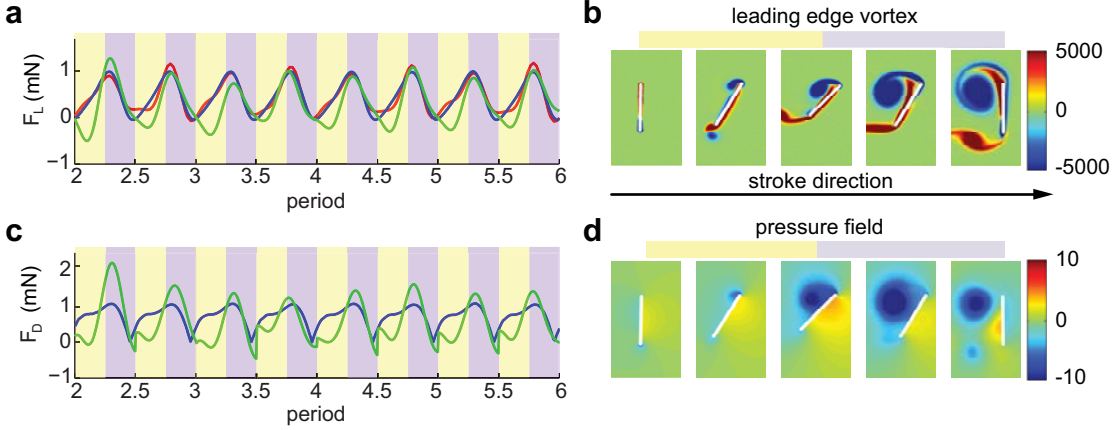


Figure 5.4: (a) Lift and (c) drag force comparison for the 2D CFD model (green), the 3D CFD model (blue) and the experimental measurement (red). The yellow regions represent the stroke acceleration phase and the violet regions represent the stroke deceleration phase. Relationship between (b) the LEV strength and (d) the associated pressure field. The LEV is fully developed during the stroke deceleration phase and it corresponds to a strong low-pressure region on the wing upper surface. The illustrations in (b, d) are computed from the 2D CFD model. The units of the vorticity and pressure fields are s^{-1} and N/m^2 , respectively.

and shedding of the LEV is the primary lift generation mechanism for flapping flight.

Figure 5.4b, d show the LEV on an impulsively started wing and the corresponding pressure field computed by the 2D CFD model. In the stroke acceleration phase, the vorticity on the upper wing surface is small. In the stroke deceleration phase, the LEV is fully developed and we observe a strong low-pressure region attached to the upper wing surface. Physically, a strong vortex always corresponds to a low-pressure region because streamline curvature implies an outward pointing radial pressure gradient.

Compared with experimental measurements, both the 2D and the 3D CFD models give accurate lift force predictions during the stroke deceleration phase (violet). Due to the lack of stabilizing spanwise flow, the LEV in the 2D simulation is shed prior to that of the experimental measurement. However, the 2D LEV also decays slower

due to the lack of spanwise flow. Consequently, the effect of early LEV detachment is compensated by the slow LEV decay. These 2D effects counteract each other and lead to accurate lift force prediction in the stroke deceleration phase.

However, the 2D CFD model is less accurate in the stroke acceleration phase (yellow) due to interactions with shed vortices and stronger downwash. In the stroke acceleration phase the 2D CFD model underpredicts both lift and drag forces. The experimentally measured mean lift is 0.46 mN; the 2D and 3D CFD model estimates are 0.31 mN and 0.46 mN respectively. In addition, the relative root mean square error of model estimation can be computed as:

$$e_{rms} = \frac{\sqrt{\int_T (F_{measure} - F_{model})^2 dt}}{\sqrt{\int_T F_{model}^2 dt}}, \quad (5.19)$$

where the integration interval is between the third and the sixth period. The 2D and 3D model errors are 34%, and 4.5% respectively. In the 2D simulation, the stroke acceleration phase (yellow) and deceleration phase (violet) contribute 86% and 14% of the total model error, suggesting that the shed vortex interaction in the stroke acceleration phase causes the greatest 2D model error. For completeness, figure 5.4a also shows the drag force predicted by the 2D and 3D models. The mean drag forces computed by the 2D and 3D models are 0.57 mN and 0.71 mN respectively. Due to the reasons discussed in Chapter 2, we do not report experimental time varying drag measurements.

5.5.2 Vorticity field comparison

The vorticity field offers a very informative description of fluid–wing interaction and lift and drag generation. Since the flow is modeled as incompressible, comparing the experimentally measured and computed vorticity fields is equivalent to comparing both the x and y components of fluid velocity fields. In addition, as we have discussed in section 5.5.1, there is an intuitive connection between the vorticity field and the pressure field. Here, we experimentally compare the measured vorticity fields with the computed vorticity fields.

We perform experiments on four different wing designs with different aspect ratios ($AR = 3, 3.5, 4.5, 5$). All wings are flapped at 120 Hz, and we vary the input drive voltage to achieve similar stroke motion for each wing. We measure the flapping kinematics and the associated flow fields using techniques described in Chapter 2, and then we run 2D numerical simulations with the measured kinematic parameters ϕ_{\max} , ψ_{\max} , f , and δ . These experiments evaluate the 2D CFD model accuracy and explore the effect of the phase shift δ on LEV strength. Different wing shapes are used in the experiments to achieve different values of δ while maintaining similar stroke motions. These passive pitch experiments and 2D simulations are not intended to explore wing shape influence on mean lift.

Figure 5.5 compares the numerically computed vorticity field with the measured vorticity field for the wing with $AR = 3$. We show the vorticity field during the 10th computational period to avoid initial transients. While there is some noise in the measured vorticity field due to motion blur and numerical differentiation, we observe qualitative agreement between experiments and simulations. In figure 5.5(a, c, e, g, i,

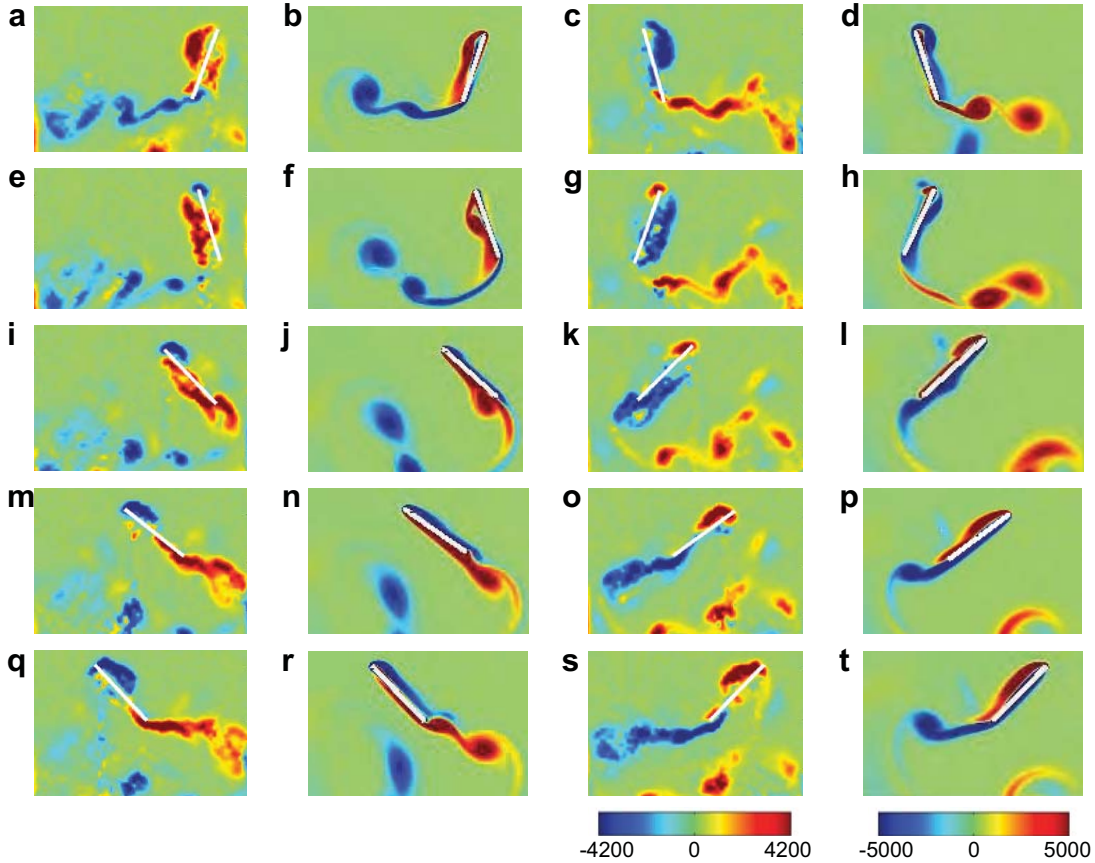


Figure 5.5: Vorticity comparison between experimental measurements and simulations for $Re = 520$. The wing aspect ratio is 3, and the wing is flapped at 120 Hz with leading edge displacement equal to 3.7 mm. The relative phase shift is 22° . Red color corresponds to counterclockwise rotating vortices and blue color corresponds to clockwise rotating vortices: (a, c, e, g, i, k, m, o, q, s) the experimentally measured vorticity fields: (b, d, f, h, j, l, n, p, r, t) the computed vorticity fields (2D CFD), for (a, b) $T = 10.0$, (e, f) 10.1, (i, j) 10.2, (m, n) 10.3, (q, r) 10.4, (c, d) 10.5, (g, h) 10.6, (k, l) 10.7, (o, p) 10.8, (s, t) 10.9. The unit of the vorticity plots is s^{-1} . The color scale of the vorticity plots is estimated based on camera frequency and lens magnification.

k, m, o, q, s), experimental measurements show a growth of the LEV during the wing translation phase and vortex shedding during wing reversal. Similar vortex growth and shedding patterns are observed through the numerical simulations shown in 5.5(b, d, f, h, j, l, n, p, r, t). There are some differences between the measurements and the simulations. In the experiments, the LEV is concentrated more closely around the leading edge, whereas in simulations the vorticity is more spread out along the upper wing surface. In addition, shed vortices decay quickly in our experiments whereas shed vortices are much stronger in the simulations. These differences may be due to the 2D flow assumption of our numerical solver. In 2D simulations, shed vortices (both LEV and TEV) are infinitely long vortex filaments and decay slowly. On the other hand, shed vortex structures in 3D flapping experiments have radially outward momentum due to the spanwise flow. The influence of the shed wake structure on the wing weakens as the LEV and the TEV move in both downward and outward directions. In addition, because a 3D vortex has finite length, it decays faster due to viscous dissipation. As a result, interactions between previously shed vortices and the wing are weaker in 3D flow. Details about 3D wake structures around a flapping wing can be found in Cheng et al [13].

We quantitatively measure the LEV strength for comparison between simulation and experiment. The flapping kinematics of all four wings have similar stroke motion (figure 5.6a) and identical driving frequency. Figure 5.6b shows the measured pitch motions. As wing aspect ratio increases, the relative phase shift between stroke and pitch motion decreases. Figure 5.6c shows the experimentally measured leading edge circulation as a function of time during a flapping period. We measure the

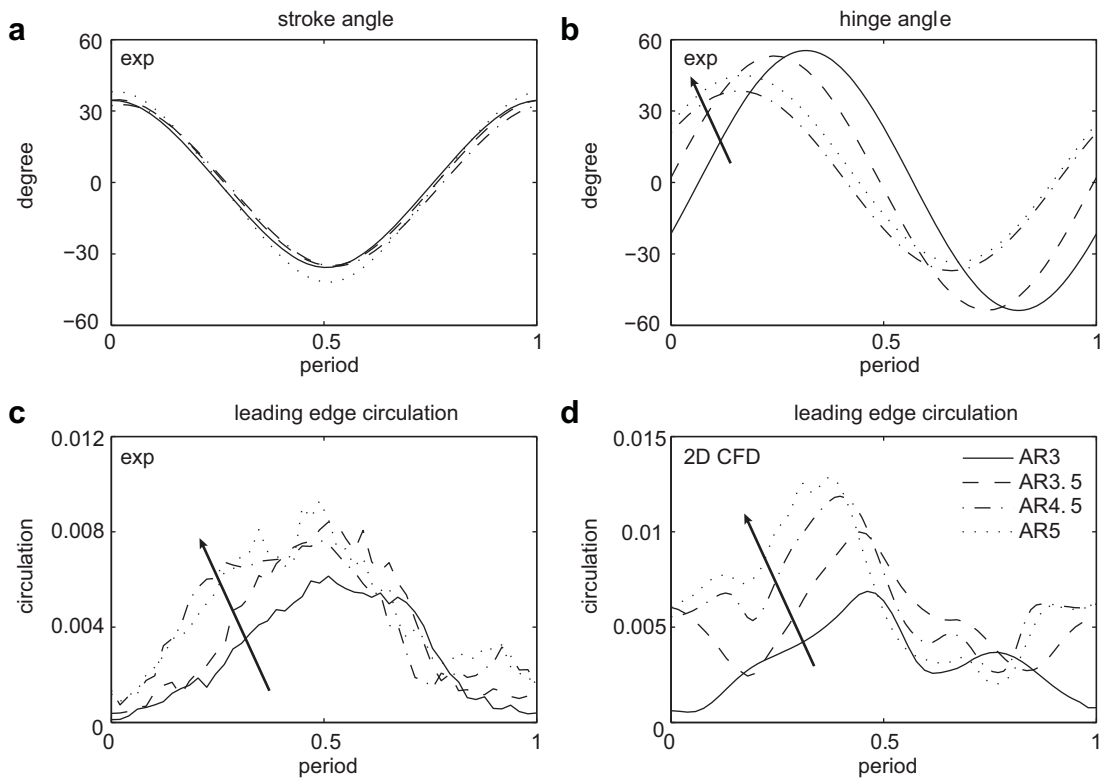


Figure 5.6: (a) Experimentally measured wing stroke motion as a function of time. (b) Wing pitch rotation as a function of time. The arrow indicates that increasing wing aspect ratio (AR) corresponds to decreasing phase shift δ . The stroke and pitching motions shown in (a, b) are projected to the lowest Fourier component for numerical simulation. (c) Experimentally measured leading edge circulation as a function of time. (d) Numerically computed circulation as a function of time. The unit of circulation in (c, d) is m^2/s . The arrows in (c, d) indicate that increasing aspect ratio AR corresponds to increasing leading edge circulation. The bounding box that defines the leading edge circulation region is shown in figure 4(d). In all graphs, time is normalized to one flapping period.

leading edge circulation by integrating the vorticity in a small rectangle around the leading edge. The bounding box dimension is chosen to include the entire LEV while excluding contributions from previously shed vortices. We only integrate over negative vorticity (clockwise rotating vortices) to avoid cancellation between positive and negative vorticity on opposite wing surfaces. The integration formula is given by:

$$\Gamma_{LEV} = \left| \int_{box} (\nabla \times \mathbf{u})_z \cdot ((\nabla \times \mathbf{u})_z \leq 0) da \right|, \quad (5.20)$$

where $(\nabla \times \mathbf{u})_z$ is the z component of the vorticity vector, and the conditional statement $(\nabla \times \mathbf{u})_z \leq 0$ avoids contributions of positive vorticity on the other side of the wing surface. The strength of the LEV between period = 0 and period = 0.5 directly correlates to the lift force production. At around the half-period point, the wing reverses and a previous LEV is shed and attaches to the lower wing surface. Experimentally, we observe that flapping experiments with advanced pitch rotation correspond to stronger leading edge circulation. Figures 5.6b, c show that wings with larger leading edge circulation also have more negative phase shift δ . This experimental observation is confirmed by the numerical simulations shown in figure 5.6d. The simulation results confirm that wings with more negative phase shift have larger leading edge circulation.

5.5.3 Numerical simulation with passive hinge rotation

In section 5.3.2, we introduced a 2D coupled fluid–mesh model that allows us to prescribe stroke motion and compute passive hinge rotation. Using the measured stroke kinematics of the AR = 3 wing in figure 5.6a as the input, we compute passive

pitch motion and the vorticity fields. The parameters in equation (5.14) are found using the method discussed in section 5.3.2. The normalized moment of inertia i_{xx} is 0.12 mg mm. We run a number of simulations and identify the best fitting to be 2.8. The normalized hinge stiffness k is calculated to be 100 mN/rad using equation (5.15).

Figure 5.7 shows qualitative agreement of the vorticity field between the experimental measurement and the passive hinge simulation. We observe similar LEV formation and vortex shedding behaviors. Due to the lack of spanwise flow, the 2D simulation is less stable than the 3D experiments. We observe that a small LEV detaches at $T = 10.7$, and at the same time a new LEV quickly develops on the wing upper surface. At $T = 10.8$ and $T = 10.9$, the new LEV on the upper wing surface is qualitatively similar to the measured LEV. Although we observe an instance of instability, the LEV profile during the downstroke ($10.75 \leq t \leq 11.0$) is qualitatively similar to the measurement. Hence, the influence of this early shedding on lift is not significant. This coupled fluid–mesh simulation demonstrates that the numerical solver can reasonably describe passive hinge rotation when given the stroke kinematics.

5.5.4 Effect of relative phase shift

In sections 5.5.2 and 5.5.3 we show that simulations with fully or partially prescribed kinematics yield good agreement with experimental measurements. Here we use numerical simulations to explore kinematic inputs that cannot be studied using the existing experimental setup. In Chapter 4, figure 4.6d showed that the mean lift

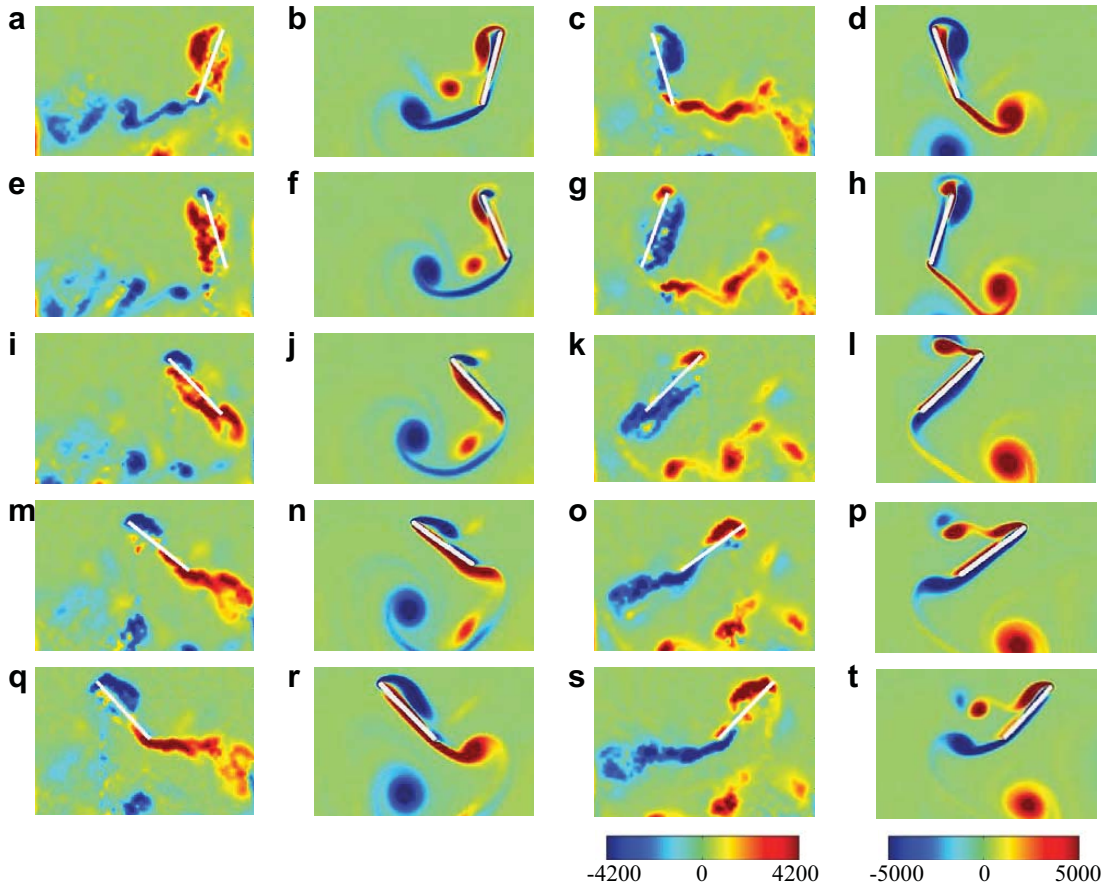


Figure 5.7: Vorticity comparison between experimental measurements and passive pitching simulations for $Re = 520$. Red corresponds to counterclockwise rotating vortices and blue corresponds to clockwise rotating vortices: (a, c, e, g, i, k, m, o, q, s) the experimentally measured vorticity fields; (b, d, f, h, j, l, n, p, r, t) the computed vorticity fields (2D CFD), for (a, b) $T = 10.0$, (e, f) 10.1, (i, j) 10.2, (m, n) 10.3, (q, r) 10.4, (c, d) 10.5, (g, h) 10.6, (k, l) 10.7, (o, p) 10.8, (s, t) 10.9. The unit of the vorticity plots is s^{-1} .

plummet when δ is large and positive. However, we cannot experimentally isolate the effect of δ because the pitching motion depends on the stroke and frequency operating points.

We study the effect of δ numerically through simulations with fully prescribed kinematics. Figure 5.8 shows the time-averaged lift and drag coefficients as a function of the δ while holding other kinematic parameters constant. Here, we set $\phi_{\max} = 34^\circ$, $\psi_{\max} = 43^\circ$, and $f = 120$ Hz. Figure 5.8a shows the $\overline{C_L}$ and $\overline{C_D}$ of an impulsively started wing for half of a flapping period and 5.8b shows the averages for six flapping periods. In the first half-stroke there are no downwash or wake capture effects; hence, figure 5.8a quantifies the effect of δ on translational lift and drag alone. Figure 5.8b shows the variation of $\overline{C_L}$ and $\overline{C_D}$ due to δ on both translational and rotational motion.

Both figures 5.8a, b show that $\overline{C_L}$ and $\overline{C_D}$ decrease as δ increases. Compared with $\delta = 0^\circ$, the 2D simulation of $\delta = -30^\circ$ shows a 61% increase of $\overline{C_L}$ and a 66% increase of $\overline{C_D}$. On the other hand, at $\delta = 30^\circ$, we observe a 44% decrease of $\overline{C_L}$ and a 7.1% decrease of $\overline{C_D}$.

Figure 5.8c further shows the $\overline{C_L}$ and $\overline{C_D}$ dependence on δ through 3D simulations. Since 3D CFD simulations are less influenced by shed vortex interactions and downwash effects, we only show the case of averaging over six periods. The 3D simulations show that $\overline{C_L}$ and $\overline{C_D}$ reduce by 52% and 38% from $\delta = -30^\circ$ to $\delta = 40^\circ$, respectively. The mean lift and drag coefficients are monotonically decreasing functions of δ . We observe that the half-period 2D result is more similar to the 3D simulation than the six-period 2D result. This suggests that unsteady vortex interactions and downwash

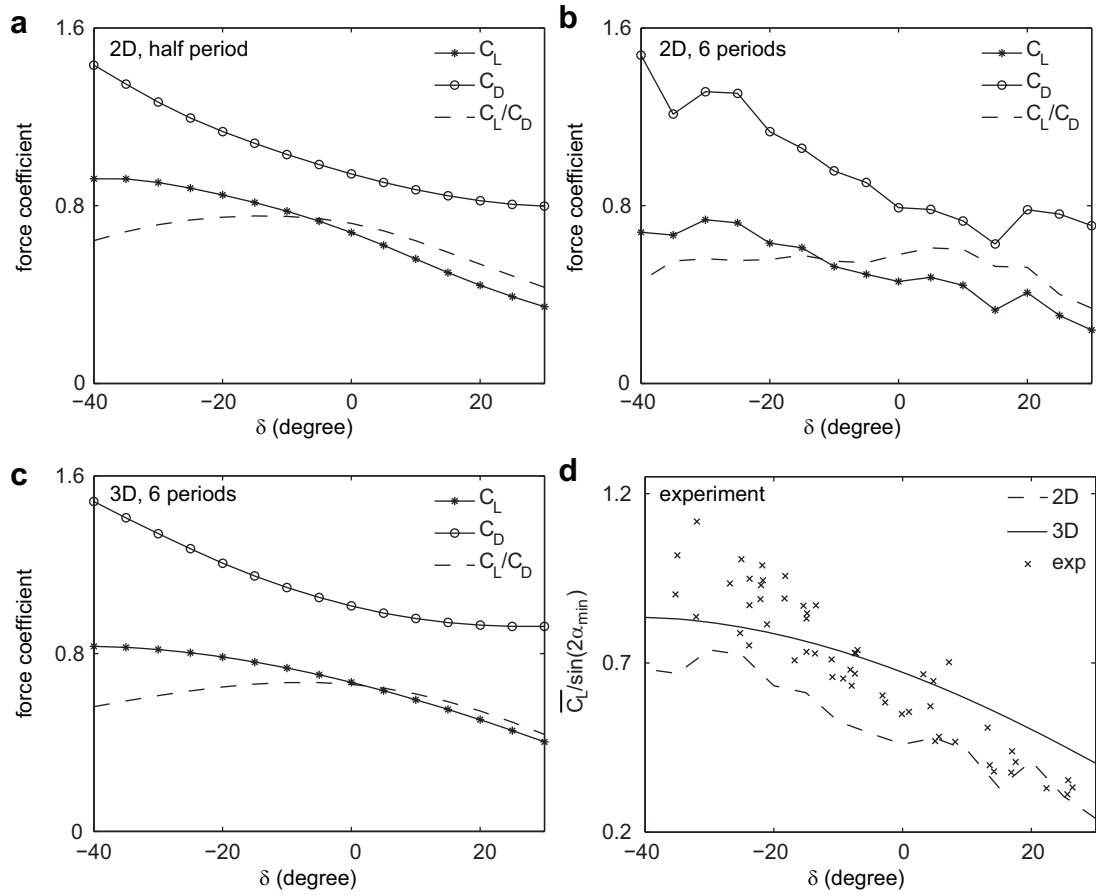


Figure 5.8: Plots of $\overline{C_L}$, $\overline{C_D}$ and $\overline{C_L/C_D}$ as functions of δ . All simulations are run with $\phi_{\max} = 34^\circ$, $\psi_{\max} = 43^\circ$, $f = 120$ Hz, while the phase parameter δ is varied from -40° to 30° . (a) Time-averaged lift and drag coefficients for an impulsively started wing for a half flapping period. (b) The same simulations averaged over six flapping periods. Panels (a) and (b) Show 2D CFD results. (c) Three-dimensional CFD simulation of mean lift and drag coefficients averaged over six flapping periods. (d) Comparison of $\overline{C_L}/\sin(2\alpha_{\min})$ between 2D and 3D simulations and measurements.

may be the main factors of discrepancy between 2D and 3D simulations.

Figure 5.8a-c also show the ratio $\overline{C_L}/\overline{C_D}$ as a function of δ . The ratio $\overline{C_L}/\overline{C_D}$ is an important MAV design parameter because it relates to flight endurance. Instead of maximizing mean lift, it is energetically more efficient to maximize $\overline{C_L}/\overline{C_D}$ in flight. Both 2D and 3D simulations show that $\overline{C_L}/\overline{C_D}$ is small when the phase shift δ is much less than 0° or much greater than 0° . In particular, the 3D CFD simulation shows that $\overline{C_L}/\overline{C_D}$ is a maximum at $\delta = -5^\circ$, which suggests $\delta \approx 0^\circ$ to be a desirable operating point. This suggests that optimization based on a quasi-steady model (which assumes $\delta = 0^\circ$) will be fruitful in a future study.

Finally, figure 5.8d compares the $\overline{C_L}/\sin(2\alpha_{\min})$ dependence on δ between experiments, 2D and 3D simulations. The data shown in figure 5.8d are taken from figures 4.6d and 5.8b, c. In passive pitching experiments, the minimum angle of attack varies in different driving conditions; hence, we normalize effects of different α_{\min} values by dividing by $\sin(2\alpha_{\min})$. Although 2D simulations underestimate $\overline{C_L}/\sin(2\alpha_{\min})$, both 2D and 3D simulations show a similar trend to the experiments.

In this chapter, we developed numerical solvers to explore the flow structures associated with flapping-wing flight. Both simulations and experiments show that a negative phase shift corresponds to a stronger LEV and thus larger lift and drag forces. Furthermore, we find that wings with stiffer hinges achieve favorable pitching kinematics that lead to larger mean lift forces. In addition to investigating flapping flight in air, the numerical simulations can be modified to study aquatic flapping in water. In the next chapter, we explore the similarities of flapping wing propulsion in aerial and aquatic environments.

Chapter 6

Flapping propulsion in aquatic environment

6.1 Introduction

Mobile robots capable of locomotion through complex environments are becoming increasingly essential for search-and-rescue, surveillance, and environment exploration applications [17]. Aerial vehicles [59, 65] are attractive for these applications because they can survey large areas and bypass heterogeneous ground with ease. However, unlike ground-based robots that have been shown to be able to move across rough terrain and within water [18], current aerial robots are incapable of multi-modal locomotion through air and water which limits their utility [81].

The concept of dual aerial, aquatic vehicles emerged in 1939 when Russian engineer Boris Ushakov proposed the “flying submarine” [1]. In recent years, several fixed-wing dual aerial, aquatic testing platforms have been developed [31, 61]. However, designs

that rely on traditional airfoils to generate lift and rotary propellers to generate thrust have been unsuccessful in achieving aquatic and aerial motion. The difference in density between air and water ($1.2 \text{ kg}\cdot\text{m}^3$ and $1000 \text{ kg}\cdot\text{m}^3$, respectively) poses challenges to choosing suitable wing size, vehicle cruise speed, and propeller speed. While underwater vehicle designs aim to minimize surface area to reduce drag, aerial vehicle designs need large airfoils to maintain lift. This design conflict, in addition to the reduction of rotary motor efficiency at small scales, makes fixed-wing designs ineffective for hybrid aerial, aquatic micro-vehicles.

There are a number of biological examples of hybrid aerial and aquatic locomotion including numerous fish, birds, and insect species [19, 64, 101]. In particular, puffins and guillemots [64] are aquatic birds that both fly and swim by flapping-wings with adaptive kinematics for air and water. A flying fish [19] whips its tail to jump out of the water surface, and then it unfolds its pectoral fins to glide in air.

To achieve multi-modal locomotion in a flapping wing vehicle, wing kinematics must be adapted based on the fluid mechanics and system dynamics within these environments due to changes in fluid density and viscosity. For instance, lift-enhancing, unsteady mechanisms such as the development and shedding of the leading edge vortex (LEV) change with varying Reynolds number. While many previous studies explored these effects using dynamically scaled models [24], these experiments do not allow simultaneous inertia matching to investigate system dynamics or wing flexibility in water and air. Hence, to develop design principles for robotic aerial and aquatic locomotion, it is necessary to develop a theoretical and experimental basis of flapping-wing fluid mechanics in these environments.

In this chapter, we compare the fluid mechanics of flapping propulsion in aerial and aquatic environments. We first give a high-level scaling analysis to estimate the appropriate operating frequency that leads to suitable passive wing pitching kinematics in both fluids. Next, we quantify fluid-wing interaction in air and in water by conducting 3D-CFD simulations. Finally, we set up aquatic flapping experiments to assess model accuracy.

6.2 Scaling analysis of aerial and aquatic flapping

To reconcile the large density difference between air and water, a flapping-wing robot needs to operate at different frequencies. We identify the frequency range at which a flapping-wing aerial robot can operate in an aquatic environment using the quasi-steady formula:

$$\overline{F_L} = \frac{1}{2} \overline{C_L} \rho U_{rms}^2 S. \quad (6.1)$$

In equation (6.1), $\overline{F_L}$ is mean lift force, $\overline{C_L}$ is the time averaged lift coefficient, ρ is the fluid density, U_{rms} is the root mean square of wing tip velocity, and S is the wing surface area. Since the wing planform, inertia, and hinge stiffness are unchanged as the vehicle transitions from air to water, we need to change input frequency and stroke amplitude to maintain the desired mean lift forces. Invoking equation (6.1) leads to

$$\rho_{air} (\phi_{max,air} Rf_{air})^2 = \rho_{water} (\phi_{max,water} Rf_{water})^2, \quad (6.2)$$

For an under-actuated flapping wing aerial robot like the RoboBee, ϕ_{max} is actively controlled by vehicle actuation. If ϕ_{max} is chosen to remain constant, then the flapping

frequency in water can be estimated as:

$$f_{water} = \sqrt{\frac{\rho_{air}}{\rho_{water}}} f_{air}. \quad (6.3)$$

The quasi-steady model also estimates the fluid power dissipation in air and water:

$$P = \bar{F} \cdot \bar{v} \cong \frac{1}{2} \overline{C_L} \rho U_{rms}^3 S. \quad (6.4)$$

Substituting equation (6.3) into equation (6.4), we obtain that the fluid power dissipation ratio in air and water is inversely proportional to the square root of the fluid density ratio:

$$\frac{P_{air}}{P_{water}} \cong \sqrt{\frac{\rho_{water}}{\rho_{air}}}. \quad (6.5)$$

This scaling analysis estimates the underwater flapping frequency and suggests underwater locomotion has less fluid dissipation.

6.3 Numerical simulation of aerial and aquatic flapping

The scaling analysis does not consider the Reynolds number influence on fluid-wing interaction. Reynolds number is an important factor for flapping-wing flight and is the ratio of inertial to viscous forces:

$$Re = \frac{U_{rms} R}{\nu}. \quad (6.6)$$

In equation (6.6), ν is the kinematic viscosity of the immersed fluid. Substituting equation (6.3) into equation (6.6), we can obtain the ratio between the aquatic flapping Reynolds number and the aerial flapping Reynolds number:

$$\frac{Re_{water}}{Re_{air}} = \frac{U_{water}\nu_{air}}{U_{air}\nu_{water}} = \sqrt{\frac{\rho_{air}}{\rho_{water}}} \frac{\nu_{air}}{\nu_{water}} = 0.54. \quad (6.7)$$

Equation (6.7) shows that the Reynolds numbers in air and water are on the same order, which implies aerial and aquatic flapping share similar flow characteristics. Since the Navier Stokes equation models both fluid density and viscosity, we run a series of 3D-CFD simulations to compare flow structures and wing dynamics in air and water.

6.3.1 Aerial flapping versus aquatic flapping

A hovering RoboBee flaps at 120 Hz in air with 70° peak to peak stroke amplitude. A previous aerial flapping experiment measured the corresponding pitching kinematic parameters to be $\psi_{max} = 43^\circ$ and $\delta \approx 0^\circ$. Assuming ϕ_{max} , ψ_{max} , and δ are identical in air and water, equation (6.1) predicts the hovering frequency in water to be 4.1 Hz. Using the 3D-CFD solver from Chapter 5, we compare flapping flight in air and water under the same kinematic parameters ϕ_{max} , ψ_{max} , and δ but at different frequencies. Figure 6.1 compares the computed lift, drag and wing hinge torque. Although the Reynolds numbers differ by 46%, we observe that these quantities are very similar between flapping in air (green) and water (blue).

Figure 6.2 illustrates the similarities between aerial and aquatic velocity, pressure, and vorticity fields. Figure 6.2a, d compare the flow (U_x , U_y , U_z components) and

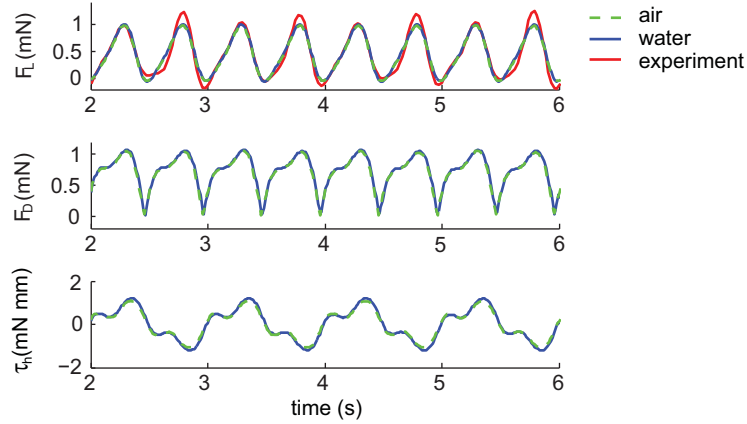


Figure 6.1: Lift, drag, and wing pitch torque in water and air from CFD computation. (a) Instantaneous lift force generation. (b) Instantaneous drag force generation. (c) Instantaneous fluid torque along the wing pitch axis. In (a), (b) and (c) green and blue colors represent simulation for aerial flapping at 120 Hz and aquatic flapping at 4.1 Hz, respectively. The time scales are normalized in the unit of a flapping period. We show the second to the sixth flapping period to avoid initial transients.

the pressure fields (PR) when the wing stroke velocity is at a maximum ($T = 2.25$). These plots show the solutions on a 2D plane that intersects the wing chord at mid-span. The aerial and aquatic flapping speed at wing mid-span are approximately 2 m/s and 7 m/s, respectively. Since water density is approximately 850 times greater than that of air, the pressure fields in both fluid media have similar magnitudes (10 N/m²).

In the intermediate Reynolds number regime, pressure dominates viscous shear. Our simulations show that pressure accounts for over 90% of the lift and drag on the wing. Figure 6.2b, e compare the pressure distribution on the wing surfaces when stroke velocity is at the maximum ($T = 2.25$). In both cases the upper wing surface has a negative pressure profile (blue) and the lower wing surface has a positive pressure profile (red). We use the same color scale for both aerial (left) and aquatic (right) simulations.

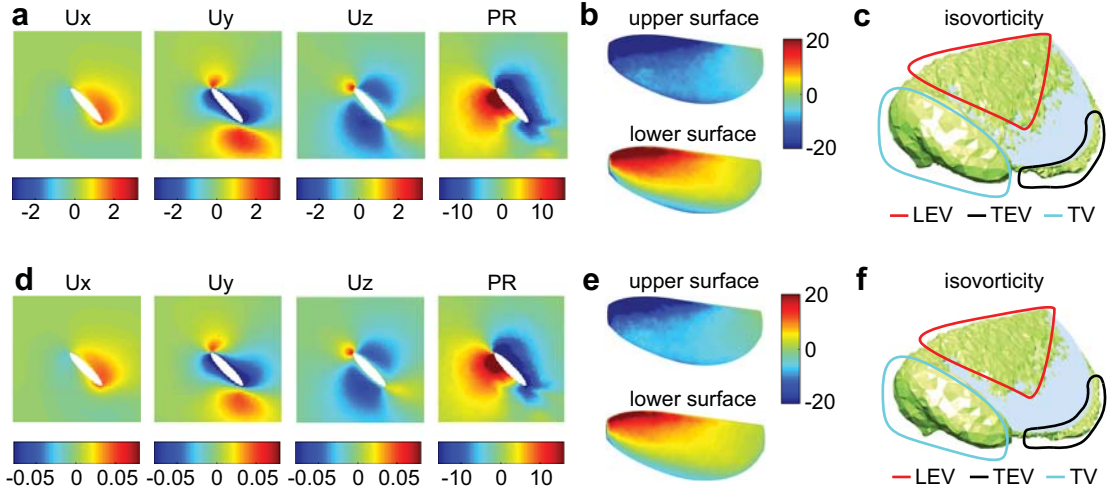


Figure 6.2: Comparison of aerial and aquatic flapping under identical ϕ , ψ , and δ but at a different frequency f . The top and bottom row illustrate the flow structures of aerial and aquatic flapping, respectively. (a) Instantaneous flow field (U_x , U_y , U_z) and pressure field (PR) of aerial flapping. (b) The pressure profile on the wing surface in aerial flapping. (c) The iso-vorticity contour on the wing surface in aerial flapping. (d) The flow and the pressure fields of aquatic flapping. (e) The pressure profile on the wing surface in aquatic flapping. (f) The iso-vorticity contour on the wing surface in aquatic flapping. In all sub-figures, we show the solutions taken at mid-stroke ($T = 2.25$). In (a) and (b), we show the solutions on a 2D plane that intersects the wing chord at wing mid-span. The units for the velocity and the pressure fields are m s^{-1} and N m^{-2} , respectively. In (c) and (f), the values of the aerial (left) and aquatic (right) iso-vorticity contours are 1200 s^{-1} and 41 s^{-1} , respectively. Both values normalize to 10 when the time scales are non-dimensionalized.

Although the pressure contribution dominates, viscous shear is important in the unsteady boundary layer and is responsible for the growth and shedding of vortices. Figure 6.2c, f illustrate the iso-vorticity contour on the upper wing surface. In both cases we observe the development of a LEV, a weak trailing edge vortex (TEV), and a very strong wing tip vortex. Our numerical simulations show vortex structures and pressure profiles are similar for aerial and aquatic flapping locomotion at the chosen kinematics.

In Chapter 5, we quantify the effects of phase shift δ on lift production. To com-

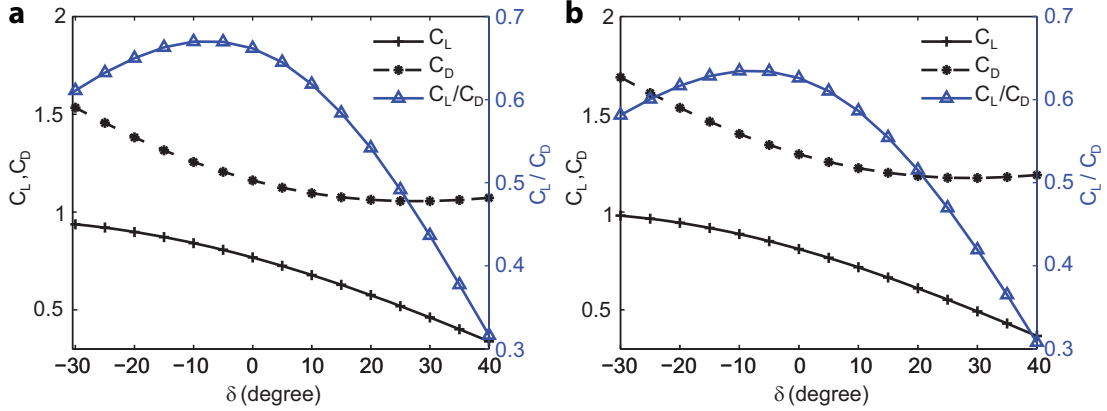


Figure 6.3: Influence of phase shift δ on lift and drag force production in air and water. (a) and (b) Simulation results of $\overline{C_L}$, $\overline{C_D}$ and $\overline{C_L/C_D}$ as functions of δ in aerial and aquatic flapping, respectively. Aerial and aquatic flapping propulsion have similar dependence on the kinematic parameter δ .

pare the influence of δ in aerial and aquatic flapping, we perform 3D-CFD simulations that vary δ while holding the other kinematic parameters constant. Figure 6.3 compares the mean lift and drag coefficients of aerial and aquatic flapping. The aerial flapping results presented in figure 6.3a is taken from Chapter 5. Figure 6.3b shows $\overline{C_L}$ and $\overline{C_D}$ as functions of δ . $\overline{C_L}$ is a monotonically decreasing function as δ increases, which indicates that aquatic flapping produces large mean lift when δ is negative. $\overline{C_D}$ is a decreasing function for $\delta < 0^\circ$ and flattens out for $\delta > 0^\circ$. Figure 6.3b also shows δ 's influence on $\overline{C_L/C_D}$, which is a measure of flight endurance. We observe that maximum flapping efficiency is achieved at $\delta = -10^\circ$. These simulations show that the effects of δ on lift and drag production in water and air are similar.

6.4 Experiment and discussion

6.4.1 Experimental setup

To validate the scaling analysis and the numerical simulations, we perform flapping experiments in air and water using the same actuator, wing, and wing hinge. For aerial flapping experiments, we use an existing setup (Chapter 2) for motion tracking and lift measurement. For aquatic flapping experiments, we extend the wing driver transmission to fully submerge the wing. We measure input voltage and current to study the system energetics for both aerial and aquatic experiments.

As shown in figure 6.4, we operate the actuator outside of water to prevent shorting. The wing is driven at 3-6 Hz and the motion is recorded at 200 Hz with a Phantom V7.3 high speed camera. Wing stroke and pitch motions are extracted using a similar method described in Chapter 2. We do not measure time varying forces for aquatic flapping experiments because of the difficulty to incorporate sensitive electronics.

6.4.2 Experimental comparison

To compare flapping dynamics in air and water, we first conduct aerial flapping experiments. When the wing is flapped at 120 Hz, we measure $\phi_{\max} = 35^\circ$, $\psi_{\max} = 35^\circ$, and $\delta \approx 0^\circ$. Next, we submerge the wing in water and operates the system at 4.1 Hz. In both experiments, the wing hinge stiffness and the wing area are fixed to 2.4 $\mu\text{Nm}/\text{rad}$ and 54mm², respectively. Figure 6.5a, b compare the flapping kinematics in air and water. Figure 6.5a shows a typical aerial flapping experiment. Figure 6.5b shows that similar flapping kinematics can be achieved in water. Since both

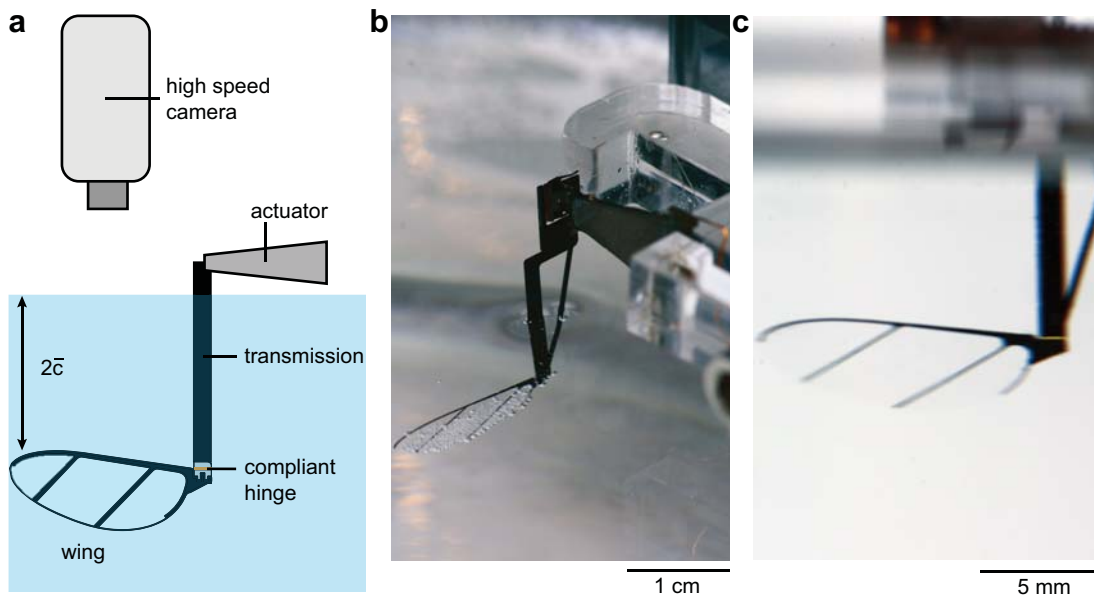


Figure 6.4: Experimental setup in water. (a) Schematic of the actuator, the transmission, the compliant flexure, and the robot's wing. A high speed video camera is positioned overhead to record the flapping kinematics. (b) and (c) The perspective and anterior view of the flapping wing setup. The wing leading edge is placed at a distance $2c$ below the water surface to avoid surface effects. The wing planforms in (a) and (c) are identical however there is some optical distortion when the wing is placed in a cylindrical beaker.

experiments involve passive wing pitching, similar pitching kinematics implies that both systems generate similar lift and drag forces.

To validate the numerical model, we extract flapping kinematics from the aquatic flapping experiment. Using the driving frequency and the measured stroke amplitude as inputs, we solve for the passive pitching kinematics. Here we use the coupled PDE-ODE solver that is described in section 5.4.2.

Figure 6.5c compares the measured and the simulated stroke and pitch motion. We observe close agreement between the experiment and the simulation, and the relative error for $\phi(t)$ and $\psi(t)$ are 8% and 17%, respectively. The measured and computed phase shift δ are 3° and -1.5° , respectively. This comparison shows that our numerical solver can capture the kinematics and dynamics of aquatic flapping.

We further compare the power consumption in air and water. By measuring the current drawn by the wing driver, we calculate the average power usage:

$$P_{total} = \frac{1}{T} \int_0^T i_{act} v_{act} dt, \quad (6.8)$$

where T , v_{act} and i_{act} are the flapping period, the applied voltage, and the measured current, respectively. We measure $P_{water} = 4.1$ mW and $P_{air} = 25.4$ mW. In section 6.2, we model the fluid power dissipation through a simple scaling analysis. While the analysis suggests that aerial flapping consumes 25 times more power, the experimental result shows aerial flapping is only 6 times more costly. This increase of aerial flapping efficiency is most likely to be contributed by the improved actuator efficiency when operated near resonance and the low coupling factor of the actuator.

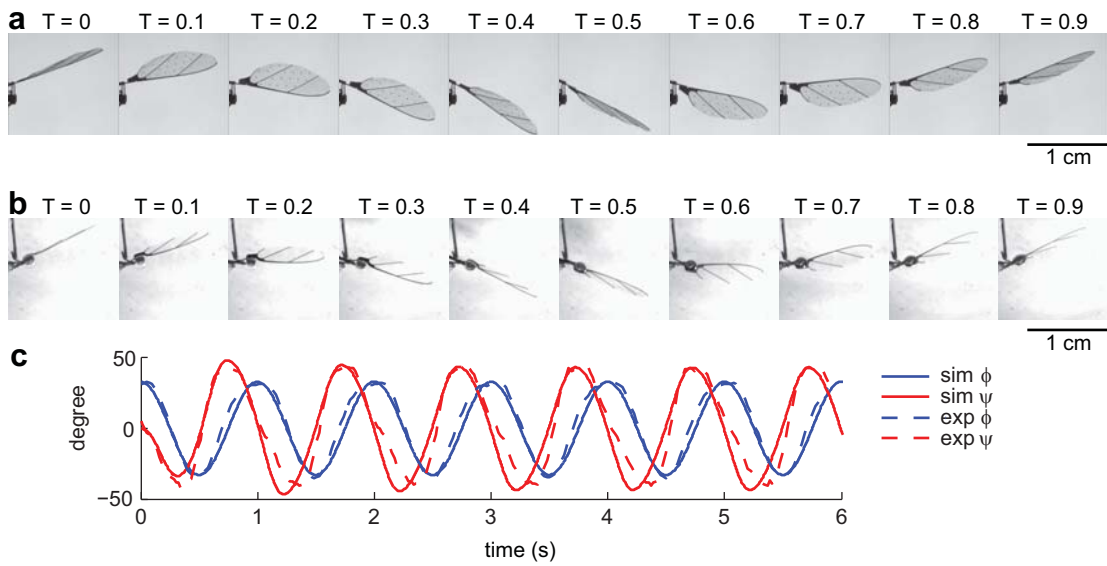


Figure 6.5: Comparison of flapping experiments in air and water. (a) Image sequence of an aerial flapping experiment operated at 120 Hz. (b) Image sequence of an aquatic flapping experiment operated at 4.1 Hz. (a) and (b) show flapping kinematics in air and water are similar under properly scaled driving frequencies. (c) Measured and simulated stroke and pitch kinematics of aquatic flapping. The passive wing pitch rotation matches closely between the simulation and the experiment.

In this chapter, we compare the similarities of flapping propulsion in aerial and aquatic environments. We propose a scaling relation that relates flapping frequency in air and water. Further, we use 3D-CFD numerical models to compare the corresponding fluid dynamics. The simulated results are corroborated by experimental measurements. In the next chapter, we explore flapping wing aquatic locomotion of an entire robot.

Chapter 7

A dynamical model for aquatic locomotion

7.1 Introduction

In the previous chapter we analyze the fluid dynamics of a single flapping wing in aquatic environment. The analysis shows a single flapping wing can generate adequate lift and drag forces for aquatic locomotion. Here we study the upright stability of the entire robot by developing a time varying, quasi-steady dynamical model. Specifically, we examine body-wing coupling and body pitching effects at low flapping frequencies. Experimental and simulation results suggest that increasing flapping frequency will improve the vehicle performance.

First, we derive a time-varying dynamical model for the robot aquatic locomotion. In addition to interpreting the simulation results, we further validate the model by running robot swimming experiments. This work lays the foundation for a novel

vehicle design that will be introduced in following chapter.

7.2 Robot dynamical model

There are a number of previous studies [36, 65, 75] that developed system level controllers for hovering flight. A model-free controller was developed [75] to demonstrate flight with altitude control. Chirratantanon et al. developed an adaptive controller based on a time-averaged dynamical model [14]. Parameters of the dynamical model were refined based on system identification methods.

While these models are effective for aerial hovering studies, they are inadequate for investigating aquatic locomotion. Previous time-averaged models neglect body-wing coupling because the flapping frequency is significantly higher than the body resonance frequency. Consequently, the effect of body oscillation on wing flapping kinematics is small. However, the robot flapping frequency is much lower in water, which leads to significant body-wing coupling. In particular, robot pitching adversely affects lift force generation.

Chirratantanon et al. [14] showed that the robot is intrinsically unstable in air and requires feedback control for stability. However, the current infrared based Vicon motion tracking system does not operate near or under the water. Consequently, the robot needs to be passively upright stable while swimming in water. Here we quantify wing-body coupling and investigate robot stability conditions in water by developing a time varying dynamical model.

7.2.1 Coordinate system definition

We formulate a time varying model that has 10 degrees of freedom. The robot body has six translational and rotational degrees of freedom denoted by x , y , z , ϕ , θ , and ψ . Here x , y , and z are the translational degrees of freedom and ϕ , θ , ψ are Euler angles following the roll, pitch, and yaw convention. Figure 7.1a, b define the robot body and wing coordinate axes. As discussed in Chapter 2, wing flapping kinematics each have two degrees of freedom relative to the robot body for a total of four degrees of freedom corresponding to the robot's left and right wing. We let α_i and β_i denote wing stroke and pitch angle, respectively. The subscript i distinguishes the left and the right wing. These ten generalized coordinates are defined as a column vector:

$$\mathbf{q} = [x, y, z, \phi, \theta, \psi, \alpha_r, \beta_r, \alpha_l, \beta_l]^T. \quad (7.1)$$

In this chapter, we denote right and left wing by the abbreviations r , and l , respectively.

7.2.2 Rigid body dynamics

We adopt the matrix form of Lagrangian mechanics to derive the equation of motion (Chapter 7 of Spong et al. [82]):

$$D(\mathbf{q})\ddot{\mathbf{q}} + C(\mathbf{q}, \dot{\mathbf{q}})\dot{\mathbf{q}} + \mathbf{g}(\mathbf{q}) = \boldsymbol{\tau}. \quad (7.2)$$

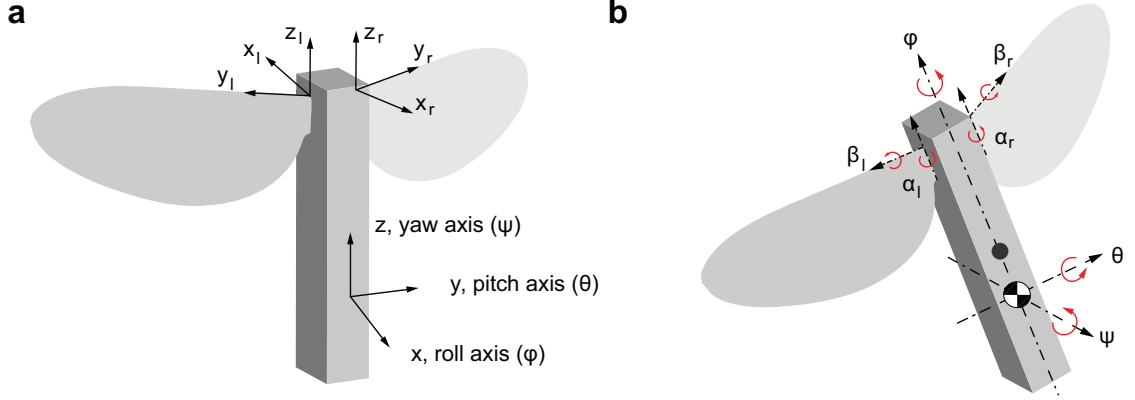


Figure 7.1: Dynamical model of the robot. a) Coordinate system definition of the robot body (x, y, z), the left wing (x_l, y_l, z_l) and right wing (x_r, y_r, z_r) reference frame. b) Definition of the generalized coordinates ($\psi, \theta, \phi, \alpha_r, \beta_r, \alpha_l, \beta_l$). The origin of the body coordinate system is located at the robot center of mass. The geometric center of the robot body is the body center of pressure.

The inertia matrix D is given by the sum of contributions from body, right and left wing:

$$D = \sum_{i \in \{b, r, l\}} \{J_{v,i}^T R_i M R_i^T J_{v,i} + J_{w,i}^T R_i I R_i^T J_{w,i}\}, \quad (7.3)$$

where M and I are the mass and moment of inertia matrix, respectively. Here mass is a tensor quantity to account for geometry-dependent added mass effects. R_i is the corresponding rotation matrix from the center of mass reference frame to the inertial system. $J_{v,i}$ and $J_{w,i}$ are velocity and angular velocity Jacobians. The Christoffel matrix elements are obtained from the partial differentials of the inertia matrix:

$$C_{kj} = \sum_{i=1}^n C_{ijk}(\mathbf{q}) \dot{q}_i = \sum_{i=1}^n \frac{1}{2} \left\{ \frac{\partial D_{kj}}{\partial q_j} + \frac{\partial D_{ki}}{\partial q_j} - \frac{\partial D_{ij}}{\partial q_k} \right\} \dot{q}_i. \quad (7.4)$$

The j^{th} component of the gravity vector is given by:

$$g_j = \frac{\partial P}{\partial q_j}, \quad (7.5)$$

where P is the total potential energy. The generalized force vector $\boldsymbol{\tau}$ is given by the matrix product of the partial displacement matrix and the external force vector. The dimensionalities of these quantities are given by: $D \in R^{10 \times 10}$, $C \in R^{10 \times 10}$, $g \in R^{10 \times 1}$, $\boldsymbol{\tau} \in R^{10 \times 1}$. The equations of motion form a system of coupled ordinary differential equations. We solve this system numerically through the Matlab function `ode45`.

Next, we derive the velocity Jacobians and angular velocity Jacobians of the robot body, its right and left wing.

7.2.2.1 Body J_v and J_w

The body velocity Jacobian $J_{v,b}$ transforms velocities with respect to the generalized coordinate to velocities with respect to the inertial coordinate. Here we have $J_{v,b} \in R^{3 \times 10}$ and it is given by:

$$J_{v,b} = \begin{pmatrix} | & | & | & | & | & | & | & | & | & | & | \\ \mathbf{e}_1 & \mathbf{e}_2 & \mathbf{e}_3 & \mathbf{0} \\ | & | & | & | & | & | & | & | & | & | & | \end{pmatrix}. \quad (7.6)$$

The body angular velocity Jacobian is given by

$$J_{w,b} = \begin{pmatrix} | & | & | & | & | & | & | & | & | & | \\ \mathbf{0} & \mathbf{0} & \mathbf{0} & R_\psi R_\theta \mathbf{e}_1 & R_\psi \mathbf{e}_2 & \mathbf{e}_3 & \mathbf{0} & \mathbf{0} & \mathbf{0} & \mathbf{0} \\ | & | & | & | & | & | & | & | & | & | \end{pmatrix}, \quad (7.7)$$

where R_ψ and R_θ are rotation matrices with respect to the ψ and θ axes. In the next sections we will use the rotation matrices R_ϕ , $R_{\alpha r}$, $R_{\alpha l}$, $R_{\beta r}$, and $R_{\beta l}$. These are rotations with respect to the axes defined in figure 7.1b.

7.2.2.2 Body and wing displacement vectors

The right and left wing velocity and angular velocity Jacobians contain a number of displacement vectors that define the distance between the robot center of mass, wing root, and wing center of mass. These vectors are defined as:

- \mathbf{d}_{rb} : displacement from the body center of mass to the right wing center of mass
- \mathbf{d}_{lb} : displacement from the body center of mass to the left wing center of mass
- \mathbf{d}_{rw} : displacement from the right wing root to the right wing center of mass
- \mathbf{d}_{lw} : displacement from the left wing root to the left wing center of mass

These displacement vectors can be calculated from a sequence of translations and rotations from the default robot configuration. Let \mathbf{r}_{rb} , \mathbf{r}_{lb} , \mathbf{r}_{rw} , and \mathbf{r}_{lw} be the

corresponding robot parameters in the fixed frame. The transformation is given by:

$$\begin{aligned}
 \mathbf{d}_{rb} &= R_b(\mathbf{r}_{rb} - \mathbf{r}_{rw}) + R_b R_{\alpha r} R_{\beta r} \mathbf{r}_{rw} \\
 \mathbf{d}_{lb} &= R_b(\mathbf{r}_{lb} - \mathbf{r}_{lw}) + R_b R_f R_{\alpha l} R_{\beta l} \mathbf{r}_{lw} \\
 \mathbf{d}_{rw} &= R_b R_{\alpha r} R_{\beta r} \mathbf{r}_{rw} \\
 \mathbf{d}_{lw} &= R_b R_f R_{\alpha l} R_{\beta l} \mathbf{r}_{lw}
 \end{aligned} \tag{7.8}$$

where R_b is the body rotation matrix:

$$R_b = R_\psi R_\theta R_\phi. \tag{7.9}$$

The rotation matrix R_f accounts for the 180° rotation between the left wing coordinate and the body coordinate.

7.2.2.3 Jacobian matrices of the right wing

Figure 7.1a shows the coordinate definition of the right wing with respect to the body frame. The wing rotates with respect to the stroke axis (z_r) and then the pitch axis (y_r). The cumulative rotation matrix is given by

$$R_r = R_b R_{\alpha r} R_{\beta r}. \tag{7.10}$$

The right wing velocity Jacobian is given by

$$J_{v,r} = \begin{pmatrix} | & | & | & & | & & | & & | & & | & & | & | \\ \mathbf{e}_1 & \mathbf{e}_2 & \mathbf{e}_3 & R_\psi R_\theta S_{e_1} \mathbf{d}_{rb} & R_\psi S_{e_2} \mathbf{d}_{rb} & S_{e_3} \mathbf{d}_{rb}, & R_b S_{e_3} \mathbf{d}_{rw} & R_b R_{\alpha r} S_{e_2} \mathbf{d}_{rw} & \mathbf{0} & \mathbf{0} & & & & \\ | & | & | & & | & & | & & | & & | & & | & | \end{pmatrix}. \quad (7.11)$$

The right wing angular velocity Jacobian is given by

$$J_{w,r} = \begin{pmatrix} | & | & | & & | & & | & & | & & | & & | & | \\ \mathbf{0} & \mathbf{0} & \mathbf{0} & R_\psi R_\theta \mathbf{e}_1 & R_\psi \mathbf{e}_2 & \mathbf{e}_3 & R_b \mathbf{e}_3 & R_b R_{\alpha r} \mathbf{e}_2 & \mathbf{0} & \mathbf{0} & & & & \\ | & | & | & & | & & | & & | & & | & & | & | \end{pmatrix}. \quad (7.12)$$

7.2.2.4 Jacobian matrices of the left wing

Figure 7.1a also shows the coordinate definition of the left wing with respect to the body frame. The left wing rotates with respect to the stroke axis (z_l) and then the pitch axis (y_l). The cumulative rotation matrix is given by:

$$R_l = R_b R_f R_{\alpha l} R_{\beta l}. \quad (7.13)$$

The left wing velocity Jacobian is given by

$$J_{v,l} = \begin{pmatrix} | & | & | & & | & & | & & | & & | & & | & | \\ \mathbf{e}_1 & \mathbf{e}_2 & \mathbf{e}_3 & R_\psi R_\theta S_{e_1} \mathbf{d}_{lb} & R_\psi S_{e_2} \mathbf{d}_{lb} & S_{e_3} \mathbf{d}_{lb} & \mathbf{0} & \mathbf{0} & R_b R_{cf} S_{e_3} \mathbf{d}_{lw} & R_b R_{cf} R_{\alpha l} S_{e_2} \mathbf{d}_{lw} & & & & \\ | & | & | & & | & & | & & | & & | & & | & | \end{pmatrix}. \quad (7.14)$$

The left wing angular velocity Jacobian is given by

$$J_{w,l} = \begin{pmatrix} | & | & | & & | & & | & | & | & & | & & | \\ \mathbf{0} & \mathbf{0} & \mathbf{0} & R_\psi R_\theta \mathbf{e}_1 & R_\psi \mathbf{e}_2 & \mathbf{e}_3 & \mathbf{0} & \mathbf{0} & R_b R_{cf} \mathbf{e}_3 & R_b R_{cf} R_{\alpha l} \mathbf{e}_2 & & & \\ | & | & | & & | & & | & | & | & & | & & | \end{pmatrix}. \quad (7.15)$$

7.2.3 A time-varying aerodynamic model

In the previous chapter, we investigated the dynamics of a single flapping wing in water. Generalizing the numerical solver to the entire robot is prohibitively expensive. Here we generalize a previous quasi-steady blade element model [96] to account for body movement and rotation. We aim to quantify the influence of robot morphological and kinematic parameters on swimming stability and speed.

In equation (7.2) the generalized force $\boldsymbol{\tau}$ relates to net external force, which consists of aerodynamic forces, flexure viscoelastic forces, and actuator driving forces:

$$\mathbf{F}_{ext} = \mathbf{F}_{aero} + \mathbf{F}_{flexure} + \mathbf{F}_{act}. \quad (7.16)$$

The aerodynamic force consists of contributions from the robot body, and left and right wings. We describe the modeling of these external forces in the following sections.

7.2.3.1 Aerodynamic model of the robot body

Figure 7.2a illustrates the robot body and wing centers of mass, and the corresponding aerodynamic forces. First, we consider the drag force on the robot body.

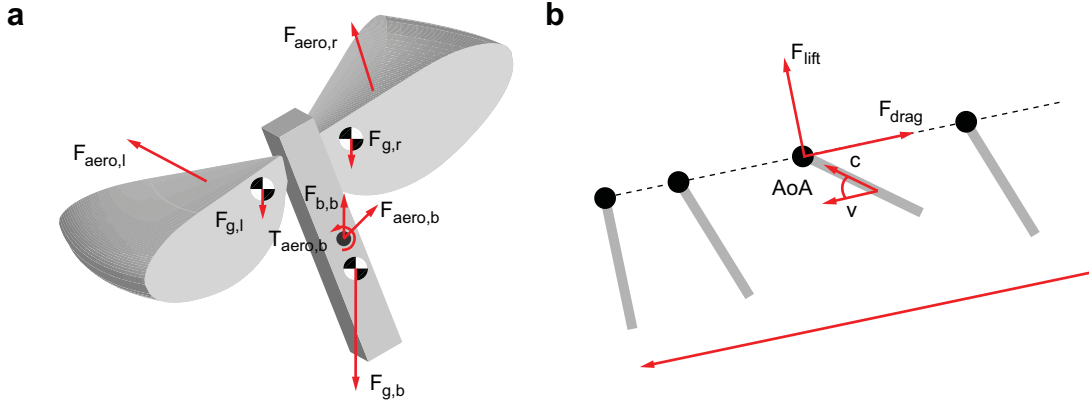


Figure 7.2: Aerodynamic model of the robot. (a) Illustration of aerodynamic forces and torques. (b) Definition of the instantaneous lift and drag directions. The robot body oscillation tilts the stroke plane, which changes the angle of attack, and the lift and drag direction.

Since the body center of mass does not coincide with its geometric center, we separately model the damping force and torque with respect to its center of mass.

The force on the robot body is predominately contributed by pressure because the corresponding Reynolds number is approximately 100. The drag force has quadratic dependence on body velocity:

$$\mathbf{F}_d = -\frac{1}{2}\rho C_d S_{\perp} \|\mathbf{v}_b\| \mathbf{v}_b, \quad (7.17)$$

where \mathbf{v}_b is the instantaneous body velocity and S_{\perp} is the frontal area normal to \mathbf{v}_b .

The damping torque with respect to the body center of mass is given by

$$\mathbf{\Gamma}_d = -\frac{1}{2}C_{\Gamma} \rho r S_W^2 \|\boldsymbol{\omega}\| \boldsymbol{\omega}, \quad (7.18)$$

where $\boldsymbol{\omega}$ is the instantaneous angular velocity, S_W is the total wetted area, and r is the mean moment arm. C_d and C_{Γ} are the body drag and torque coefficients.

Since water density is approximately 900 times that of air, it is important to consider buoyancy and added mass effects for aquatic locomotion. Buoyancy accounts for nearly 25% of the robot weight. Here the buoyancy force is given by:

$$\mathbf{F}_{b,b} = \rho g V_{disp} \hat{\mathbf{z}}, \quad (7.19)$$

where V_{disp} is the volume displaced by the robot body.

Added mass effects arise because a moving robot body accelerates the nearby fluid. Specifically, this term depends on body surface area and fluid density. With respect to the inertial frame, we model added mass contribution as

$$M_{add} = \begin{pmatrix} \rho l S_x & 0 & 0 \\ 0 & \rho l S_y & 0 \\ 0 & 0 & \rho l S_z \end{pmatrix}, \quad (7.20)$$

where S_x , S_y , and S_z are the corresponding frontal areas, ρ is the fluid density and l is a length scale. l is a fitting parameter and we set it to be the robot width.

7.2.3.2 Blade element quasi-steady method

We adopt the classical quasi-steady blade element method and account for wing root movement from body motions. Following the blade element approach, we divide each wing into N chordwise panels and approximate each panel as translating on a 2D plane. Figure 7.2b illustrates the translating and pitching motion of a chordwise panel. The instantaneous stroke plane is not orthogonal to the \mathbf{z} axis due to robot oscillation.

First, we calculate each panel's instantaneous leading edge velocity using the wing velocity Jacobian:

$$\mathbf{v}_{le} = J_v \dot{\mathbf{q}}, \quad (7.21)$$

where \mathbf{v}_{le} denotes the leading edge velocity. Next, we compute the normalized wing chord vector $\hat{\mathbf{c}}$ using rotation matrices derived from the previous chapter. The panel angle of attack is given by

$$AoA = \cos^{-1}(\hat{\mathbf{c}} \cdot \hat{\mathbf{v}}_{\perp}), \quad (7.22)$$

where $\hat{\mathbf{v}}_{\perp}$ is the normalized component of \mathbf{v}_{le} orthogonal to the wing span. Given the local angle of attack, we compute local lift and drag coefficient following Dickinson's formula [24]:

$$\begin{aligned} C_L &= C_{L0} \sin 2AoA \\ C_D &= \frac{C_{D0} + C_{Dmax}}{2} - \frac{C_{Dmax} - C_{D0}}{2} \cos 2AoA \end{aligned}, \quad (7.23)$$

where the coefficients are given by $C_{L0} = 1.8$, $C_{D0} = 0.4$, and $C_{Dmax} = 3.4$. Then we compute the direction of the lift and drag forces on the local panel:

$$\begin{aligned} \hat{\mathbf{f}}_L &= \hat{\mathbf{w}}_{z,b} \\ \hat{\mathbf{f}}_D &= -\hat{\mathbf{v}}_{\perp} \end{aligned}. \quad (7.24)$$

Here $\hat{\mathbf{w}}_{z,b}$ is the unit normal vector of the instantaneous stroke plane. These definitions are adopted from the aeromechanical model developed by Whitney et al [96]. Finally, we compute the total lift and drag forces on the wing by summing the contribution

from each panel:

$$\begin{aligned}\mathbf{F}_L &= \frac{1}{2}\rho \sum_{i=1}^N C_{Lv_\perp}^2 c(r_i) \hat{\mathbf{f}}_L \delta r \\ \mathbf{F}_D &= \frac{1}{2}\rho \sum_{i=1}^N C_{Dv_\perp}^2 c(r_i) \hat{\mathbf{f}}_D \delta r\end{aligned}\quad (7.25)$$

Here $c(r_i)$ represents the local chord length of the i^{th} panel. The aerodynamic force contribution from the left and the right wing can be separately computed through invoking equation (7.25). We do not include contribution from rotational circulation and added mass because their force coefficients are not quantified in previous studies. Inclusion of these terms may lead to unnecessary over-fitting.

The aerodynamic lift and drag forces, together with other external forces, need to be projected onto the generalized coordinates to obtain the generalized forces. The j^{th} component of the generalized force $\boldsymbol{\tau}$ can be calculated as:

$$\tau_j = \sum_k \mathbf{f}_{ext,k} \cdot \frac{\partial \mathbf{x}_k}{\partial q_j}, \quad (7.26)$$

where \mathbf{x}_k is the center of pressure location of the k^{th} panel, and $\mathbf{f}_{ext,k}$ is the total external force on the k^{th} panel. To evaluate this equation, we need to estimate the center of pressure for each wing panel and integrate across the wing span. The center of pressure location can be computed given the local wing chord and a non-dimensionalized center of pressure r_{cop} . The relationship between r_{cop} and angle of attack is given in a previous study [12]:

$$r_{cop} = 0.25 + 0.25 \times \frac{1}{1 + \exp(\gamma(1 - \frac{4}{\pi}AoA))}. \quad (7.27)$$

Here γ is a positive fitting parameter related to the wing geometry.

While the generalized force vector can be computed easily through equation (7.26), it does not offer a straightforward physical interpretation. The torque on the robot center of mass due to the fluid forces on the wing is given by:

$$\mathbf{\Gamma} = \frac{1}{2}\rho \sum_{i=1}^N \mathbf{r}_{p,i} \times \left(C_L \hat{\mathbf{f}}_L + C_D \hat{\mathbf{f}}_D \right) \|v_{\perp}\|^2 c(r_i) \delta r, \quad (7.28)$$

where $\mathbf{r}_{p,i}$ is the displacement from robot center of mass to the local center of pressure.

7.2.4 Contribution from wing flexures and actuators

We model the wing flexure as a torsional spring with viscous damping. The torques exerted by the wing hinges along wing pitch axes are given by:

$$\begin{aligned} \tau_{\beta r} &= -K_h \beta_r - D_h \dot{\beta}_r \\ \tau_{\beta l} &= -K_h \beta_l - D_h \dot{\beta}_l \end{aligned}, \quad (7.29)$$

where K_h is the stiffness and D_h is the viscoelastic damping. Both parameters are dependent on the wing hinge geometry.

The piezoelectric actuator and robot transmission can be modeled as a sinusoidal torque source [49]. The driving frequency and torque amplitude depend on the input electrical signal. The input torque along the wing stroke axes are given by:

$$\begin{aligned} \tau_{\alpha r,act} &= A_r \cos(2\pi ft) \\ \tau_{\alpha l,act} &= A_l \cos(2\pi ft) \end{aligned}. \quad (7.30)$$

The robot transmission also exerts restoring and damping torque along the stroke

axes:

$$\begin{aligned}\tau_{\alpha r,trans} &= -K_t \alpha_r - D_t \dot{\alpha}_r \\ \tau_{\alpha l,trans} &= -K_t \alpha_l - D_t \dot{\alpha}_l\end{aligned}, \tag{7.31}$$

where K_t and D_t are robot transmission stiffness and viscoelastic damping coefficients.

7.3 Simulation results

We solve the equations of motion numerically to investigate the robot aquatic locomotion. Table 7.3 lists the robot parameters. In the simulations, we vary the actuator driving torque amplitude and the flapping frequency. We solve for the swimming trajectory and analyze the corresponding dynamical data. In the following sections, we give detailed discussion about the simulation results.

7.3.1 Symmetric flapping

First, we simulate the robot operated at 11 Hz and set the input torque amplitude to 15 $\mu\text{N m}$. The simulation runs for 8 flapping periods. Figure 7.3 details the robot kinematics. Figure 7.3a shows the trajectory and velocity of the body center of mass. The color scale represents ascending speed. The robot swims faster during the wing midstroke and slows down during the stroke reversal. This trajectory is also projected onto the xy , xz and yz plane for clarity. Figure 7.3b shows the displacement of the body center of mass as a function of time, which indicates that the robot ascends 40 mm in 0.73 seconds. The body oscillation amplitude in the x-axis is 0.5 mm. There is no body oscillation in the y-axis due to symmetry. Figure 7.3c shows the body center of mass velocity as a function of time. The body ascending speed is

Robot Body Properties		
Body mass	80	mg
Roll axis inertia	1.42	$\text{g}\cdot\text{mm}^2$
Pitch axis inertia	1.34	$\text{g}\cdot\text{mm}^2$
Yaw axis inertia	0.45	$\text{g}\cdot\text{mm}^2$
Body width	4	mm
Body height	14	mm
Wing Properties		
Wing mass	1	mg
Wing span	14	mm
Wing area	54	mm^2
Wing spanwise c.o.m	3.19	mm
Wing chordwise c.o.m	0.73	mm
Roll axis inertia	77	$\text{mg}\cdot\text{mm}^2$
Pitch axis inertia	8.5	$\text{mg}\cdot\text{mm}^2$
Yaw axis inertia	69	$\text{mg}\cdot\text{mm}^2$
Transmission Properties		
Transmission stiffness	6	$\mu\text{N}\cdot\text{m}/\text{rad}$
Wing hinge stiffness	2	$\mu\text{N}\cdot\text{m}/\text{rad}$
Wing hinge damping	5	$\text{nN}\cdot\text{m}\cdot\text{s}/\text{rad}$
Wing hinge length	2	mm
Input commands		
Stroke torque amplitude	15	$\mu\text{N}\cdot\text{m}$
Frequency range	1-30	Hz

Table 7.1: Physical parameters of the robot body, wings, transmission, and input commands.

sinusoidal with mean of 80 mm/s and amplitude of 15 mm/s. Figure 7.3d, e show the body orientation and its angular velocity. While there is no body roll and yaw due to symmetric flapping kinematics, the body pitching motion is sinusoidal with an amplitude of 9.3° . Figure 7.3f, g show the flapping kinematics of the left and right wings are identical. Both stroke and pitch motion are approximately sinusoidal. The stroke and pitch amplitudes are 23.8° and 25.4° , respectively. The relative phase shift between wing stroke and pitch is -2.7° .

7.3.2 Asymmetric flapping

While we can prescribe symmetric flapping kinematics in dynamical simulations, there exists intrinsic asymmetry in experiments. Flapping asymmetry is usually contributed by manufacturing or assembly imprecision. Here we investigate the robot stability when the flapping motion is slightly mismatched. Figure 7.4 shows a simulation in which the left wing input torque is increased by 5%. All other simulation parameters are identical to the previous case described in section 7.3.1. Figure 7.4a shows that there is a lateral drift along the \hat{y} axis. Figure 7.4b, c show the mean drift speed is non-zero. Figure 7.4d, e show the robot angular motion. While the body pitch amplitude is approximately the same to that of symmetric flapping, we observe small body yaw and roll. In fact, the robot body precesses about the positive \hat{z} axis. The precession amplitude increases as flapping asymmetry grows or flapping frequency reduces. Figure 7.4f, g show the wing kinematics. The left wing stroke and pitch amplitude are 9% and 11% larger than that of the right wing, respectively. When driven at 11 Hz, the robot is passively upright stable even if there is a small

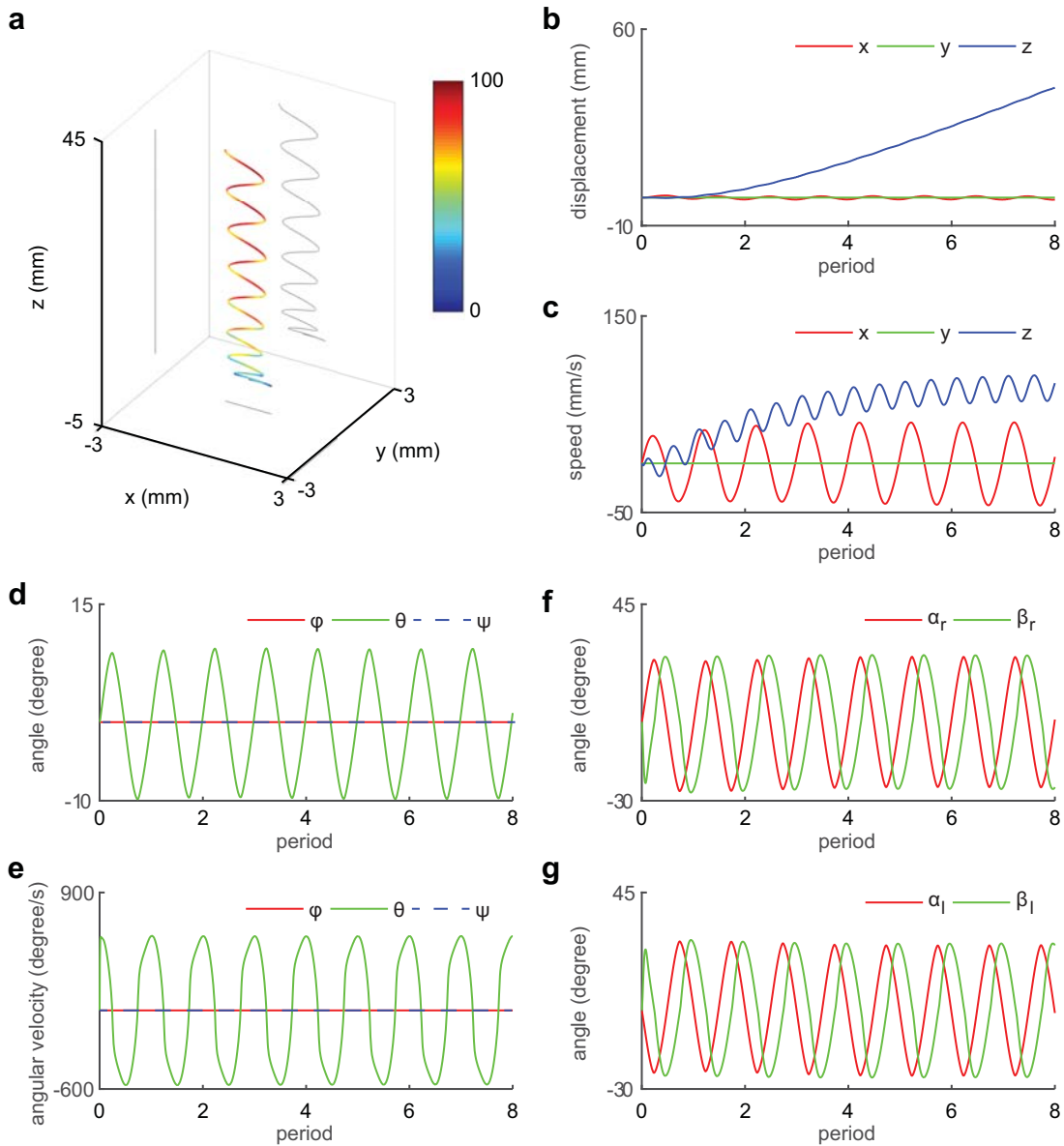


Figure 7.3: Simulation of the robot operated at 11 Hz. Both wings share the same driving inputs. (a) The motion of the robot center of mass. The color scale represents vehicle speed with the unit of mm/s. (b) The robot center of mass displacement. (c) The robot center of mass velocity. (d) The robot body rotation. (e) The robot body angular velocity. (f) The stroke and pitch motion of the right wing. (g) The stroke and pitch motion of the left wing.

flapping asymmetry.

7.3.3 Body-wing coupling

While the previous simulations show noticeable body-wing coupling, they do not quantify the influence on force generation. Figure 7.5 illustrates the body pitching and the body translation. Figure 7.5a shows that the body pitching opposes the wing stroke direction. The blue lines illustrate the instantaneous wing tip velocity, the body velocity and the body pitching. The red line shows the tilting of the wing stroke plane. This body rotation reduces wing lift and creates a downward pointing drag component. Consequently, body pitching adversely affects robot ascent. Figure 7.5b illustrates the influence of body translation on the lift force production. The drag force accelerates the robot body in the opposite direction relative to wing stroke. This causes back flow near wing root and reduces lift. In the quasi-steady model, the local angle of attack near the wing root becomes negative. Both of these effects are negligible for hovering flight in air, but they become significant for aquatic locomotion when the flapping frequency is reduced. Given the robot mass and geometry, we find that the body pitching is more important than the body translation. Here we investigate the body pitching effect by varying the robot's body moment of inertia while holding other parameters constant.

Figure 7.6a illustrates the right wing tip trajectory of the robot when driven at 11 Hz. In this plot, we remove the body translation to overlay the trajectories of all eight flapping periods. The color scale represents the instantaneous wing tip speed. This trajectory is projected onto the xy , xz , and yz plane for clarity. Figure 7.6b shows a

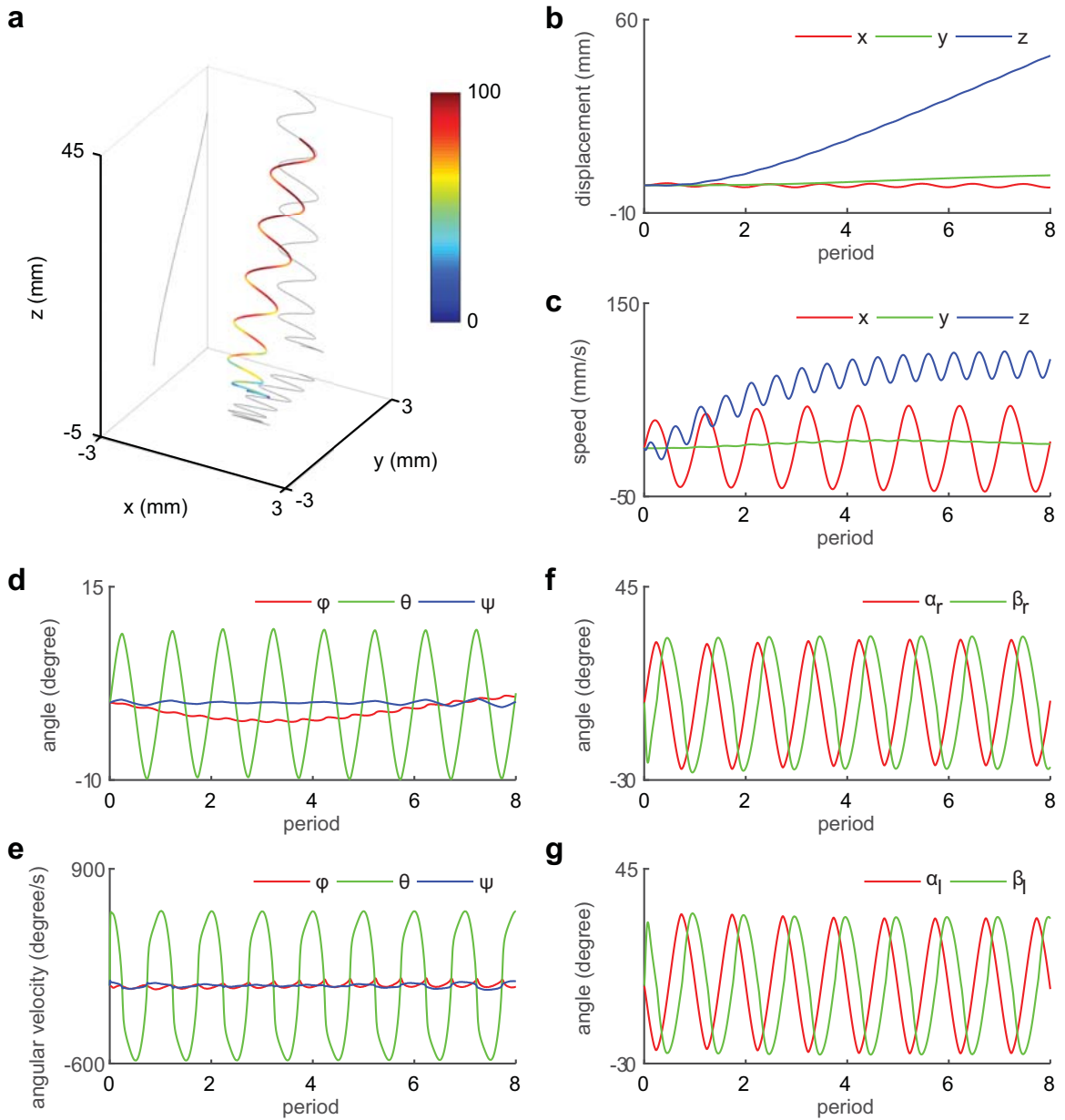


Figure 7.4: Simulation of the robot operated at 11Hz. The driving torque amplitude of the left wing is 5% larger than that of the right wing. (a) The motion of the robot center of mass. The color scale represents the vehicle speed with the unit of mm/s. (b) The robot center of mass displacement. (c) The robot center of mass velocity. (d) The robot body rotation. (e) The robot body angular velocity. (f) The stroke and pitch motion of the right wing. (g) The stroke and pitch motion of the left wing.

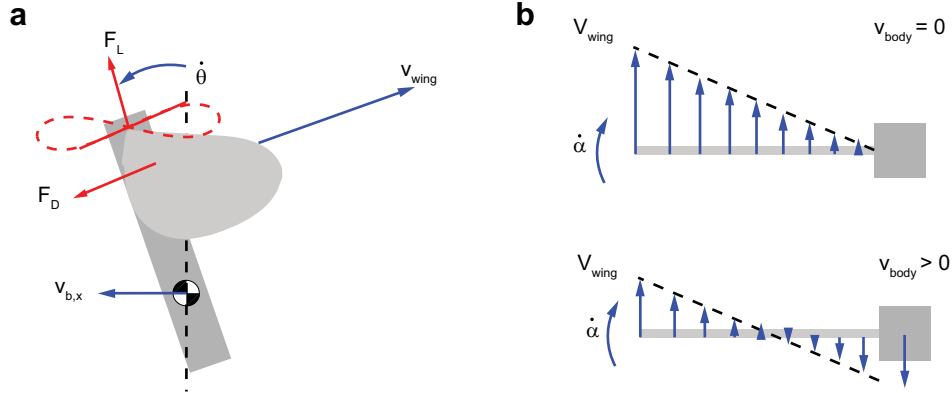


Figure 7.5: Effect of the body-wing coupling. (a) Side view of the body-wing coupling. Body pitching and lateral motion reduce the wing stroke amplitude by tilting the stroke plane. (b) Top view of the body-wing coupling. Body translation opposes the wing stroke motion and causes back flow near the wing root.

similar simulation in which we increase of body moment of inertia by a million times. Consequently, the robot experiences negligible body oscillation due to this dramatic increase of rotational inertia. Compared to figure 7.6a, the oscillation of the wing tip trajectory along the \hat{z} axis is reduced. The tilting of the wing stroke plane has a large effect on the ascending speed and the lift force generation. Figure 7.6c shows the ascending speed increases from 75 mm/s to 195 mm/s when body pitching is removed. Figure 7.6d shows the lift force from the right wing increases from 350 μN to 550 μN . This result shows that the body pitching reduces the lift force by 60%.

7.3.4 Frequency variation

In Chapter 3, we gave a scaling relationship that relates the robot flapping frequency to the wing size. In Chapter 6, we further derived an equation that relates aerial and aquatic flapping frequency. Previous studies [65] on aerial locomotion simply choose an arbitrary wing size and operating frequency. Since we aim to enable

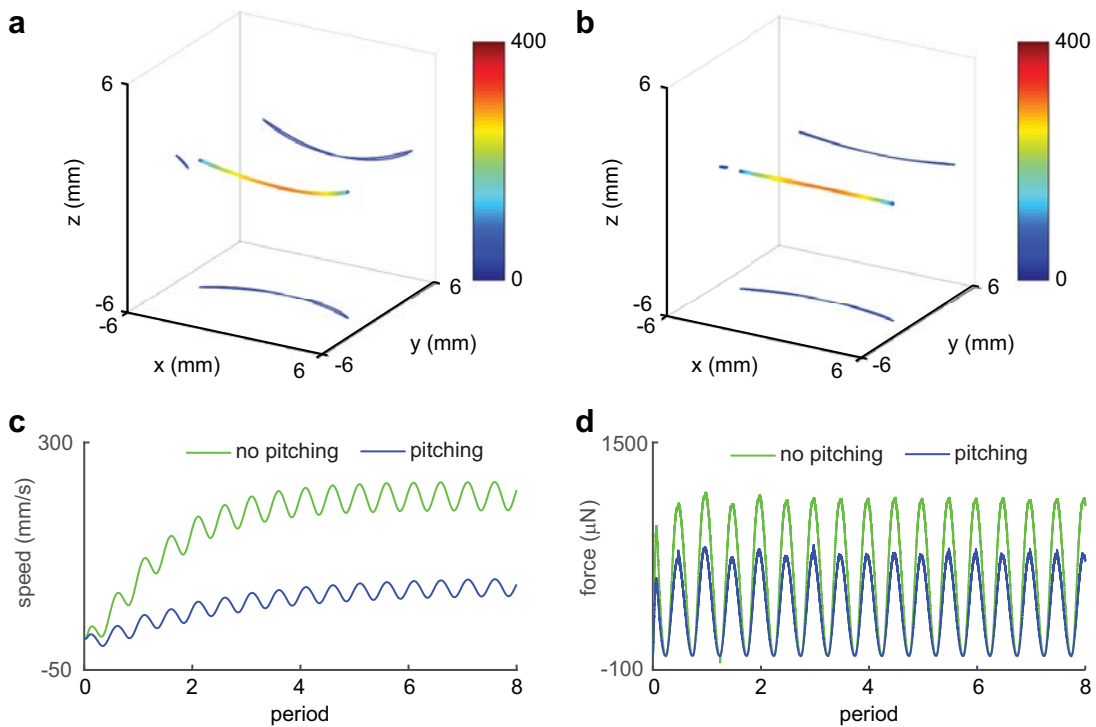


Figure 7.6: Effect of body pitching on lift force. (a) The wing tip trajectory of the robot operated at 11Hz. (b) The wing tip trajectory of the robot without experiencing body oscillation. The color bars in (a) and (b) represent wing tip speed with the unit of mm/s. (c) Comparison of the ascending speed with or without body pitching. (d) Comparison of the lift force with or without body pitching.

aerial and aquatic locomotion, we must consider passive upright stability as an additional constraint. Here we investigate the robot stability in water under different driving frequencies.

Figure 7.7 shows the wing kinematics, robot pitching and ascending speed as functions of frequency given constant driving torque amplitude. The blue and red colored regions distinguish the unstable and stable frequencies, respectively. In our model, the Euler angle definition becomes singular when body rotation exceeds 90° . The numerical solver terminates prematurely at low frequencies due to the large body oscillation.

Figure 7.7a illustrates the wing stroke and the pitch amplitudes. The red line shows the wing stroke amplitude reduces as frequency increases. This relationship can be well approximated by the black curve that is given by $f \cdot \alpha = C$, where C is a constant. Here, the constant is related to the maximum wing stroke velocity, which implies that the fluid drag remains nearly constant as the driving frequency changes. The green curve shows that the pitching amplitude remains constant as the frequency varies. The blue curve shows that the phase shift δ increases as the driving frequency increases.

Figure 7.7b shows that the body pitch amplitude and the ascending speed reduce monotonically as the frequency increases. This result leads to a seeming paradox between the body pitching and the lift force generation. While we have shown body pitching reduces the lift force production, it is counter-intuitive that the reduction of the body pitching relates to a decrease of ascending speed. This observation can be explained by considering the phase shift parameter δ in figure 7.7a. In Chapter 4,

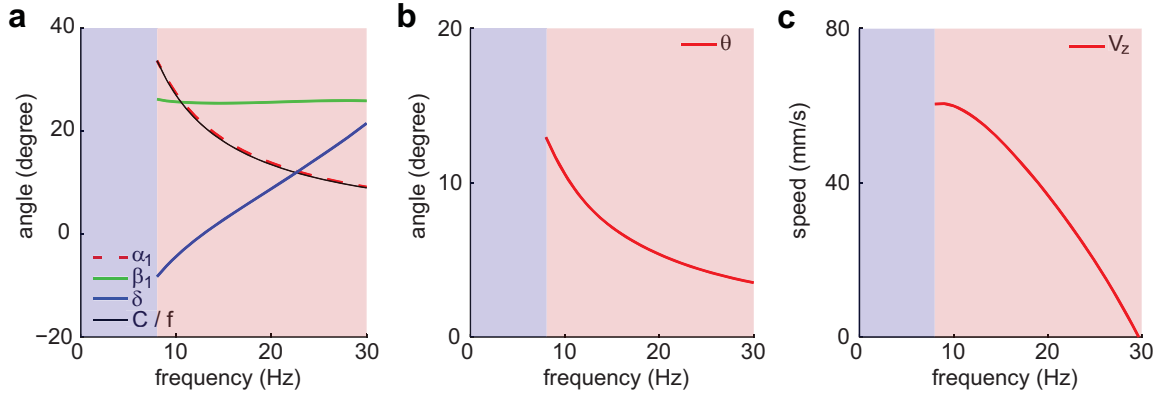


Figure 7.7: Influence of the flapping frequency on aquatic locomotion. (a) The wing stroke and pitch amplitude as a function of the flapping frequency. (b) The body pitch amplitude as a function of the flapping frequency. (c) The robot ascending speed as a function of the flapping frequency.

we showed δ negatively correlates with lift force generation. Here δ increase from -8° to 22° as frequency increases from 9 Hz to 30 Hz. The increase of δ dominates the reduction of body pitching at high frequency.

There are two competing effects that influence the robot locomotion. At low flapping frequencies, large body rotations destabilize the vehicle and reduce lift. At high frequencies, the phase shift δ increases and adversely impacts lift. While we can mitigate the influence of δ by stiffening wing hinge, this change inevitably impacts aerial hovering conditions. Our simulation shows that the robot needs to operate in the range between 10-15 Hz in water. In the next section, we verify our simulation results by conducting robot swimming experiments.

7.4 Experimental result

7.4.1 Experimental setup

A robot is placed in the center of a beaker filled with tap water. The beaker radius and height are both 10 cm. A Phantom 7.10 colored high speed camera captures the swimming motion at 200 frames per second. The robot driving frequency varies from 5 Hz to 15 Hz and the input voltage amplitude is fixed at 200 V. The Vicon motion tracking system does not operate in water because infrared radiation is scattered. Hence, all swimming experiments are conducted without feedback control.

7.4.2 Robot kinematic tracking

The recorded swimming videos show noticeable body pitching during robot locomotion. We quantify the amplitude of body pitching through post-processing the videos. We manually select two images of maximum body pitch in opposite directions. A number of tracking points are manually labeled given the recorded images. These are the 2D projection of specific reference points onto the camera image plane. Since there is an accurate geometrical model of the RoboBee, we can estimate robot orientation by solving a constrained optimization problem. Specifically, the problem can be formulated as:

$$\arg \min_{\phi, \theta, \psi} \sum_i \|R_{(1:2,:)}(\phi, \theta, \psi)s_i - r_i\|_2, \quad (7.32)$$

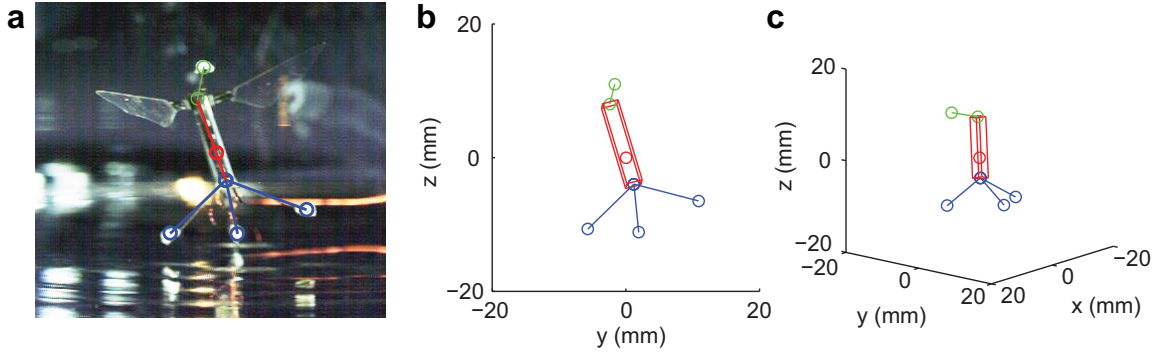


Figure 7.8: Orientation tracking of the robot. (a) Raw image and manual tracking of the robot centroid and labeling markers. (b) Fit of the robot model and its projection onto the camera image plane. (c) Fit of the robot model shown in perspective view.

where $R_{(1:2,:)} \in R^{2 \times 3}$ is the top two rows of the rotation matrix:

$$R = R_{z,\phi} R_{y,\theta} R_{x,\psi}. \quad (7.33)$$

$s_i \in R^3$ is the displacement of the i th reference point with respect to the robot center of mass, and $r_i \in R^2$ is the corresponding measured location on the image. Here the measured location r_i can be calculated from the pixel values through subtracting the centroid pixel values and then scaling by the appropriate length scale. This simple operation is given by

$$r_i = \alpha(p_i - c). \quad (7.34)$$

The robot centroid is identified manually and the scaling constant is obtained by measuring the aquarium dimension from the image.

Equation (7.32) can be solved using Matlab's constrained optimization function *fmincon*. We impose constraints on the rotation angles such that $-\pi \leq \phi, \theta, \psi \leq \pi$. Figure 7.8a labels the robot center of mass and several tracking points. Figure 7.8b

shows the numerical solution of the robot model projected onto the image plane. Figure 7.8c shows the same solution in perspective view.

7.4.3 Model comparison

We conduct robot swimming experiments at 5, 7, 8, 9, 11, 13 and 15 Hz. We observe the robot is unstable at low driving frequencies due to large body oscillation. Figure 7.9a shows an overlaid image of the robot swimming at 5 Hz. The robot plummets immediately after takeoff and suffers large body pitch oscillation (figure 7.9b). In contrast, the robot becomes upright stable when it is driven at 11 Hz. Figure 7.9c shows the same robot ascending to the water surface. The red lines in figure 7.9b, d show that the robot pitch amplitude reduces from 14.8° to 9.4° .

Figure 7.9e illustrates the trajectories of the robot operated at different frequencies. The robot is able to take off and lift up for frequencies larger than 5 Hz. However, at 7 and 8 Hz the robot swims laterally and is unable to reach the water surface. As we continue to increase the driving frequency, robot stability improves and the robot is able to swim to the water surface. However, the robot performance deteriorates as driving frequency continues to increase beyond 11 Hz. The wing stroke amplitude reduces significantly as the flapping frequency increases beyond 13Hz. At 15 Hz the robot loses lift near the water surface and plunges downward. We observe a crack on the piezoelectric actuator that powers the left wing. At high driving frequencies the phase shift between the actuator tip and the wing root increases dramatically, which leads to higher stress on the piezoelectric actuator. Consequently, we are unable to drive the robot beyond 15 Hz.

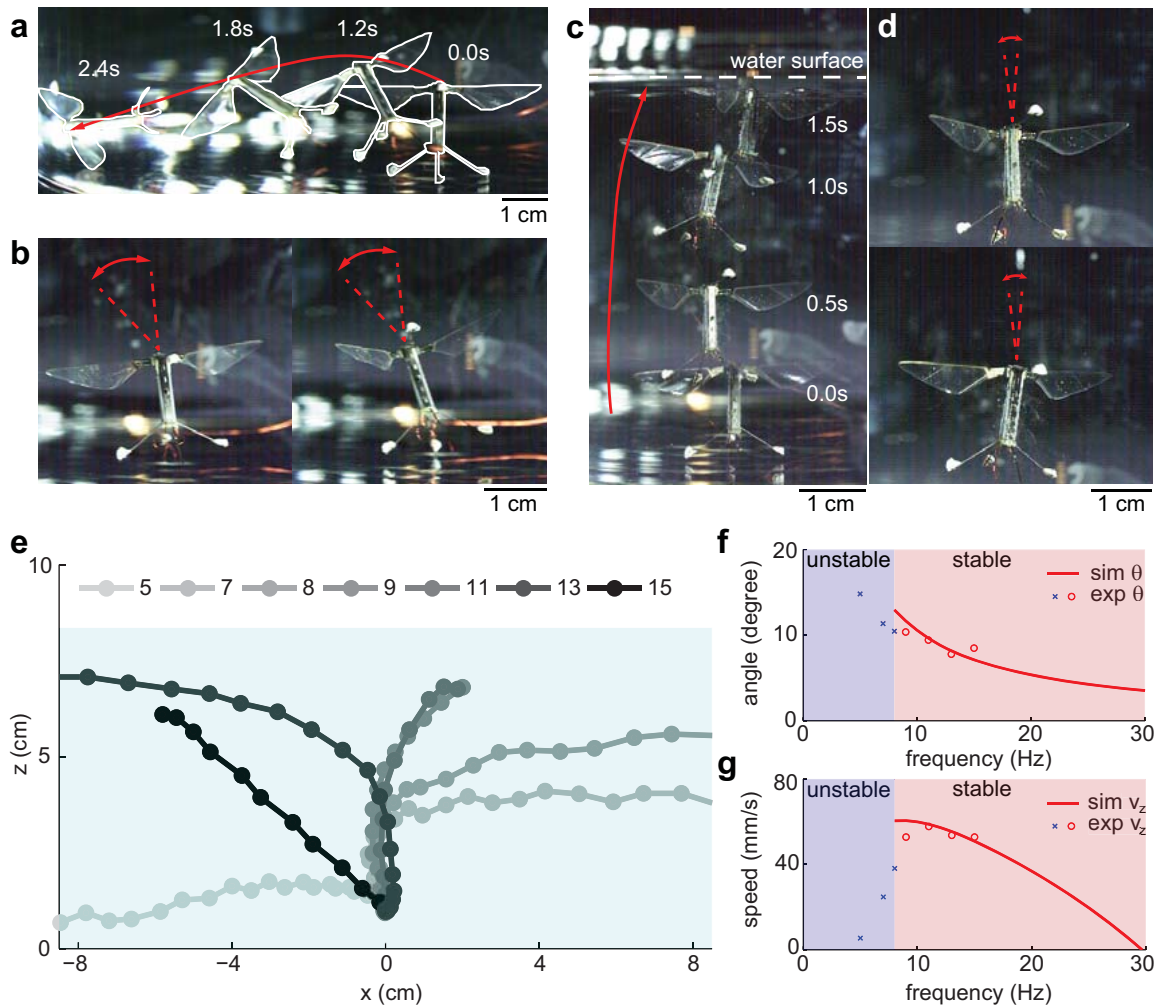


Figure 7.9: Robot body pitching and swimming stability. (a) Overlaid image of an unstable swimming robot when driven at 5Hz. (b) The robot experiences large body pitching when driven at 5Hz. (c) Overlaid image of a robot ascending to the water surface when driven at 11Hz. (d) When driven at 11Hz, the robot body pitching amplitude reduces. (e) Comparison of the robot swimming trajectories when flapping at different frequencies. (f) The robot ascending speed as a function of the flapping frequency. (d) The robot body pitch amplitude as a function of the flapping frequency. (f) and (g) show dynamical simulations agree well with the experiments.

Figure 7.9f, g further compare the simulated ascending speed and the body pitch to that of the experiments. We find our simulation results closely agree with the experimental measurements in the frequency range of 9-15 Hz. While our simulations diverge at low flapping frequencies due to kinematic singularities, our experiments show the robot is unstable when operated below 8 Hz. We cannot verify our model beyond 15 Hz because the robot actuator fails at high frequencies.

Our simulations and experiments offer important implications for hybrid aerial-aquatic locomotion. First, both simulations and experiments show the robot is unstable when driven below 8 Hz. In addition, they both show stable swimming in the range of 9-15 Hz. Based on the aerial, aquatic scaling relation from Chapter 6, we estimate the corresponding aerial flapping frequency to be 270-400 Hz. Based on the wing size and frequency scaling relation from Chapter 3, we predict that the wing area needs to be reduced by 30%-50%. In addition, our simulation suggests that an increase of robot moment of inertia improves swimming stability. In the next chapter, we apply these results to developing a fully functional, hybrid aerial-aquatic robot.

Chapter 8

A flapping wing, hybrid aerial-aquatic microrobot

8.1 Introduction

Hybrid aerial-aquatic robots capable of traversing complex multi-phase environments will have a wide range of applications, such as environmental exploration and search and rescue missions [70]. Owing to smaller size and weight, microrobots are advantageous for navigating within confined and cluttered environments. Since inertial forces diminish at the millimeter scale, microrobots are more resilient to impact events such as crash landing on the water surface or collision with obstacles [50]. Despite these functional advantages, hybrid aerial-aquatic microrobots face unique design and fabrication challenges. While previous studies have developed numerous robotic platforms [30, 68, 81] and propulsive strategies [52, 67] to address the challenges of air-water locomotion and transition, these designs are unsuitable for

microrobots due to their limited payload, fabrication difficulties, and the dominance of surface forces near or below the millimeter scale.

A hybrid aerial-aquatic microrobot must solve two key problems: 1) multi-phase propulsion for air and water, 2) overcoming surface tension for water exit and entry. The large density difference between air and water imposes conflicting criteria for robot locomotion and structural design in these two environments. Flight in air requires high-frequency flapping which imparts very small body perturbations while aquatic locomotion requires low-frequency flapping that can induce large perturbations. Water surface tension far exceeds the robot weight and thus transitioning into or out of water requires novel mechanisms to overcome this effect. However, any additional mechanisms must satisfy the microrobot's sub-gram payload limits. This design challenge requires fabrication of lightweight, energy-efficient, and multi-functional components for locomotion and water-air transition. In this chapter, we report an impulsive water-air transition method and novel micro-mechanical device fabrication that culminate in the first bio-inspired, flapping wing, hybrid aerial-aquatic microrobot.

Our robot can demonstrate aerial hovering, air-water transition, swimming, water surface takeoff, and landing (figure 8.1a). The robot flaps at 265 Hz in air and is intrinsically unstable without feedback. We use a motion tracking system [65] with adaptive control [15] to obtain stable hovering flight capabilities (figure 8.1b). The control signals are computed offboard and sent to the robot through a wire tether. To initiate a dive when above water, the wing flapping is halted mid-hover. The robot descends onto the water surface, breaking surface tension upon impact and

subsequently sinks into the aquatic environment (figure 8.1c). To hold position or maneuver once underwater, the robot flaps its wings at 9 Hz. When the robot is to transition back to flying, it first swims upward towards the surface (figure 8.1d). Upon reaching the water surface, a pair of electrolytic plates in the robot body begin decomposing water into oxyhydrogen. The gas is collected by a chamber and the increased buoyant force gradually pushes the robot's wings out of water (figure 8.1e). Lastly, to completely break free from the water surface we use an impulsive strategy: a sparker ignites the oxyhydrogen mixture and the robot jumps off the water surface (figure 8.1f). This combustion-based takeoff results in a typical takeoff velocity of 2.5 m/s and a jump height of 37 cm (figure 8.1.1f). The robot assumes a ballistic trajectory in air and lands on the ground approximately 0.55 s after takeoff. We ensure that the robot is still functional after takeoff and landing by demonstrating successful hovering flight with minimal tuning to the robot's structure.

This robot design successfully addresses the two key challenges unique to hybrid, aerial-aquatic microrobots – multi-phase locomotion and water-air transition. In chapter 7, we examine the stability properties of robot aquatic locomotion. In this chapter, we study surface tension effects and investigate robot water-air transition.

8.2 Robot design and fabrication

We modify the robot's structure with a number of micro-mechanical features specifically for water-air transition. Compared to the original robot (figure 8.2a-1), this design is split into two symmetric halves (figure 8.2a-2) leaving a large central volume to accommodate functional components for water surface takeoff. These com-

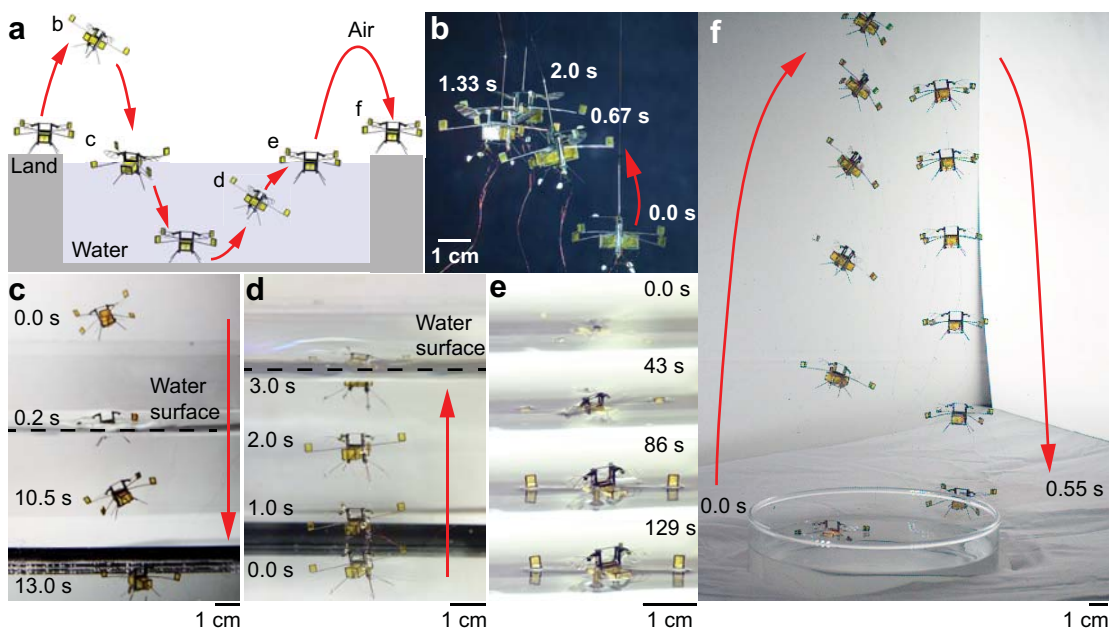


Figure 8.1: Demonstration of aerial-aquatic locomotion and transition. (a) The robot is capable of demonstrating aerial hovering, air-water transition, swimming, water-air transition, impulsive takeoff, and landing. (b) Composite image of a hovering robot. (c) Composite image of the robot transitioning from air to water. (d) Composite image of the robot swimming to the water surface. (e) Images of the robot gradually emerge from the water surface by capturing gas from electrolysis. (f) Composite image of robot takeoff and landing.

ponents consist of four balance beams and small buoyant outriggers (figure 8.2b, c), a gas collection chamber (figure 8.2b, d, e), and a lightweight device (figure 8.23f) that integrates electrolytic plates and a sparker (figure 8.2g). The electrolytic plates and the sparker utilize electrolysis reactions to achieve water surface takeoff:



The interdigitated electrolytic plates (figure 8.2f) decompose water to hydrogen and oxygen and the sparker ignites the gas for takeoff. The sparker electrodes (figure 8.2g) are laser machined to achieve a small separation gap of 20 μm , which ensures the sparking potential to be within the robot's 300 V operating voltage. The entire device is affixed vertically to the bottom of the gas collection chamber (figure 8.2d). The chamber's titanium top plate is patterned with an array of 34 μm radius micro-openings (figure 8.2e). Four titanium T-beams (figure 8.2b) are affixed to the connections struts (figure 8.2c) above the chamber top plate for maintaining robot stability on the water surface. A sealed box attaches to the tip of each balance beam and functions as a buoyant outrigger to increase buoyancy and improve underwater stability. The additional components total 70 mg and satisfy the vehicle's 150 mg payload capability. In the following sections, we describe the design and fabrication of these devices.

8.2.1 Gas collection chamber fabrication

The gas chamber consists of five rectangular, planar laminates. The top piece is made from 50 μm titanium sheet laminated with 12.7 μm polyimide. It is patterned

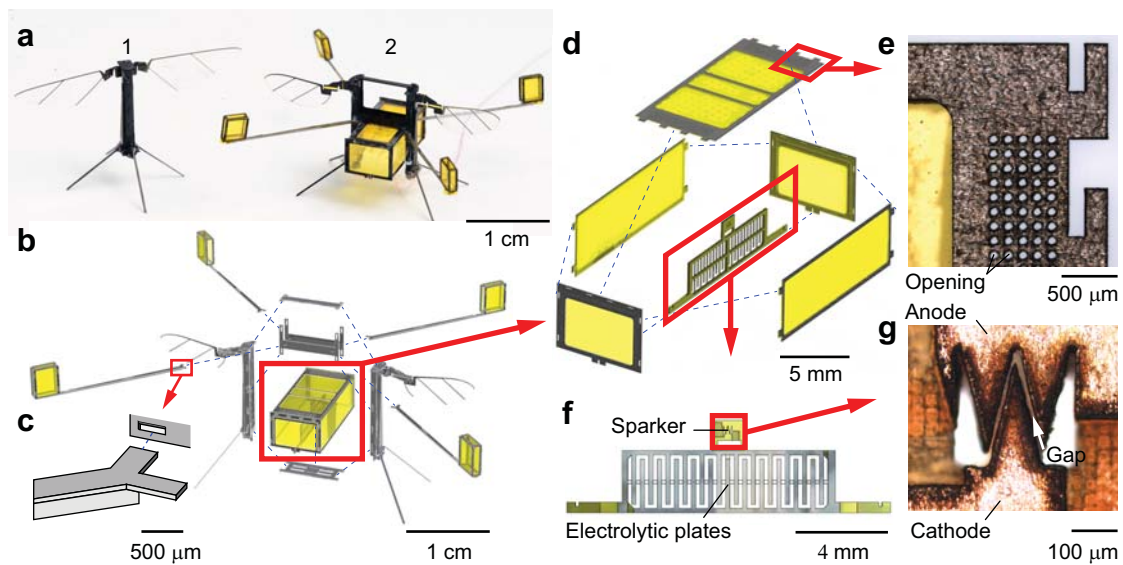


Figure 8.2: Robot components and assembly. (a) An existing 85 mg robot (1) is used to investigate underwater stability. The improved 164 mg robot (2) consists of two symmetric halves, a central gas collection chamber with a sparker plate, four balance beams, and buoyant outriggers. (b) Exploded view of robot assembly. (c) Mating feature of the titanium balance T-beam. (d) Exploded view of gas collection chamber assembly. (e) Microscopic image illustrating an array of porous openings on the chamber's titanium top plate. (f) The sparking plate consists of a pair of stainless steel plates and a copper sparker. (g) Microscopic image of the sparker electrodes.

with a rectangular array (39×12) of circular holes with $34 \mu\text{m}$ radius. The four side pieces are made of $100 \mu\text{m}$ carbon fiber laminated with $12.7 \mu\text{m}$ polyimide. The bottom face is left open for gas collection. The chamber is assembled using tab-and-slot features to ensure precision and strength. The assembled chamber is glued using Loctite 60 minutes epoxy. The chamber weighs 33 mg and has dimension of $14 \text{ mm} \times 6.7 \text{ mm} \times 4.9 \text{ mm}$.

The micro-openings (figure 8.2e) on the robot chamber top plate serve multiple functions. When the robot is dry, air within the chamber exits through the micro-openings, reducing buoyancy, and facilitating the air-water transition. When the robot is wet, a thin film of water covers the micro-openings due to surface tension. The gas collection chamber can then generate and capture gas once fully submerged in water. Upon combustion-based takeoff, these micro-openings enable excess gas pressure to escape, preventing structural damage during detonation.

8.2.2 Balance beam fabrication

Each balance beam consists of two $50 \mu\text{m}$ titanium pieces. These are assembled manually to form a T-beam using tab-and-slot assembly. Each balance beam is 25 mm long, $400 \mu\text{m}$ wide, $400 \mu\text{m}$ tall, and weighs 2 mg.

8.2.3 Buoyant outrigger fabrication

Each buoyant outrigger has dimensions of $2.5 \text{ mm} \times 2.5 \text{ mm} \times 1 \text{ mm}$ and attaches to the tip of the balance beam. The buoyant outrigger consists of three carbon fiber and polyimide laminated pieces: square top and bottom pieces and a foldable side

piece. The foldable side piece is manually folded along compliant flexures. Then top and square pieces are assembled using tab-and-slot features. Finally, the box is sealed using CA glue (Loctite 416).

8.2.4 Sparker plate fabrication

The sparker plate consists of 150 μm copper clad FR-4 (glass reinforced epoxy laminate sheet) and 25 μm stainless steel laminated layers. FR-4 provides structural support, the copper serves as a soldering pad and sparker material, and the stainless steel is used for electrolysis. The sparker plate has three functional parts: a shared ground, a low voltage plate for electrolysis and a high voltage copper plate for generating sparks. Tether wires are soldered on copper pads, which connect to corresponding stainless steel plates via conductive epoxy. The sparker plate weighs 6.5 mg.

8.2.4.1 Material choice of the sparker and electrolytic plates

Copper is a favorable sparker material because of higher thermal conductivity. Figure 8.3a, b compare new stainless steel sparker tips and shorted sparker tips. The stainless steel sparker tips fuse together after three ignitions and we observe noticeable discoloration (figure 8.3b). In contrast, the copper sparker can ignite over 40 times. Oxidation is not an important problem for the sparker because it does not operate when fully submerged in water.

On the other hand, the electrolytic plates are made of stainless steel because copper anodes easily oxidize in water. Figure 8.3c, d compare new copper plates and

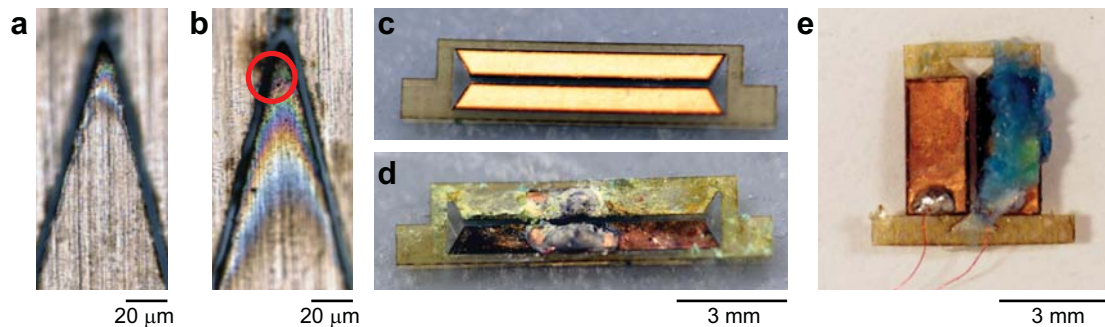


Figure 8.3: Material selection of electrolytic plates and sparker. (a) A new stainless steel sparker tip. (b) A shorted stainless steel sparker tip after three ignitions. The sparker tip changes color due to the heat associated with sparking. The red circle highlights the shorted region. (c) A new pair of copper electrolytic plates. (d) A pair of electrolytic plates after 120 seconds of reaction. Most of the copper on the anode disappears. (e) Copper oxide growth on the anode.

oxidized plates after 120 seconds of use. Figure 8.3e further highlights an oxidized anode. Consequently, we choose stainless steel as the anode material. The stainless steel electrolytic plates can operate for more than 600 seconds without severe oxidization.

8.2.4.2 Electrolytic efficiency

We investigate electrolytic efficiency because the reaction is energetically costly. First, we estimate energy expenditure per takeoff assuming perfect efficiency. The volume of the gas collection chamber is 450 mm^3 , which implies 300 mm^3 hydrogen and 150 mm^3 oxygen are produced. Assuming standard temperature and pressure, we estimate the electrolytic plates need to dissociate 1.3×10^{-5} mole of water. The enthalpy of water electrolysis is 286 kJ/mol , which implies each takeoff consumes 3.8 J of energy.

Electrolysis reactions cannot achieve perfect efficiency due to over-potential. We can quantify the amount of energy spent by measuring current and integrating power

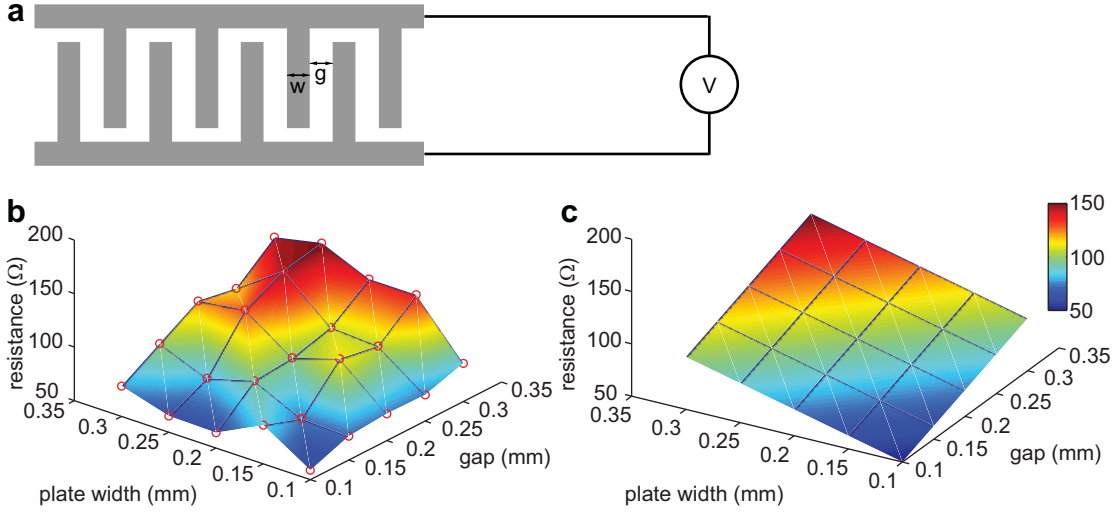


Figure 8.4: Plate geometry influence on water resistance during electrolysis. (a) Design of Interdigitated electrolytic plates. Plate finger width and gap are changed while the total plate area is kept constant. (b) Measurement of water resistance as a function of plate width and gap. Each red circle represents a data point. (c) modeling of water resistance as a function of plate width and gap. (b) and (c) have the same color scale.

expenditure over the reaction time:

$$E_{meas} = \int_0^T v(t)i(t)dt = V \cdot IT,$$

where V is the voltage input, I is the average current and T is the total reaction time. In this equation, the product IT is proportional to the number of disassociated electrons, which further relates to net gas volume. Hence, IT is a constant for any fixed chamber volume. This analysis suggests energy input is directly proportional to input voltage. The lower bound of input voltage is 1.23 V, which is the minimum reaction potential. While lowering electrolysis voltage improves efficiency, it reduces the average current and increases the total reaction time.

To reduce input voltage while maintaining average current, we reduce water re-

sistance by improving plate geometry [71]. Specifically, we fabricate 25 interdigitated electrolytic plates of varying plate finger width and gap (figure 8.4a). We vary the input voltage from 0 V to 10 V and measure the corresponding current for every device. Then we calculate the corresponding resistance through linear fitting. Figure 8.4b shows the measured resistance as a function of plate width and gap. We observe that resistance increases as plate finger width or gap increases.

Resistance is proportional to the distance an electron travels in water, which is equal to the sum of plate width and gap. Figure 8.4c shows a simple resistance model: $r = C(w + g)$. Here C is a fitted constant, w and g are plate finger width and gap, respectively. This model yields good qualitative agreement with our measurement. The most efficient plates have width and gap of 0.1 mm, and its measured resistance is 59 Ω .

Although plates with smaller width and gap are more efficient, they are harder to fabricate. We set both plate width and gap to 0.2 mm for takeoff experiments. The measured resistance of this device is 98 Ω , which is 66% larger than the most efficient plates. This design operates at 7.5 V and completely fills the gas collection chamber in 120 seconds. The total energy expenditure is 16 J, and the device efficiency is 23%. The energy density of lithium batteries is 1.8 J/mg, which implies that each takeoff will exhaust energy from approximately 10 mg of battery. The power consumption for robot hovering is 300 mW, which suggests that each water-air transition corresponds to an approximate flight time of 40-60 seconds.

8.2.5 Robot assembly

First, four 160 μm thick carbon fiber struts securely connect the two robot halves (figure 8.2b). Then four balance beams are inserted into the slots on connection pieces. Next, each buoyant outrigger is attached to a balance beam. Then the gas collection chamber is inserted between the robot halves (figure 8.2c). Finally, the sparker plate is installed to the bottom of the gas collection chamber.

8.3 Robot air-water transition

Surface tension imposes extreme difficulties on air-water transitions of mobile objects at the milligram scale. Whereas impact forces from large diving objects [37, 74, 92] can easily break the water surface, water entry of millimeter-scaled objects is difficult due to the dominance of surface tension. To quantify the surface tension effect on water entry, we mount the robot on a capacitive force sensor (Figure 8.5a). The robot is lowered into or pulled out of water at a constant speed of 0.2 mm/s. We conduct experiments using either soapy water or tap water and quantify the effects of the surfactant. In these experiments the robot weighs 175 mg. The dimension of its gas collection chamber and buoyant outriggers are 14 mm \times 6.9 mm \times 5.75 mm and 4 mm \times 3 mm \times 1 mm, respectively. Instead of coating the robot with surfactant, we put three to five drops of Joy Liquid Detergent in approximately 200 mL of tap water.

First, we lower a robot that is completely dry into soapy water and measure the corresponding forces (Figure 8.5b). The robot experiences an upward buoyant force

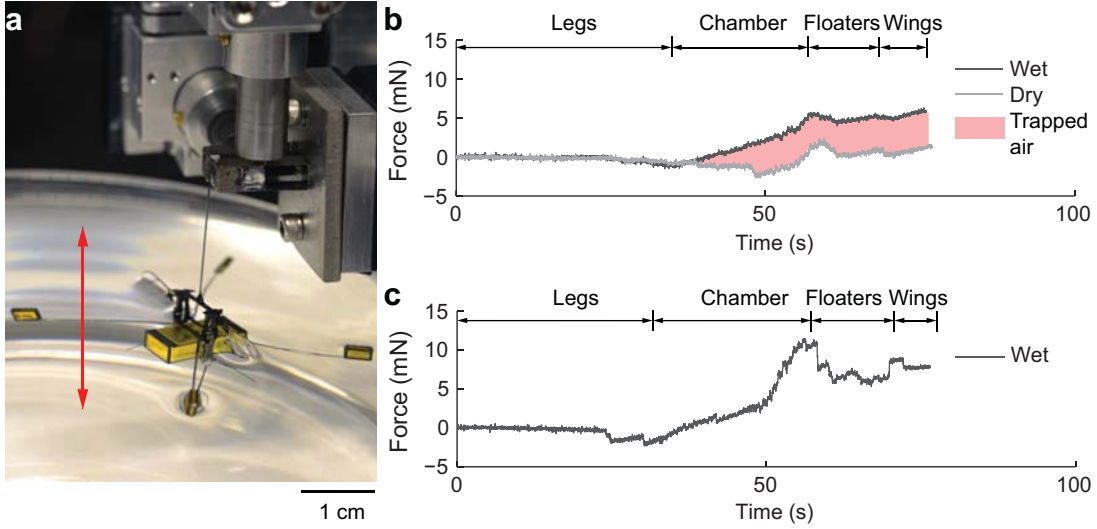


Figure 8.5: Surface tension measurement of robot air-water transition. (a) Illustration of the experimental setup. The robot is mounted on a capacitive force sensor and is slowly lowered into water or pulled out of water. (b) Force trace when the robot is lowered into soapy water. (c) Force trace as the robot is lowered into tap water.

as it is lowered into water. In addition, deformation of the water surface causes an upward surface tension force during water entry. The net buoyant force is given by the sum of contributions from the robot body, the sealed buoyant chambers, and the air trapped in the gas collection chamber:

$$F_{bouy} = F_{b,robot} + 4\rho_w g V_c + \rho_w g V_g. \quad (8.2)$$

In this equation, ρ_w is the water density, V_c is the small chamber volume, and V_g is the volume of trapped air. Without any trapped air ($V_g = 0$), the net buoyancy force is estimated to be approximately 1.1 mN. For the case of lowering a dry robot into soapy water, we measure the maximum force of 1.8 mN. The net force after the robot fully submerges is 1.3 mN, which implies 20 mm³ of air is trapped in the gas chamber or the robot body.

The experiment is repeated with a wetted robot (Figure 8.5b). Thin film of water covers the micro-openings and traps air during water entry. The maximum measured force is 6 mN, which implies 490 mm³ of air is trapped in the gas chamber or the robot body. The red colored region in Figure 8.5b shows the amount of captured gas due to covering of the micro-openings. Next, we lower a wetted robot into tap water and observe a significant increase in surface tension. The maximum force for tap water entry is 11 mN (Figure 8.5c). The net buoyancy force on trapped air, small buoyant outriggers, and the robot body sums to 7.6 mN, which implies surface tension is approximately 3.4 mN in tap water. These experiments suggest that the micro-openings and surfactant are necessary to enable water entry.

8.4 Robot water-air transition

To take off from the water surface, the robot must overcome surface tension and gravity while maintaining upright stability. Unlike large animals [73] or rotorcraft [68] that can demonstrate direct lift off, insects and microscale vehicles are limited by surface tension and gravity.

To achieve a water-air transition, our robot employs a two steps process: gradual surfacing of its wings followed by impulsive takeoff. As gas is generated and collected in the collection chamber, the gradually increasing buoyant force of the system gently pushes the robot's wings out of the water. In this process, surface tension on the balance beams maintains the robot's upright stability. This approach protects the delicate wings and transmission from high drag forces experienced upon impulsive transition to air. The second step generates an impulse that breaks the water surface.

Previously developed impulsive takeoff methods involve either a fast push off from the water surface [9, 57] or chemical reaction based jet propulsion [81]. Due to limited payload, our robot requires a novel method for repeatable takeoff. Here the robot utilizes reverse electrolysis to acquire energy for takeoff.

In the following sections, we quantify the surface tension forces on vehicle exit, investigate robot stability near the water surface, and demonstrate robot impulsive takeoff.

8.4.1 Surface tension force on an emerging robot

Using the same setup described in section 8.3, we measure the forces on the robot as it is pulled out of water. As the balance beams emerge from the water surface, a thin water film forms and stretches to the free surface (red circled region of figure 8.6a). This thin film collapses as the robot continues to rise, and consequently each balance beam pops out of water (figure 8.6b). This motion is captured by the discontinuities of the force plots (figure 8.6a-d). The magnitudes of these discontinuities quantify the surface tension forces on the balance beams and the chamber. In soapy water, the corresponding forces are 1.3 mN and 1.4 mN (figure 8.6c). We repeat the experiment in tap water (figure 8.6d) and measure 3.6 mN and 4.4 mN force on balance beam and chamber, respectively.

We model the surface tension forces using the formula [90] $F_s \approx 2\gamma L$, where γ is the surface tension coefficient and L is the wetted length. This equation assumes the floating object is a one dimensional thin wire. In soapy water, we estimate the surface tension forces on a balance beam and the chamber to be 1.2 mN and 2.0 mN,

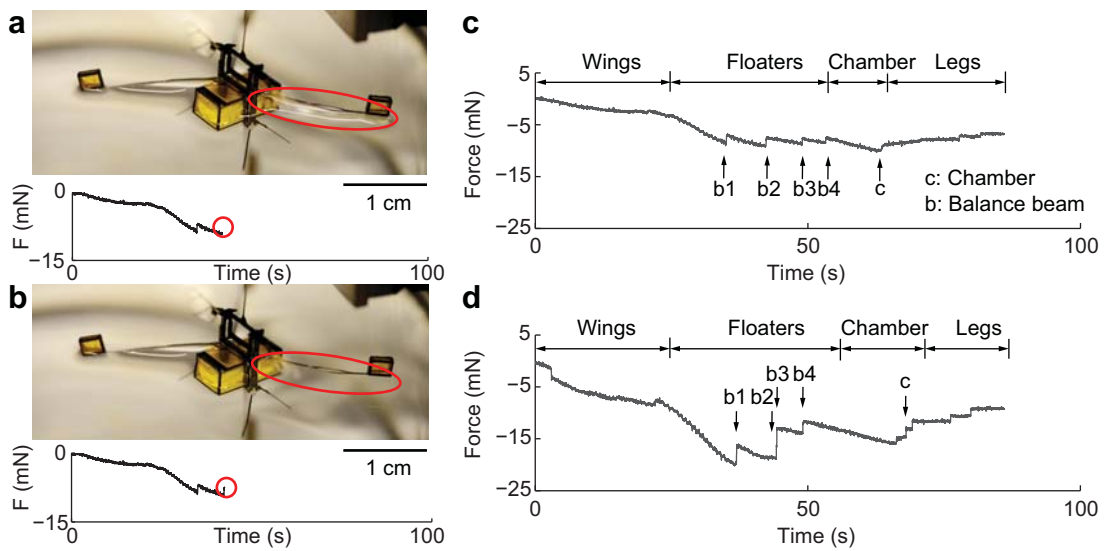


Figure 8.6: Surface tension measurement of robot water-air transition. (a) Picture of the robot and force trace immediately before one of its balance beams (red circle) pops out of the water surface. (b) Picture of the robot and force trace immediately after one of its balance beams (red circle) pops out of the water surface. (a) and (b) are taken 0.33 seconds apart. (c) Force trace as the robot is pulled out of soapy water. (d) Force trace as the robot is pulled out of tap water.

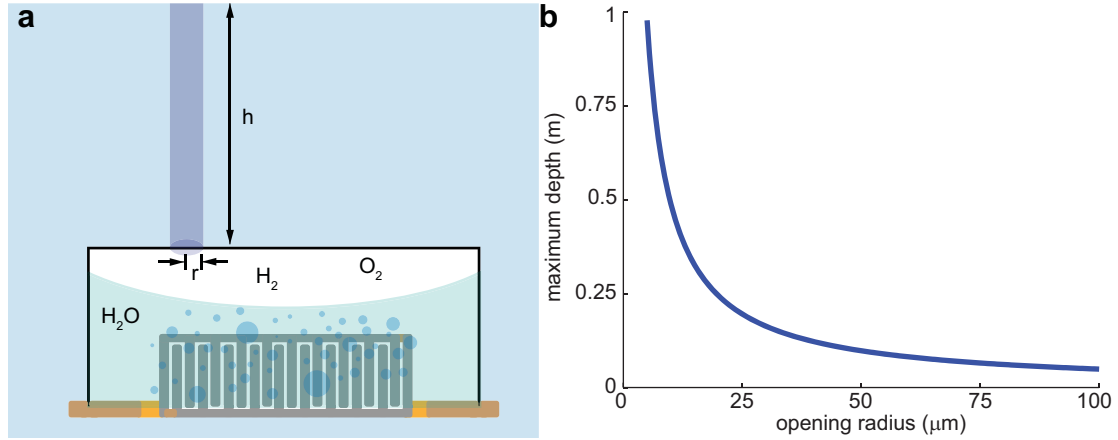


Figure 8.7: Surface tension influence on gas collection depth. (a) Illustration of gas collection in a chamber with openings on the top plate. The weight of a water column (dark blue) needs to be smaller than the surface tension force along the opening. Hydrogen and oxygen are captured in the chamber if current depth is smaller than the maximum depth. (b) Maximum gas collection depth as a function of micro-opening radius.

respectively. In tap water, the forces increase to 3.6 mN and 6.0 mN due to a larger γ . The estimates agree well with balance beam measurements, but over predict the force on the chamber. The discrepancy is largely contributed by the chamber corners because they do not satisfy the one dimensional assumption.

The robot has four balance beams and one gas collection chamber. In soapy water and tap water, the total surface forces on these components are 6.6 mN and 18.8 mN, respectively. This result suggests that direct liftoff from the water surface is infeasible, as a previous work [49] reports 3.1 mN maximum lift.

8.4.2 Underwater gas collection

Gas produced by the electrolysis reaction needs to be captured by the chamber. Although there are circular micro-openings on its top plate, the chamber can still

collect gas by utilizing surface tension effects (Figure 8.7a). To prevent water from flowing through the micro-openings, hydrostatic pressure needs to be balanced by capillary pressure. The hydrostatic pressure is linearly proportional to the distance from the water surface. Capillary pressure is calculated using the Young-Laplace equation, which relates pressure to the micro-opening radius and the material contact angle with water. We impose a force balance and obtain the following equation:

$$\rho_w h \pi r^2 = 2\pi \gamma \cos \theta_c, \quad (8.3)$$

where h is the distance from the water surface, r is the micro-opening radius, γ is the surface tension coefficient, and θ_C is the contact angle. We rearrange this equation and obtain a relation between depth h and micro-opening radius r :

$$h = \frac{2\gamma \cos \theta_C}{\rho_w g r}. \quad (8.4)$$

Figure 8.6b shows this relation for the current chamber design.

This relation offers guidelines for robot design and fabrication. We can interpret h as the maximum robot operation depth. The chamber cannot capture gas if the robot dives below depth h since gas will escape through the micro-openings. We can increase the maximum depth h by increasing the fluid surface tension coefficient, reducing the contact angle, or reducing the opening radius. In our experiment the aquarium height is 15 cm. Hence we set the opening radius to $34 \mu\text{m}$ to achieve 15 cm maximum depth.

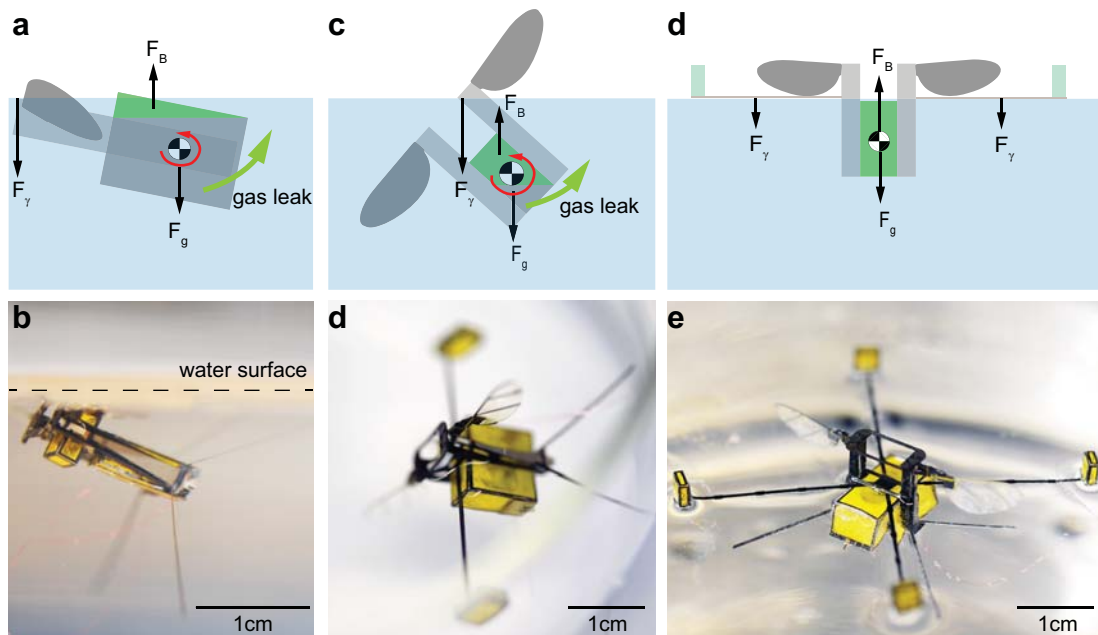


Figure 8.8: Robot stability near the water surface. (a) Illustration of the robot tilted along the body pitch axis beneath the water surface. (b) Picture of the robot tilted along the body pitch axis. (c) Illustration of the robot tilted along the body roll axis after it is stabilized in the pitching axis. (d) Picture of the robot tilted along the body roll axis at the water surface. (e) Illustration of a stabilized robot with balance beams. (f) Picture of the robot with its wings completely emerged from the water surface.

8.4.3 Robot stability near the water surface

The robot needs to maintain upright stability as its wings gradually emerge from water. If the robot body tilts significantly in this process, gas leaks via the chamber's uncovered bottom face and the buoyant force decreases.

Surface tension forces destabilize the robot along the body pitch and roll axes. (The definition of robot pitch, roll, and yaw axes is given in figure 7.2a.) Figure 8.7a illustrates body pitch instability in which the surface tension force creates a counter-clockwise torque. Gas leaks from the chamber's bottom face and the robot is unable to generate sufficient buoyancy force. Figure 8.7b shows an image from a related

experiment illustrating pitch instability. Pitch instability can be resolved by placing a balance beam along the roll axis.

The robot is also unstable along the roll axis due to similar surface tension effects (figure 8.7c). Here one robot wing pushes through the water surface but the other one remains fully submerged (figure 8.7d). We place balance beams in both pitch and roll axes to resolve pitch and roll instability. The surface tension force on the balance beams stabilizes the robot while the buoyancy force pushes both wings out of the water (figure 8.7e). Figure 8.7f shows successful wing water-air transition after installing balance beams.

8.4.4 Robot impulsive takeoff

The robot prepares for impulsive takeoff after its wings completely emerge from the water. At this time, the gas chamber is filled with oxyhydrogen that contains sufficient energy to break the water surface. The robot switches off its electrolytic plates and briefly flap its wings to remove water residue. Next, a 250 V pulsed signal (figure 8.9a) is sent to the sparker plate and corona discharge is generated within the 20 μm gap between the sparker plate electrodes. We find that the ignition energy is approximately 0.2 mJ by measuring the corresponding current and pulse duration (figure 8.9a). The detonation of oxyhydrogen [26] immediately increases pressure within the gas chamber (figure 8.9b). This detonation completes within 1 ms, breaks the water surface, and exerts an upward impulse on the robot. The average upward force generated within the first millisecond is between 7.5 N to 9 N, resulting in a device thrust-to-weight-ratio of 19,000 to 23,000.

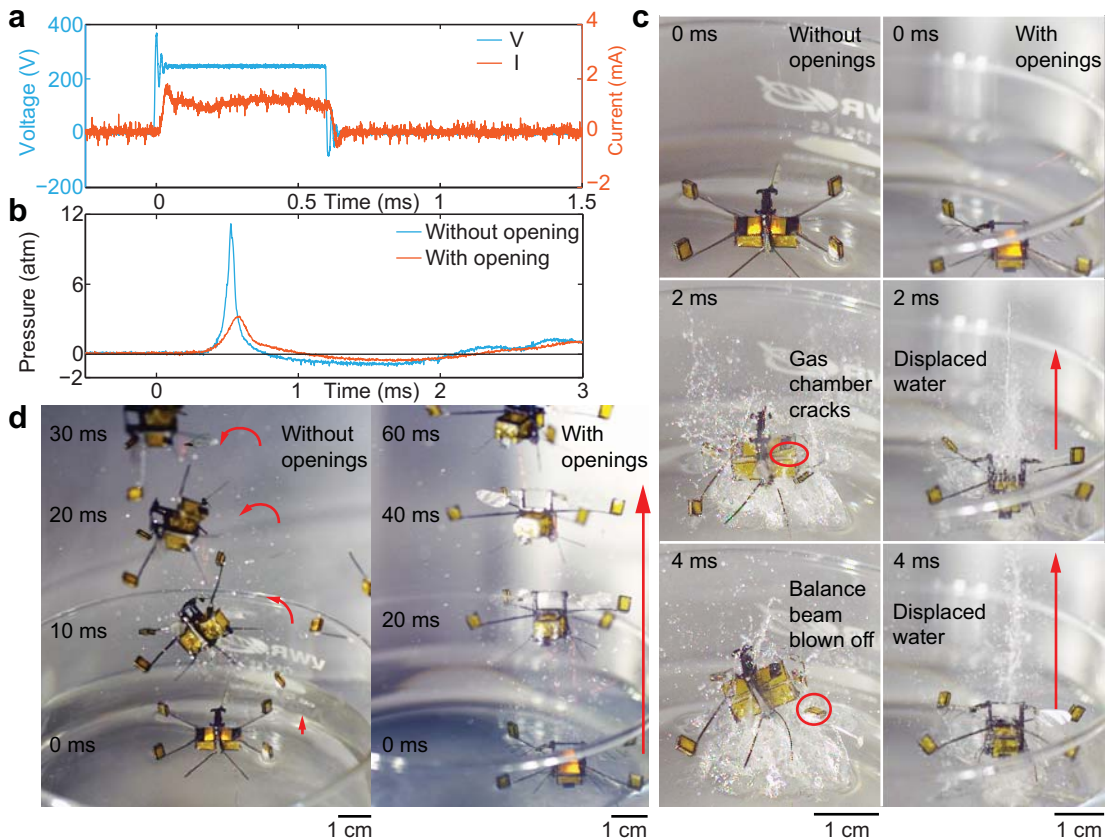


Figure 8.9: Impulsive takeoff from the water surface. (a) Sparker plate input voltage and current when a visible spark is generated. (b) Pressure profile within the chamber upon oxyhydrogen ignition. A reinforced chamber without micro-openings experiences higher pressure than one with micro-openings. (c) Image sequence comparison of initial robot takeoff. For the robot without chamber micro-openings (left), the detonation cracks the chamber top plate, and detaches a robot balance beam and wing. For the chamber with micro-openings (right), gas and water are released upon ignition and the robot remains undamaged. (d) Overlaid image comparison of robot takeoff. A robot without chamber micro-openings experiences significant body rotation and has a higher takeoff speed (left). A robot with chamber micro-openings maintains upright stability and has lower takeoff speed (right).

The micro-openings on the chamber top plate play important roles in preventing structural damage and improving takeoff stability. Without the micro-openings, excessive detonation pressure damages the chamber, balance beams, and robot wings (figure 8.9c). The robot takes off at 3.4 m/s and experiences large body rotation (figure 8.9d). In contrast, the presence of micro-openings reduces maximum pressure by 3.4 times and widens initial pressure pulse width by 39% (figure 8.9b), thereby preventing structural damage. The chamber with micro-openings experiences a smaller pressure rise (figure 8.9b) by releasing gas through its openings (figure 8.9c). These micro-openings further reduce the robot's takeoff speed and body rotation. With the micro-openings, the robot takes off at 1.8 m/s and the robot is undamaged. The balance beams stabilize robot takeoff via surface tension and viscous shear. Consequently, the robot experiences small body rotation during takeoff (figure 8.9d). In the next section, we investigate the influence of micro-openings on robot takeoff.

8.4.5 Effect of micro-openings on takeoff

Robot takeoff and landing experiments are conducted in a beaker of radius 7.5 cm (figure 8.10a). A pre-stretched nylon cloth is placed at the water level as the landing surface. We filmed the robot takeoff using a Phantom v7.10 color camera and a v7.3 black and white camera. The scene is illuminated by a VIC 900590P LED array. We use a Kistler 601B1 pressure sensor to measure the detonation pressure upon ignition.

Prior to conducting robot takeoff experiments, we design a set of simplified tests that replace robot halves with dummy weights. We further replace titanium balance beams with carbon fiber ones due to ease of fabrication. The device in figure 8.11

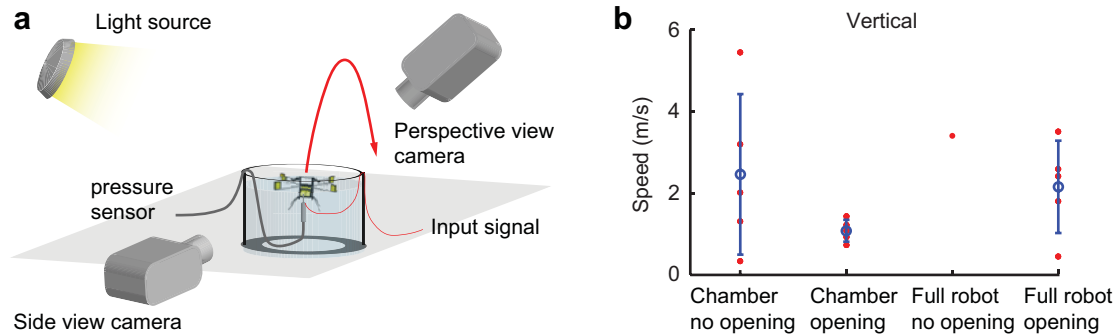


Figure 8.10: Impulsive takeoff experiment. (a) Experimental setup for takeoff and landing. (b) Chamber and robot vertical takeoff speed. We report five trials for chambers with or without openings and the robot with openings. We only report one trial for the robot without openings due to damage from explosion. The blue circles and lines represent mean and standard deviation.

weighs 170 mg and has an identical chamber as the real robot.

Figure 8.11a illustrates device takeoff without micro-openings. Large detonation pressures crack the chamber’s top plate and all balance beams break during takeoff. The vertical takeoff speed is 2.0 m/s. Figure 8.11b shows device takeoff with micro-openings. The vertical takeoff speed reduces to 1.4 m/s and the chamber is undamaged. Figure 8.11c shows a time image sequence of the same experiment during the early phase of takeoff. Water is ejected from the micro-openings within 0.5 ms of ignition. The openings release detonation energy and reduce takeoff speed.

We repeat the chamber explosion experiments five times. For the case of completely sealed chambers, there is noticeable damage in each experiment. In all five trials, the carbon fiber balance beams break in ways similar to the case shown in figure 8.11a. In two trials, the chamber’s side walls are blown apart during takeoff. In the rest of the experiments, we observe cracks and deformation on the chamber’s top plate and side walls. The sealed chambers cannot be reused after an explosion.

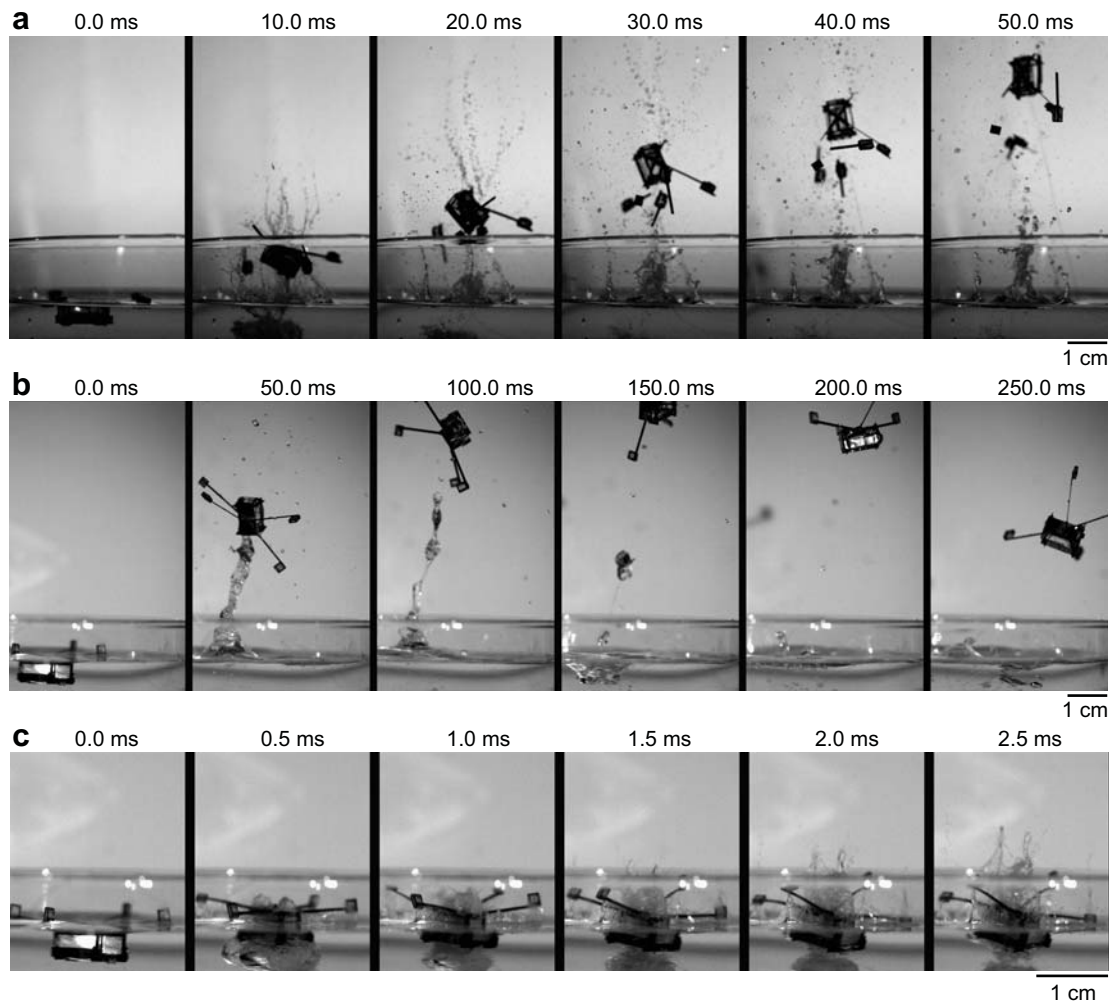


Figure 8.11: Influence of micro-openings on takeoff speed. (a) Takeoff of a chamber without micro-openings. The chamber cracks open and its supporting balance beams break apart. (b) Takeoff of a chamber with micro-openings. (c) Initial takeoff images of (b). Water exits the chamber through micro-openings before chamber gains momentum.

For the case of chambers with micro-openings, we observe significantly less damage. The chamber balance beams remain undamaged in three out of the five combustion experiments. The chamber is undamaged in four out of the five experiments. There is one experiment where the chamber is slightly damaged; there is a small crack on the chamber's side piece and the local epoxy sealant is removed by the explosion.

The first two columns of figure 8.10b compare the chamber's initial vertical takeoff speeds. The red dots show the takeoff speed of each individual experiment and the blue circles and lines show the mean and standard deviation. With the micro-openings, the chamber's mean vertical takeoff speed is reduced by 57%.

Next, we install chambers with micro-openings on a robot and perform five experiments. Here the balance beams are made of titanium T-beams. The robot remains undamaged in three out of the five trials. In one trial, the tabs of the titanium chamber top piece are detached from the side piece slots. The local epoxy sealant is removed by the explosion. In the other trial, one buoyant outrigger is blown away from the balance beam upon takeoff. In these two cases, the damage is minor and they can be easily repaired. Finally, we conduct one takeoff experiment using a robot with a sealed chamber. As described in the main text, the robot is severely damaged in the experiment. We do not repeat this experiment because robot and chamber fabrication is costly.

Figure 8.12 compares robot takeoff with and without chamber openings. Figure 8.12a, b show the side and perspective view for the case without micro-openings. The robot experiences large body rotation and its wings and balance beams are damaged. Figure 8.12c, d show the side and perspective view for the case with micro-

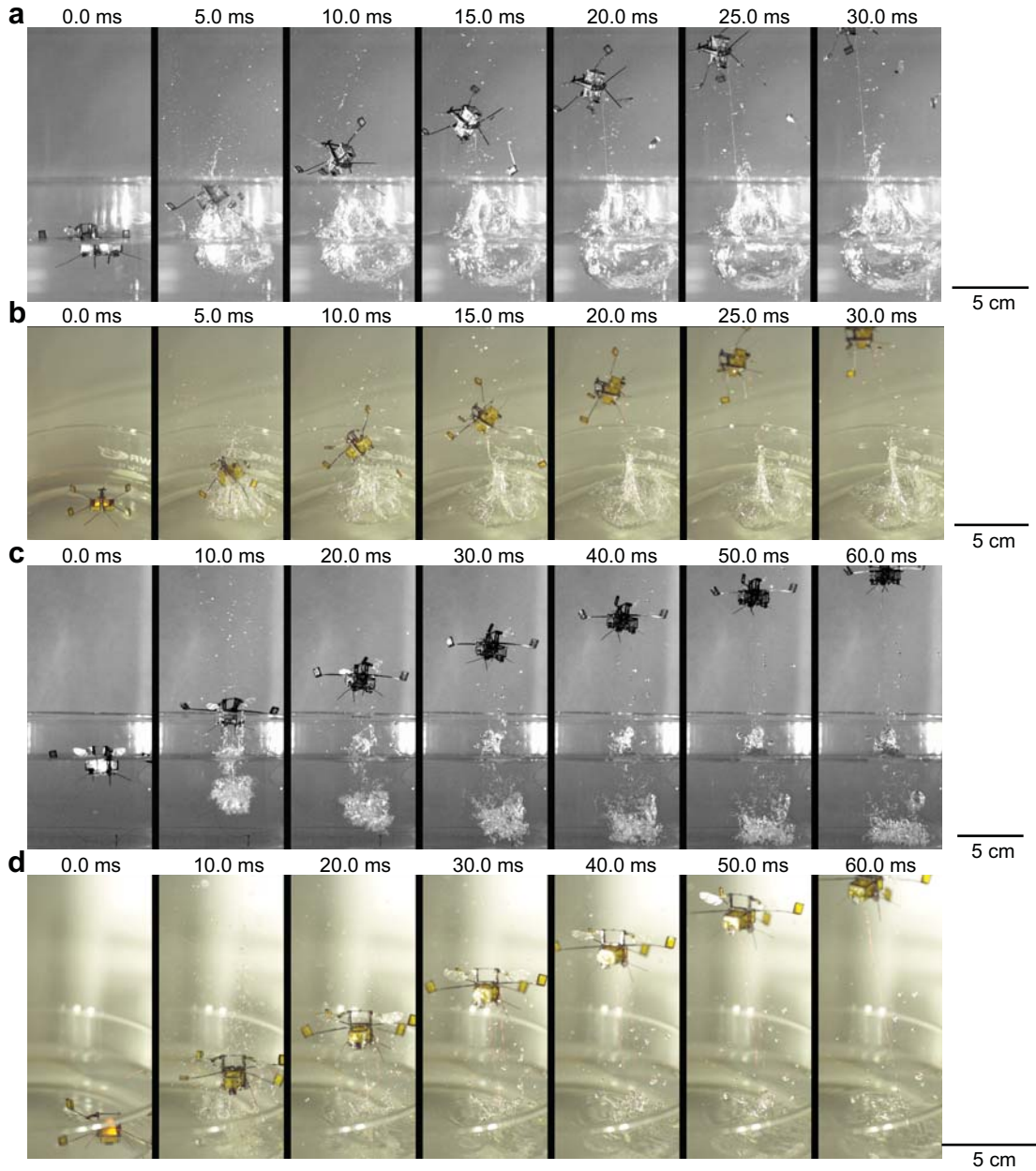


Figure 8.12: Robot impulsive takeoff. (a) Side view of robot takeoff. (b) Perspective view of robot takeoff. (a) and (b) show the same experiment in which the robot chamber is completely sealed. (c) Side view of robot takeoff. (d) Perspective view of robot takeoff. (c) and (d) show the same experiment in which the robot chamber has micro-openings to release detonation pressure.

openings. The robot is undamaged and experiences very small body rotation.

The last two columns of figure 8.10b compare the robot's initial takeoff speed. Compared to the case with a sealed chamber, the mean vertical speeds of the robot with chamber openings are reduced by 37%.

We further quantify the influence of micro-openings on detonation pressure. Unlike previous experiments, here we reinforce the sealed chamber with a 250 μm thick FR4 top plate so the chamber can survive the detonation. This extra reinforcement plate weighs 20 mg. We place a Kistler 601B1 pressure sensor beneath the robot chamber to measure pressure at the ignition location.

Figure 8.13a, b compare ignition pressure and takeoff velocity of robots with and without micro-openings. Measurements shown in Figure 8.13a, b resemble typical underwater explosion profiles in that a primary pressure peak is followed by an oscillatory tail [38]. Figure 8.13a, b show that the presence of micro-openings reduces the maximum pressure by 3.4 times and increases the initial pressure pulse width by 39%.

We observe that the robot without micro-openings has a significantly lower takeoff speed despite having a higher maximum pressure (red curves in Figure 8.13a, b). This observation differs from unreinforced explosion experiments in which the robot with a fully sealed chamber has a higher takeoff speed. In unreinforced explosion experiments, the detonation pressure cracks the fully sealed chamber and the cracks serve similar functions as the micro-openings.

Without cracks or micro-openings, the initial positive pressure pulse width decreases. Figure 8.13a, b mark four critical events along the pressure profile: ignition,

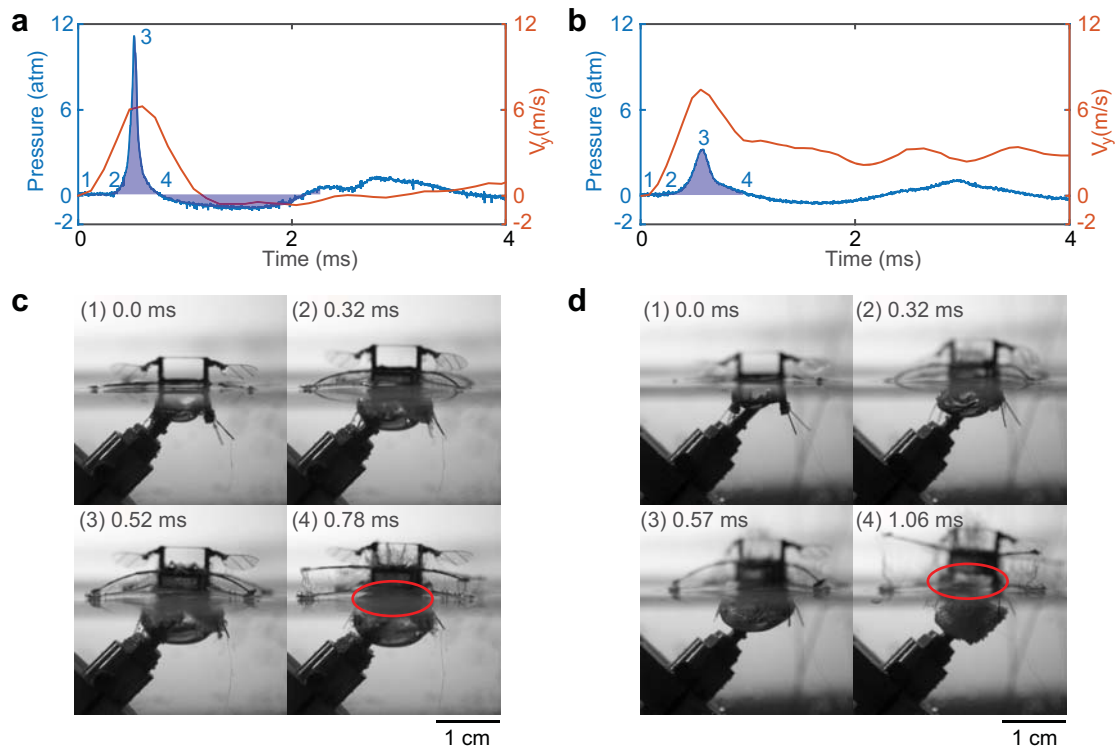


Figure 8.13: Influence of micro-openings on ignition pressure and takeoff speed. (a) Pressure distribution and takeoff velocity of a robot without micro-openings. The reinforced chamber survives the explosion. (b) Pressure distribution and takeoff velocity of a robot with micro-openings. Shaded regions in a and b represent the net impulse before the robot exits the water. Numeric labels in a and b indicate the times of ignition (1), start of pressure rise (2), peak pressure (3), and first transition to negative pressure (4). (c) Image sequence of robot takeoff corresponding to numeric labels in a. The red ellipse illustrates that the chamber has not exited the water surface when ignition pressure becomes negative. (d) Image sequence of robot takeoff corresponding to numeric labels in (b). The red ellipse illustrates that the chamber has exited the water surface when ignition pressure becomes negative.

start of pressure rise, pressure peak, and pressure drop. Figure 8.13c, d show the corresponding images of both experiments. The red circle in figure 8.13c shows that the chamber without micro-openings had not fully emerged from water surface when pressure fell negative. Consequently, the robot decelerates due to negative pressure caused by cavity contraction. In contrast, the red circle in figure 8.13d shows that the chamber with micro-openings completely exited the water surface before the pressure became negative. Consequently, cavity contraction has no effect on robot takeoff. In summary, the presence of micro-openings improves robot takeoff by reducing peak combustion pressure and increasing initial pressure pulse width.

We further relate robot takeoff velocity to the pressure measurements. We let m_r denote the robot mass, p_w denote the momentum of the displaced water, v_{exit} denote the robot velocity after the robot completely exits the water surface and t_{exit} denotes the corresponding time. The impulse-momentum equation gives:

$$m_r v_{exit} + p_w = \int_0^{t_{exit}} (F_{expl} + F_{visc} + F_{drag} + F_{surf} + F_g) dt, \quad (8.5)$$

where the total force is contributed by the explosion, viscous drag, pressure drag, surface tension, and the robot's weight. Each component is calculated as:

$$\begin{aligned} F_{expl} &= PA_t \\ F_{visc} &= -A_w \mu u \frac{1}{\sqrt{\pi vt}} \\ F_{drag} &= -\frac{1}{2} \rho C_D u ||u|| A_t \\ F_{surf} &= -2\gamma L \\ F_g &= -mg \end{aligned} \quad (8.6)$$

Symbol	Parameter name	Value
A_t	top plate area	94 mm ²
A_w	wetted area	180 mm ²
μ	water viscosity	1.002 mN·s/m ²
ν	water kinematic viscosity	1.004 mm ² /s
C_D	robot drag coefficient	1
γ	soapy water surface tension coefficient	24.3 mN/m
L	balance beam length	20 mm
m	robot mass	170 mg
g	gravitational acceleration	9.8 m/s ²

Table 8.1: Parameter values for forces estimation during impulsive takeoff.

Here P and u are instantaneous pressure and velocity. The values of other terms are documented in Table 8.1. By comparison, F_{expl} is on the order of several Newtons within the first millisecond and it dominates all other components so that the takeoff velocity can be approximated as:

$$v_{exit} \approx \frac{1}{m_r} \left(\int_0^{t_{exit}} F_{expl} dt - p_w \right). \quad (8.7)$$

Based on the high-speed videos, we estimate $t_{exit} = 1.1$ ms and 2.3 ms for the robot with or without chamber micro-openings, respectively. The corresponding robot takeoff velocities are 3 m/s and 1 m/s, respectively. Having measured other terms in the previous equation, we solve for the momentum of the displaced water. We estimate $p_w = 2$ mN s and 7 mN s for the case with or without micro-openings. In both cases the robot takeoff momentum is within 10% of the net impulse. This result shows that most of the impulse is absorbed by the water.

8.5 Landing and post-takeoff hovering

Due to motion tracking limitations, we cannot implement feedback control for impulsive water surface takeoff. Instead, the robot passively lands after takeoff (figure 8.1f). By extracting images from a high speed landing video, we measure maximum jump height and initial takeoff speed to be 37 cm and 2.5 m/s, respectively. Fig. 1f shows the composite image of the same experiment taken by a high speed camera at 9500 Hz. Although this zoomed in image does not track the entire trajectory, it shows that the robot maintains upright stability during landing.

The probability of successful landing is dependent on the landing surface. We drop the robot from 35 cm above different surfaces and repeat the experiment ten times. On pre-tensioned nylon cloth the bee successfully lands 60% of the time. The success rate is also 60% for stiff foam board. However, the success rate drops to 10% on stainless steel surfaces. These results show landing success rate is significantly higher on elastic surfaces. Pre-tensioned nylon cloth absorbs landing impact and there is very small landing bounce. The bounce magnitude significantly increases on stainless steel surfaces and reduces the landing success rate. This experiment suggests future robot designs may benefit from introducing compliance to the landing legs or from designs that passively orient the robot while on land.

To verify system repeatability, we demonstrate that the robot can successfully fly after impulsive takeoff and landing. The robot experiences none or small damage – cracked combustion chamber, loss of buoyant outrigger or landing legs, or broken wire in the power tether – after transitioning from water to land. Small damage occurs regularly during normal flight experiments, and these repairs can be performed

quickly. In addition, we strengthen the base of the robot with Loctite 416 after impulsive takeoff. The robot is first tested statically and demonstrates similar flapping performance. To achieve similar hovering performance, we perform additional wing hinge pairing, open-loop trimming, and closed-loop control parameter identification. Most importantly, we demonstrate that critical damage to the robot does not occur in any experiments (i.e. damage to the actuators, transmissions, or airframe) and the entire multimodal locomotion strategy can be performed repeatedly with a single robot.

In this chapter, we describe a hybrid aerial-aquatic, flapping wing microrobot. Besides demonstrating aerial and aquatic locomotion, we propose a novel takeoff method and develop lightweight multi-functional devices that generate large impulsive forces to overcome larger surface tension forces. The robot utilizes forward electrolytic reaction to push its wings out of the water surface and ignites the oxyhydrogen mixture to impulsively jump from the water surface. This transition method can be adapted to other aerial-aquatic vehicles, especially those with foldable wing designs and powered by chemical propellant. Further, this work offers a novel locomotive strategy for other microrobots in circumstances where surface forces impede robot movement. Finally, while this robot is an example of bioinspired engineering, it is also representative of capabilities that go beyond what nature can achieve. Although examples of insects that can perform a water-to-air transition exist, none can do so impulsively, largely due to the power density constraints on their musculoskeletal system and the dominance of surface tension at these scales.

Chapter 9

Conclusion

9.1 Summary

Inspired by agile natural flyers, we investigate the underlying physics of flapping flight, which enables similar functions in microrobots. In this dissertation, we report experimental and computational studies of flapping flight in aerial and aquatic environments. The major contributions of this work are as follows:

1. We develop a high-throughput experimental apparatus that enables efficient testing and analysis of wing and wing hinge performance. Our experiments show that wing inertia significantly impacts aerodynamic performance, wing hinge endurance strongly depends on hinge geometry, and wing hinge stiffness greatly influences passive wing pitching and lift force production.
2. We develop 2D and 3D numerical models that investigate the fluid mechanics of flapping flight. Our simulations quantify the relationship between flapping kinematics, induced flow structures, and force production. Specifically, we show

that stiffer wing hinges lead to advanced wing pitch rotation, which corresponds to a stronger leading edge vortex and thus larger lift force.

3. We propose a frequency scaling relationship that predicts flapping conditions in aquatic environments. By conducting numerical simulations and aquatic flapping experiments, we show that flapping flight with passive pitching can be adapted to both environments. This finding leads to the first ever demonstration of flapping wing locomotion in air and water.
4. We enable the RoboBee to transition from water to air by redesigning the vehicle's structure and developing novel impulsive mechanisms. At the millimeter scale, the dominance of surface tension effects gives rise to benefits and challenges unique to microrobots. We quantify the influences of surface tension and design micro-mechanical and electrical devices to either utilize or overcome these effects. This work results in the development of the first flapping wing, hybrid aerial-aquatic microrobot.

Our work sheds light on the understanding of insect flight and extends microrobot capabilities; however, there are many exciting topics for future exploration. In the following sections, we briefly describe future research directions in insect flight and microrobotics.

9.2 Fluid mechanical interactions between multiple wings

While our studies focus on the fluid mechanics of two-winged natural flyers such as honeybees or fruit flies, we have not investigated the forewing and hindwing interactions exhibited by dragonflies. As shown in a previous study [94], dragonflies modulate the phase between forewings and hindwings to save aerodynamic power or increase lift production. This phenomenon can be further studied using microrobotic flappers that have independent and precise control of relative phase and stroke amplitudes. With the goal of improving payload, maneuverability, and endurance, future studies can incorporate this new aerodynamic design into flapping wing vehicles.

9.3 Multiple winged designs and microrobotic modularity

Over the past decade, the RoboBee project has achieved a number of milestones including takeoff, hovering, perching, and swimming. Despite these advances, the current robot cannot carry the full suite of electronics necessary for autonomous flight due to limited the payload capacity of the robot. A previous study [66] successfully increased the payload by scaling up the robot's size. However, this scaling trend diminishes quickly due to the unfavorable weight-to-force scaling law intrinsic to piezoelectric actuators. To accommodate extra payload for flight autonomy, we propose an alternative robot design.

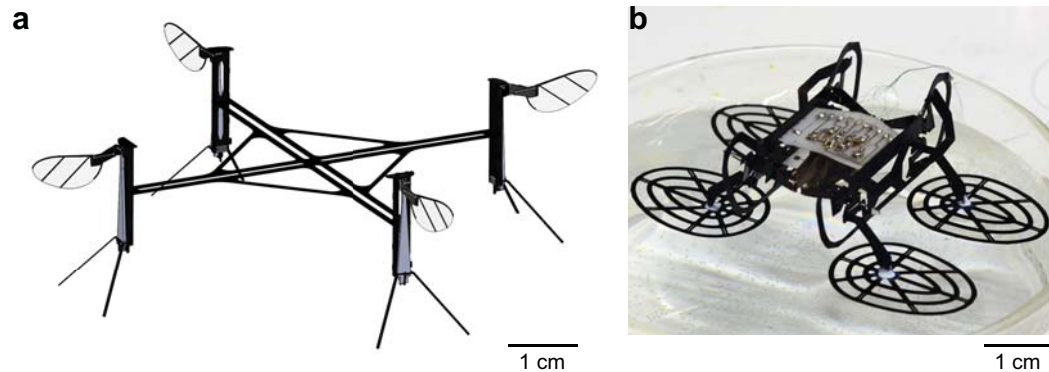


Figure 9.1: Future research directions of insect flight and microrobotics. (a) A conceptual drawing of a four-winged micro-flapper. (b) A Harvard Micro Ambulatory Robot (HAMR) resting on the water surface.

The current robot designs have two [65] or four [85] actuators and two independent control surfaces. As a consequence of the limited number of control surfaces, the robot must undergo frequent and tedious open and close loop trimming to maintain hover capability. To improve system payload and vehicle robustness, future studies can explore modularity in microrobotic design. Figure 9.1a shows a concept drawing of a quad-wing flyer consisting of four modular wing drivers. In this design, the vehicle can achieve a larger payload without experiencing the unfavorable actuator scaling. As the number of control surfaces increases, the robot's controllability increases. Consequently, the design is more tolerant to assembly imprecision and thus requires less calibration and repair. Furthermore, this design has improved stability because it allocates sufficient space for mounting sensors and batteries below the robot center of mass. Finally, this modular design is configurable because future studies can modify the number of wing drivers and their arrangements.

9.4 Novel microrobotic applications

Microrobots face unique challenges and opportunities at the millimeter scale. The dominance of surface forces gives rise to many potential applications (e.g. vertical climbing, perching) that are difficult for traditional robots. In addition to enabling multi-phase locomotion in a flapping wing robot, researchers can investigate other forms of multi-modal locomotion. Figure 9.1b shows a Harvard Micro Ambulatory Robot (HAMR) floating on the water surface. This preliminary work illustrates the possibility of hybrid terrestrial-aquatic locomotion. Enabled by folding-based meso-scale manufacturing techniques, future microrobots have the potential to achieve capabilities that surpass their biological counterparts and traditional robots.

9.5 Concluding remarks

Here we present experimental and computational studies of flapping flight. We quantify fluid-wing interactions and demonstrate the similarities of flapping propulsion in aerial and aquatic environments. Leveraging on micro-scale fabrication techniques, we develop the first flapping wing, hybrid aerial-aquatic microrobot. Future work on flapping wing vehicles can incorporate modular, multiple winged designs to improve payload capacity and aerodynamic efficiency. More broadly, future studies have the potential to enable novel microrobotic functionalities by exploiting surface effects.

Bibliography

- [1] Flying submarine, June 4 1963. US Patent 3,092,060.
- [2] Silas Alben and Michael Shelley. Coherent locomotion as an attracting state for a free flapping body. *Proceedings of the National Academy of Sciences of the United States of America*, 102(32):11163–11166, 2005.
- [3] John David Anderson Jr. *Fundamentals of aerodynamics*. Tata McGraw-Hill Education, 2010.
- [4] Federico Augugliaro, Ammar Mirjan, Fabio Gramazio, Matthias Kohler, and Raffaello D’Andrea. Building tensile structures with flying machines. In *Intelligent Robots and Systems (IROS), 2013 IEEE/RSJ International Conference on*, pages 3487–3492. IEEE, 2013.
- [5] Andrew T Baisch, Onur Ozcan, Benjamin Goldberg, Daniel Ithier, and Robert J Wood. High speed locomotion for a quadrupedal microrobot. *The International Journal of Robotics Research*, 33(8):1063–1082, 2014.
- [6] Attila J Bergou, Sheng Xu, and Z Jane Wang. Passive wing pitch reversal in insect flight. *Journal of Fluid Mechanics*, 591:321–337, 2007.

- [7] Paul Birkmeyer, Kevin Peterson, and Ronald S Fearing. Dash: A dynamic 16g hexapedal robot. In *Intelligent Robots and Systems, 2009. IROS 2009. IEEE/RSJ International Conference on*, pages 2683–2689. IEEE, 2009.
- [8] Frank M Bos, David Lentink, BW Van Oudheusden, and Hester Bijl. Influence of wing kinematics on aerodynamic performance in hovering insect flight. *Journal of fluid mechanics*, 594:341–368, 2008.
- [9] Malcolm Burrows. Jumping from the surface of water by the long-legged fly hydrophorus (diptera, dolichopodidae). *Journal of Experimental Biology*, 216(11):1973–1981, 2013.
- [10] Yufeng Chen, Nick Gravish, Alexis Lussier Desbiens, Ronit Malka, and Robert J Wood. Experimental and computational studies of the aerodynamic performance of a flapping and passively rotating insect wing. *Journal of Fluid Mechanics*, 791:1–33, 2016.
- [11] Yufeng Chen, E Farrell Helbling, Nick Gravish, Kevin Ma, and Robert J Wood. Hybrid aerial and aquatic locomotion in an at-scale robotic insect. In *Intelligent Robots and Systems (IROS), 2015 IEEE/RSJ International Conference on*, pages 331–338. IEEE, 2015.
- [12] Yufeng Chen, Kevin Ma, and Robert J Wood. Influence of wing morphological and inertial parameters on flapping flight performance. In *Intelligent Robots and Systems (IROS), 2016 IEEE/RSJ International Conference on*, pages 2329–2336. IEEE, 2016.

- [13] Bo Cheng, Jesse Roll, Yun Liu, Daniel R Troolin, and Xinyan Deng. Three-dimensional vortex wake structure of flapping wings in hovering flight. *Journal of The Royal Society Interface*, 11(91):20130984, 2014.
- [14] Pakpong Chirarattananon, Kevin Y Ma, and Robert J Wood. Adaptive control for takeoff, hovering, and landing of a robotic fly. In *Intelligent Robots and Systems (IROS), 2013 IEEE/RSJ International Conference on*, pages 3808–3815. IEEE, 2013.
- [15] Pakpong Chirarattananon, Kevin Y Ma, and Robert J Wood. Perching with a robotic insect using adaptive tracking control and iterative learning control. *The International Journal of Robotics Research*, 35(10):1185–1206, 2016.
- [16] Alexandre Joel Chorin. Numerical solution of the navier-stokes equations. *Mathematics of computation*, 22(104):745–762, 1968.
- [17] Timothy H Chung, Geoffrey A Hollinger, and Volkan Isler. Search and pursuit-evasion in mobile robotics. *Autonomous robots*, 31(4):299, 2011.
- [18] Alessandro Crespi and Auke Jan Ijspeert. Amphibot ii: An amphibious snake robot that crawls and swims using a central pattern generator. In *Proceedings of the 9th international conference on climbing and walking robots (CLAWAR 2006)*, number BIOROB-CONF-2006-001, pages 19–27, 2006.
- [19] John Davenport. How and why do flying fish fly? *Reviews in Fish Biology and Fisheries*, 4(2):184–214, 1994.
- [20] Ruijsink R Remes B De Wagter C De Croon GC, De Clercq KM. Design,

- aerodynamics, and vision-based control of the delfly. *International Journal of Micro Air Vehicles*, 1(2):71–97, 2009.
- [21] Alexis Lussier Desbiens, Yufeng Chen, and Robert J Wood. A wing characterization method for flapping-wing robotic insects. In *Intelligent Robots and Systems (IROS), 2013 IEEE/RSJ International Conference on*, pages 1367–1373. IEEE, 2013.
- [22] Michael H Dickinson. The initiation and control of rapid flight maneuvers in fruit flies. *Integrative and comparative biology*, 45(2):274–281, 2005.
- [23] Michael H Dickinson and Karl G Gotz. Unsteady aerodynamic performance of model wings at low reynolds numbers. *Journal of Experimental Biology*, 174(1):45–64, 1993.
- [24] Michael H Dickinson, Fritz-Olaf Lehmann, and Sanjay P Sane. Wing rotation and the aerodynamic basis of insect flight. *Science*, 284(5422):1954–1960, 1999.
- [25] William B Dickson, Andrew D Straw, and Michael H Dickinson. Integrative model of drosophila flight. *AIAA journal*, 46(9):2150–2164, 2008.
- [26] DH Edwards, GT Williams, and JC Breeze. Pressure and velocity measurements on detonation waves in hydrogen-oxygen mixtures. *Journal of fluid mechanics*, 6(04):497–517, 1959.
- [27] Charles P Ellington, Coen Van Den Berg, Alexander P Willmott, and Adrian LR Thomas. Leading-edge vortices in insect flight. *Nature*, 384(6610):626, 1996.

- [28] CP Ellington. The aerodynamics of hovering insect flight. i. the quasi-steady analysis. *Philosophical Transactions of the Royal Society of London B: Biological Sciences*, 305(1122):1–15, 1984.
- [29] CP Ellington. The aerodynamics of hovering insect flight. iii. kinematics. *Philosophical Transactions of the Royal Society of London B: Biological Sciences*, 305(1122):41–78, 1984.
- [30] R Eubank, E Atkins, and G Meadows. Unattended operation of an autonomous seaplane for persistent surface and airborne ocean monitoring. In *OCEANS 2010*, pages 1–8. IEEE, 2010.
- [31] Andrew Fabian, Yifei Feng, Erika Swartz, Derek Thurmer, and Rui Wang. Hybrid aerial underwater vehicle (mit lincoln lab). 2012.
- [32] Festo. Festo SmartBird inspired by nature, April 2011.
- [33] JR Fienup and AM Kowalczyk. Phase retrieval for a complex-valued object by using a low-resolution image. *JOSA A*, 7(3):450–458, 1990.
- [34] David F Fisher, John H DelFrate, and David M Richwine. In-flight flow visualization characteristics of the nasa f-18 high alpha research vehicle at high angles of attack. 1991.
- [35] Steven N Fry, Rosalyn Sayaman, and Michael H Dickinson. The aerodynamics of free-flight maneuvers in drosophila. *Science*, 300(5618):495–498, 2003.
- [36] Sawyer B Fuller, Michael Karpelson, Andrea Censi, Kevin Y Ma, and Robert J Wood. Controlling free flight of a robotic fly using an onboard vision sensor in-

- spired by insect ocelli. *Journal of The Royal Society Interface*, 11(97):20140281, 2014.
- [37] Stefan Garthe, Silvano Benvenuti, and William A Montecvecchi. Pursuit plunging by northern gannets (*sula bassana*)" feeding on capelin (*mallotus villosus*)". *Proceedings of the Royal Society of London B: Biological Sciences*, 267(1454):1717–1722, 2000.
- [38] Thomas L Geers and Kendall S Hunter. An integrated wave-effects model for an underwater explosion bubble. *The Journal of the Acoustical Society of America*, 111(4):1584–1601, 2002.
- [39] Christophe Geuzaine and Jean-François Remacle. Gmsh: A 3-d finite element mesh generator with built-in pre-and post-processing facilities. *International Journal for Numerical Methods in Engineering*, 79(11):1309–1331, 2009.
- [40] Vivette Girault and Pierre-Arnaud Raviart. *Finite element methods for Navier-Stokes equations: theory and algorithms*, volume 5. Springer Science & Business Media, 2012.
- [41] William Glaeser. *Materials for tribology*, volume 20. Elsevier, 1992.
- [42] MA Graule, P Chirarattananon, SB Fuller, NT Jafferis, KY Ma, M Spenko, R Kornbluh, and RJ Wood. Perching and takeoff of a robotic insect on overhangs using switchable electrostatic adhesion. *Science*, 352(6288):978–982, 2016.
- [43] Nick Gravish, Yufeng Chen, Stacey A Combes, and Robert J Wood. High-throughput study of flapping wing aerodynamics for biological and robotic ap-

- plications. In *Intelligent Robots and Systems (IROS 2014), 2014 IEEE/RSJ International Conference on*, pages 3397–3403. IEEE, 2014.
- [44] Emmanuel Guilmineau and P Queutey. A numerical simulation of vortex shedding from an oscillating circular cylinder. *Journal of Fluids and Structures*, 16(6):773–794, 2002.
- [45] Kun He, Wenqi Huang, and Yan Jin. An efficient deterministic heuristic for two-dimensional rectangular packing. *Computers & Operations Research*, 39(7):1355–1363, 2012.
- [46] Ronald D Henderson. Details of the drag curve near the onset of vortex shedding. *Physics of Fluids*, 7(9):2102–2104, 1995.
- [47] Jan S Hesthaven and Tim Warburton. *Nodal discontinuous Galerkin methods: algorithms, analysis, and applications*. Springer Science & Business Media, 2007.
- [48] Aaron M Hoover, Samuel Burden, Xiao-Yu Fu, S Shankar Sastry, and Ronald S Fearing. Bio-inspired design and dynamic maneuverability of a minimally actuated six-legged robot. In *Biomedical Robotics and Biomechanics (BioRob), 2010 3rd IEEE RAS and EMBS International Conference on*, pages 869–876. IEEE, 2010.
- [49] Noah T Jafferis, Moritz A Graule, and Robert J Wood. Non-linear resonance modeling and system design improvements for underactuated flapping-wing ve-

- hicles. In *Robotics and Automation (ICRA), 2016 IEEE International Conference on*, pages 3234–3241. IEEE, 2016.
- [50] K Jayaram, JM Mongeau, B McRae, and RJ Full. High-speed horizontal to vertical transitions in running cockroaches reveals a principle of robustness. In *Integrative and Comparative Biology*, volume 50, pages E83–E83. Oxford Univ Press Inc Journals Dept, 2001 Evans Rd, Cary, NC 27513 USA, 2010.
- [51] Martin Jensen. Biology and physics of locust flight. iii. the aerodynamics of locust flight. *Philosophical Transactions of the Royal Society B: Biological Sciences*, 239(667):511–552, 1956.
- [52] W Johnson, PD Soden, and ER Trueman. A study in jet propulsion: an analysis of the motion of the squid, *loligo vulgaris*. *J. exp. Biol*, 56:155–165, 1972.
- [53] DA Jones and DB Clarke. Simulation of the flow past a sphere using the fluent code. Technical report, 2008.
- [54] Chang-kwon Kang and Wei Shyy. Passive wing rotation in flexible flapping wing aerodynamics. In *30th AIAA Applied Aerodynamics Conference*, page 2763, 2012.
- [55] Matthew Keennon, Karl Klingebiel, Henry Won, and Alexander Andriukov. Development of the nano hummingbird: A tailless flapping wing micro air vehicle. In *AIAA Aerospace Sciences Meeting*, 2012.
- [56] John Kim and Parviz Moin. Application of a fractional-step method to incom-

- pressible navier-stokes equations. *Journal of computational physics*, 59(2):308–323, 1985.
- [57] Je-Sung Koh, Eunjin Yang, Gwang-Pil Jung, Sun-Pill Jung, Jae Hak Son, Sang-Im Lee, Piotr G Jablonski, Robert J Wood, Ho-Young Kim, and Kyu-Jin Cho. Jumping on water: Surface tension–dominated jumping of water striders and robotic insects. *Science*, 349(6247):517–521, 2015.
- [58] David Lentink and Michael H Dickinson. Rotational accelerations stabilize leading edge vortices on revolving fly wings. *Journal of Experimental Biology*, 212(16):2705–2719, 2009.
- [59] David Lentink, Stefan R Jongerius, and Nancy L Bradshaw. The scalable design of flapping micro-air vehicles inspired by insect flight. In *Flying insects and robots*, pages 185–205. Springer, 2009.
- [60] Bin Liang and Mao Sun. Nonlinear flight dynamics and stability of hovering model insects. *Journal of The Royal Society Interface*, 10(85):20130269, 2013.
- [61] Jianhong Liang, Xingbang Yang, Tianmiao Wang, Guocai Yao, and Wendi Zhao. Design and experiment of a bionic gannet for plunge-diving. *Journal of Bionic Engineering*, 10(3):282–291, 2013.
- [62] Yanpeng Liu and Mao Sun. Wing kinematics measurement and aerodynamics of hovering droneflies. *Journal of Experimental Biology*, 211(13):2014–2025, 2008.
- [63] Marco Locatelli and Ulrich Raber. Packing equal circles in a square: a determin-

- istic global optimization approach. *Discrete Applied Mathematics*, 122(1):139–166, 2002.
- [64] Richard J Lock, Ravi Vaidyanathan, Stuart C Burgess, and John Loveless. Development of a biologically inspired multi-modal wing model for aerial-aquatic robotic vehicles through empirical and numerical modelling of the common guillemot, *uria aalge*. *Bioinspiration & biomimetics*, 5(4):046001, 2010.
- [65] Kevin Y Ma, Pakpong Chirarattananon, Sawyer B Fuller, and Robert J Wood. Controlled flight of a biologically inspired, insect-scale robot. *Science*, 340(6132):603–607, 2013.
- [66] Kevin Y Ma, Chirarattananon Pakpong, and Robert J Wood. Design and fabrication of an insect-scale flying robot for control autonomy. In *Intelligent Robots and Systems (IROS), 2015 IEEE/RSJ International Conference on*, pages 1558–1564. IEEE, 2015.
- [67] Silvia Maciá, Michael P Robinson, Paul Craze, Robert Dalton, and James D Thomas. New observations on airborne jet propulsion (flight) in squid, with a review of previous reports. *Journal of molluscan studies*, 70(3):297–299, 2004.
- [68] Marco M Maia, Parth Soni, and Francisco J Diez. Demonstration of an aerial and submersible vehicle capable of flight and underwater navigation with seamless air-water transition. *arXiv preprint arXiv:1507.01932*, 2015.
- [69] David W Murphy, Deepak Adhikari, Donald R Webster, and Jeannette Yen.

- Underwater flight by the planktonic sea butterfly. *Journal of Experimental Biology*, 219(4):535–543, 2016.
- [70] Robin R Murphy, Eric Steimle, Chandler Griffin, Charlie Cullins, Mike Hall, and Kevin Pratt. Cooperative use of unmanned sea surface and micro aerial vehicles at hurricane wilma. *Journal of Field Robotics*, 25(3):164–180, 2008.
- [71] N Nagai, M Takeuchi, T Kimura, and T Oka. Existence of optimum space between electrodes on hydrogen production by water electrolysis. *International journal of hydrogen energy*, 28(1):35–41, 2003.
- [72] Toshiyuki Nakata and Hao Liu. Aerodynamic performance of a hovering hawkmoth with flexible wings: a computational approach. *Proceedings of the Royal Society of London B: Biological Sciences*, page rspb20111023, 2011.
- [73] Víctor Manuel Ortega-Jiménez, Saúl Álvarez-Borrego, Sarahí Arriaga-Ramírez, Martin Renner, and Eli S Bridge. Takeoff flight performance and plumage wettability in cassin’s auklet *ptychoramphus aleuticus*, xantus’s murrelet *synthliboramphus hypoleucus* and leach’s storm-petrel *oceanodroma leucorhoa*. *Journal of Ornithology*, 151(1):169, 2010.
- [74] Man-Sung Park, Young-Rae Jung, and Warn-Gyu Park. Numerical study of impact force and ricochet behavior of high speed water-entry bodies. *Computers & fluids*, 32(7):939–951, 2003.
- [75] Néstor O Pérez-Arancibia, Kevin Y Ma, Kevin C Galloway, Jack D Greenberg,

- and Robert J Wood. First controlled vertical flight of a biologically inspired microrobot. *Bioinspiration & Biomimetics*, 6(3):036009, 2011.
- [76] Per-Olof Persson and Gilbert Strang. A simple mesh generator in matlab. *SIAM review*, 46(2):329–345, 2004.
- [77] Ngoc San Ha, Quang Tri Truong, Nam Seo Goo, and Hoon Cheol Park. Relationship between wingbeat frequency and resonant frequency of the wing in insects. *Bioinspiration & biomimetics*, 8(4):046008, 2013.
- [78] Sanjay P Sane. The aerodynamics of insect flight. *Journal of experimental biology*, 206(23):4191–4208, 2003.
- [79] Sanjay P Sane and Michael H Dickinson. The control of flight force by a flapping wing: lift and drag production. *Journal of experimental biology*, 204(15):2607–2626, 2001.
- [80] Richard Shepherd Shevell. Fundamentals of flight. 1989.
- [81] R Siddall and M Kovač. Launching the aquamav: bioinspired design for aerial–aquatic robotic platforms. *Bioinspiration & biomimetics*, 9(3):031001, 2014.
- [82] Mark W Spong, Seth Hutchinson, and Mathukumalli Vidyasagar. *Robot modeling and control*, volume 3. wiley New York, 2006.
- [83] D Stojković, M Breuer, and F Durst. Effect of high rotation rates on the laminar flow around a circular cylinder. *Physics of fluids*, 14(9):3160–3178, 2002.
- [84] Roger Temam. *Navier-stokes equations*, volume 2. North-Holland Amsterdam, 1984.

- [85] Zhi Ern Teoh and Robert J Wood. A bioinspired approach to torque control in an insect-sized flapping-wing robot. In *Biomedical Robotics and Biomechanics (2014 5th IEEE RAS & EMBS International Conference on)*, pages 911–917. IEEE, 2014.
- [86] William Thielicke and Eize J Stamhuis. The influence of wing morphology on the three-dimensional flow patterns of a flapping wing at bird scale. *Journal of Fluid Mechanics*, 768:240–260, 2015.
- [87] Adrian LR Thomas, Graham K Taylor, Robert B Srygley, Robert L Nudds, and Richard J Bomphrey. Dragonfly flight: free-flight and tethered flow visualizations reveal a diverse array of unsteady lift-generating mechanisms, controlled primarily via angle of attack. *Journal of Experimental Biology*, 207(24):4299–4323, 2004.
- [88] Shuangzhang Tu, Shahrouz Aliabadi, et al. A slope limiting procedure in discontinuous galerkin finite element method for gasdynamics applications. *International Journal of Numerical Analysis and Modeling*, 2(2):163–178, 2005.
- [89] Alphan Ulusoy, Michael Marrazzo, and Calin Belta. Receding horizon control in dynamic environments from temporal logic specifications. In *Robotics: Science and Systems*, 2013.
- [90] Dominic Vella and Jie Li. The impulsive motion of a small cylinder at an interface. *Physics of Fluids*, 22(5):052104, 2010.

- [91] Jane Wang and Song Chang. Predicting fruit fly's sensing rate from insect flight simulations. In *APS Meeting Abstracts*, volume 1, page 17002, 2013.
- [92] TM Wang, XB Yang, JH Liang, GC Yao, and WD Zhao. Cfd based investigation on the impact acceleration when a gannet impacts with water during plunge diving. *Bioinspiration & biomimetics*, 8(3):036006, 2013.
- [93] Z Jane Wang, James M Birch, and Michael H Dickinson. Unsteady forces and flows in low reynolds number hovering flight: two-dimensional computations vs robotic wing experiments. *Journal of Experimental Biology*, 207(3):449–460, 2004.
- [94] Z Jane Wang and David Russell. Effect of forewing and hindwing interactions on aerodynamic forces and power in hovering dragonfly flight. *Physical review letters*, 99(14):148101, 2007.
- [95] JP Whitney, PS Sreetharan, KY Ma, and RJ Wood. Pop-up book mems. *Journal of Micromechanics and Microengineering*, 21(11):115021, 2011.
- [96] JP Whitney and RJ Wood. Aeromechanics of passive rotation in flapping flight. *Journal of Fluid Mechanics*, 660:197–220, 2010.
- [97] JP Whitney and RJ Wood. Conceptual design of flapping-wing micro air vehicles. *Bioinspiration & biomimetics*, 7(3):036001, 2012.
- [98] Christian E Willert and Morteza Gharib. Digital particle image velocimetry. *Experiments in fluids*, 10(4):181–193, 1991.

- [99] RJ Wood, S Avadhanula, R Sahai, E Steltz, and RS Fearing. Microrobot design using fiber reinforced composites. *Journal of Mechanical Design*, 130(5):052304, 2008.
- [100] Robert J Wood. The first takeoff of a biologically inspired at-scale robotic insect. *IEEE transactions on robotics*, 24(2):341–347, 2008.
- [101] KAN Yasuhiko, Yuzuru YAMADA, and Koji TSUYUKI. Swimming behavior of small diving beetles. *Journal of Advanced Science*, 18(1+ 2):46–49, 2006.
- [102] Jie Zhang, Nan-Sheng Liu, and Xi-Yun Lu. Locomotion of a passively flapping flat plate. *Journal of Fluid Mechanics*, 659:43–68, 2010.
- [103] Lingxiao Zheng, Tyson L Hedrick, and Rajat Mittal. A multi-fidelity modelling approach for evaluation and optimization of wing stroke aerodynamics in flapping flight. *Journal of Fluid Mechanics*, 721:118–154, 2013.

Appendix A

Robot wing fabrication

6.1 Background

A RoboBee wing is made of a carbon fiber structural frame and polyester membrane through the smart composite micro structure processes [99]. The fabrication requires three materials: $0^\circ - 45^\circ - 0^\circ$ carbon fiber laminates, polyester membrane and acrylic adhesive. The $0^\circ - 45^\circ - 0^\circ$ carbon fiber laminates ensure high stiffness along the leading edge and wing spar directions. The acrylic adhesive laminates polyester membrane to the carbon fiber frame. Each material is laser cut using different cutfiles and laminated together under heat and pressure. Once cured, the composite is laser cut again to release the wings. Here we discuss the design process and describe a design automation method.

Previous wing shape variation studies required manual generation in a professional CAD software. This process was both time consuming and inconsistent, since a human operator was in charge of hand determining fine details such as spar placement

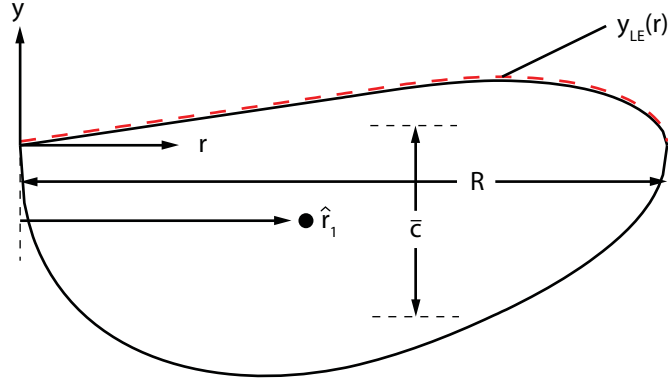


Figure A.1: Illustration of the wing planform and the morphological parameters. The red dotted line highlights the leading edge function $y_{LE}(r)$. R is the wing span, \bar{c} is the mean wing chord, and \hat{r}_1 is the non-dimensionalized first area moment. In this example, the values of R , \bar{c} , and \hat{r}_1 are 15 mm, 5 mm, and 0.49.

and fillet curves radii. The operator also tiled multiple wings within a rectangular template. This process became tedious and inefficient as number of wings increases. In the following sections we describe algorithms that automate the design and tiling processes.

6.2 Automated design of a single wing

We develop an algorithm that generates wing designs based on morphological parameter inputs. As discussed in Chapter 2, the wing planform is completely parametrized by a leading edge function $y_{LE}(r)$, wing span R , first moment \hat{r}_1 , and mean chord length \bar{c} . Figure A.1 illustrates an example wing planform and the corresponding morphological parameters. The algorithm computes wing planform based on user inputs, and then designs wing spars and hinges for structural support and assembly. Finally, it converts the final design into multiple laser cut files for fabrication.

Firstly, the wing planform is generated based on the parameters R , \hat{r}_1 , $LESR$, and \bar{c} . The wing leading edge profile $y_{LE}(r)$ is given by the equation:

$$y_{LE}(r) = LESR \cdot Y_{LE}(r), \quad (\text{A.1})$$

where $Y_{LE}(r)$ is a fixed function [96] and $LESR$ is the leading edge sweep ratio. The wing chord profile is given by:

$$c = \bar{c} \frac{\hat{r}^{p-1}(1-\hat{r})^{q-1}}{\int_0^1 \hat{r}^{p-1}(1-\hat{r})^{q-1} d\hat{r}}, \quad (\text{A.2})$$

where p and q are beta function parameters:

$$\begin{aligned} p &= \hat{r}_1 \left(\frac{\hat{r}_1(1-\hat{r}_1)}{\hat{r}_2^2 - \hat{r}_1^2} - 1 \right) \\ q &= (1 - \hat{r}_1) \left(\frac{\hat{r}_1(1-\hat{r}_1)}{\hat{r}_2^2 - \hat{r}_1^2} - 1 \right) \end{aligned} \quad (\text{A.3})$$

Given the input parameter \hat{r}_1 , we can compute wing second moment:

$$\hat{r}_2 = 0.929\hat{r}_1^{0.732}. \quad (\text{A.4})$$

Having obtained the wing chord function $c(r)$, we compute wing trailing edge profile:

$$y_{TE}(r) = y_{LE}(r) - c(r). \quad (\text{A.5})$$

These equations are adopted from Ellington's wing parametrization study [28].

The algorithm further designs wing structural and mating features. Firstly, the algorithm computes an offsetted inner contour based on user selection of spar thickness

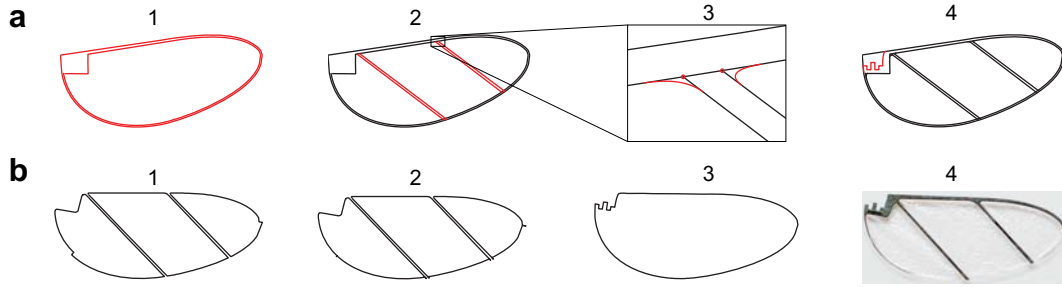


Figure A.2: Illustration of wing cut file generation. (a) Design processes of a single wing. After wing outer contour is generated based on morphological parameter inputs (a-1), wing spars are placed between leading and trailing edge (a-2). Next, stress relieving fillets (a-3) and mating feature (a-4) are added to the design. (b) Cut files for carbon fiber composite (b-1), acrylic adhesive (b-2), and final release (b-3). A sample wing designed by this algorithm is shown in (b-4).

(Figure A.2a-1). Next, two diagonal wing spars are placed between wing leading and trailing edges (Figure A.2a-2). These spars form 45° angle with respect to the wing leading edge to ensure alignment with the $0^\circ - 45^\circ - 0^\circ$ carbon fiber laminate. In addition, stress relieving fillet features are placed at wing spar locations (Figure A.2a-3). Finally, a mating feature is placed near the wing root for wing hinge attachment (Figure A.2a-4).

The completed design is further decomposed into three different laser cut files. Selected regions of carbon fiber (Figure A.2b-1) and acrylic adhesive (Figure A.2b-2) are removed before the lamination step. Compared to the carbon fiber cut pattern, the adhesive cut pattern is offsetted outward to account for material thermal expansion during the lamination process. The final release cut traces the wing outer contour (Figure A.2b-3). Figure A.2b-4 shows a photograph of a robot wing designed by this algorithm.

6.3 Automated tiling of multiple wings

The previous section introduce an algorithm for designing a single wing. Traditionally every wing design is manually arranged within a rectangular area for batch fabrication. Here we develop a stochastic algorithm that tiles multiple wings within a template.

6.3.1 Problem formulation

The 2D tiling problem can be formulated under the optimization framework. Given a list of objects s_i , we aim to choose the subset of objects whose total area is maximized. We further impose two constraints: no two objects overlap and each selected object must be placed within the template. Mathematically, this NP hard integer programming problem is described by:

$$\begin{aligned}
 & \operatorname{argmax} \sum_i z_i A_i \\
 & \text{s.t } s \cap s_j = \emptyset \forall i, j . \\
 & S_i \subset B \forall i
 \end{aligned} \tag{A.6}$$

We aim to solve for the selection indicator vector \mathbf{z} and centroid position \mathbf{x}_i for every selected object. A_i is the area of the i^{th} object and B is the bounding template.

Deterministic strip packing algorithms [45, 63] are popular methods for solving this problem. This type of algorithms first finds a rectangular bounding box for each object, and then ranks the objects with respect to height, width, or height to width ratio. Finally, the objects are selected and tiled sequentially. While these methods are computationally efficient, they are not robust for irregular objects. We aim to improve

robustness by searching for an approximate solution using stochastic methods.

6.3.1 Approximate potential and stochastic gradient descent

Our algorithm defines a tiling potential function and searches for a local minimum. This potential function is defined as the sum of a global quadratic potential and local gravitational ones:

$$U = \frac{1}{2}K \sum_i \mathbf{x}_i^T \mathbf{x}_i - G \sum_i \sum_{j \neq i} A_j \frac{1}{\|\mathbf{x}_j - \mathbf{x}_i\|}, \quad (\text{A.7})$$

where K and G are the spring and gravitational coefficients. The solver starts by randomly placing each item outside of the template and then iteratively minimize the objective function.

In every iteration each object is displaced sequentially in the direction of the local gradient:

$$D_i \propto F_i = -\nabla_i U = K \mathbf{x}_i + G \sum_{j \neq i} A_j \frac{\mathbf{x}_j - \mathbf{x}_i}{\|\mathbf{x}_j - \mathbf{x}_i\|_2^3}. \quad (\text{A.8})$$

As shown in figure A.3a, the spring and gravitational potentials dominate in different regimes. The spring potential gives a “long range” force because it has large gradient when objects are distant to the template center. In contrast, the gravitational potential gives a “short range” force because its gradient increases as two objects move close. A distant object is pulled toward the template by a long spring force (figure A.3b). Objects within the template pack densely due to local gravitational attraction (figure A.3c). Finally, every object performs biased random walk at the end of each iteration. This design allows objects to escape from local minima. This potential function is

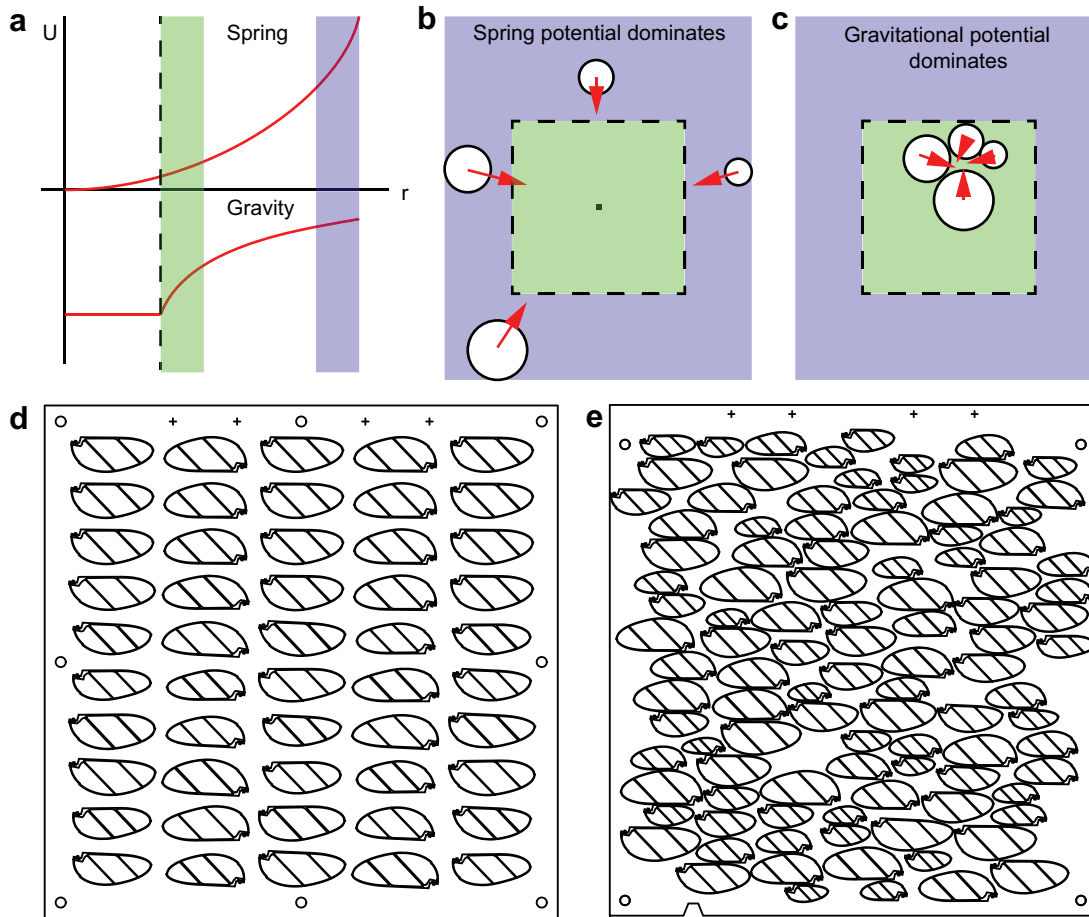


Figure A.3: Illustration of the potential function. (a) Spring potential on an object and gravitational potential between 2 objects. The dotted line indicates the position where two objects collide. (b) Spring potential dominates when objects are distant to the template and they are pulled toward the template center. (c) Gravitational potential dominates when objects within the template move close to each other. (d) Deterministic strip packing method tiles 50 wings of similar size. (e) The stochastic method tiles 102 wings of different sizes.

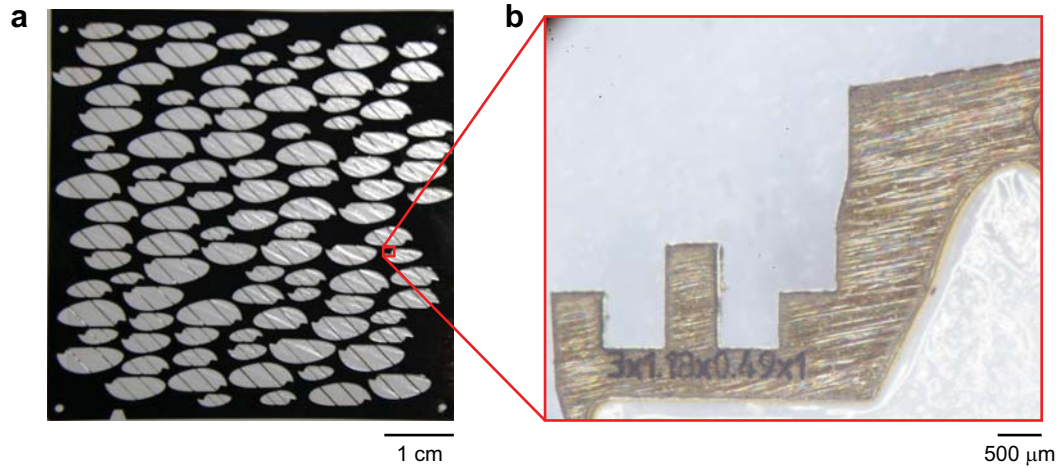


Figure A.4: Illustration of robot wing fabrication. (a) Fabrication of 102 different wings within one template. (b) Wing design parameters are labeled on the wing root.

computationally expensive because all objects interact with every other ones. Instead of accounting for every pairwise interaction, we approximate the function gradient by randomly sampling five neighbor objects.

Figure A.3d, e compare the tiling results of a deterministic algorithm and our proposed method. The deterministic method fits 50 wings and our methods fits 116 wings. In the example, our method further handles wings of varying size and morphology.

6.4 Fabrication demonstration

Our automated design and tiling algorithms significantly improve the fabrication efficiency. We demonstrate the fabrication of 102 different wing designs within a template (figure A.4a). To distinguish the wings, we engrave wing morphological parameters on each wing's mating feature (figure A.4b). This automated method

reduces total design time from over a hundred hours to within a few seconds. This improvement on design consistency and efficiency enables experimental optimization studies of wing morphology and inertia.

Appendix B

Validation of numerical solver

Here we validate our 2D and 3D numerical models by comparing with benchmark simulations in the literatures. To validate the 2D solver, we simulate flow over a cylinder for Reynolds numbers between 100 and 200. We report and compare the mean drag coefficient and Strouhal number with literature values. Figure B.1a shows the vorticity field of flow over a stationary cylinder. The Reynolds number is set to 150. To further validate the moving mesh implementation, we simulate flow over a rotating cylinder in figure B.1b and a vertically oscillating cylinder in figure B.1c. In the rotating cylinder simulation, we set $Re = 100$, $\omega L/2U_{ref} = 1$, where ω is the cylinder angular velocity, L is the cylinder diameter and U_{ref} is the upstream inflow velocity. In the oscillating cylinder simulation, we set $Re = 185$, $f_o/f_s = 0.8$, and $A/L = 0.2$, where f_o is the cylinder oscillation frequency, f_s is the vortex shedding frequency, and A/L is the oscillation amplitude to cylinder diameter ratio. These geometric and kinematic input parameters are documented in table B.1. Table B.1 further shows the relative error of these simulations compared with literature values.

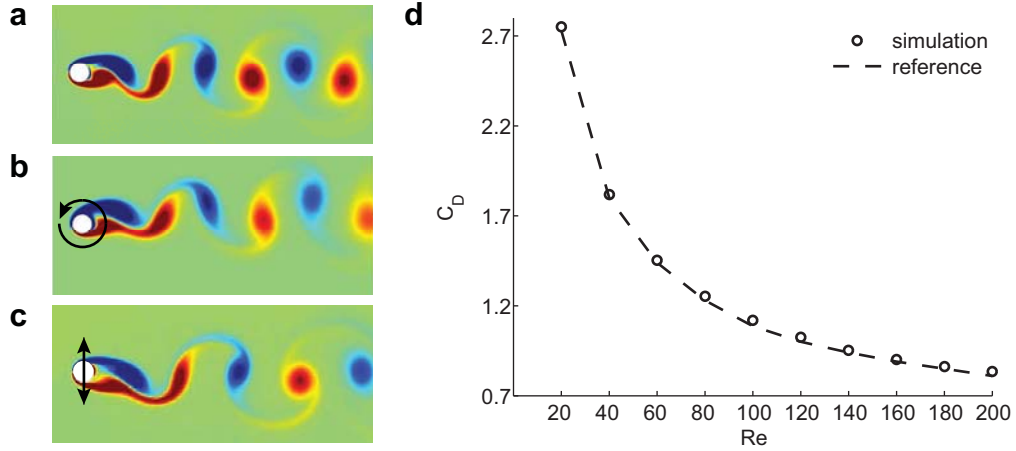


Figure B.1: Numerical solver validation. Two-dimensional vorticity fields of flow over a static (a), rotating (b) or vertically oscillating (c) cylinder. The corresponding mean drag coefficients and Strouhal numbers are compared with values reported in table B.1. (d) Three dimensional test cases of flow over a sphere. (d) Compares of mean drag coefficients of flow over a static sphere with values reported in Jones & Clarke [53]. The Reynolds number varies from 20 to 200 in steps of 20.

Test case	Re	$\omega L/2U_{ref}$	f_o/f_s	A/L	Ref	$\overline{C_{Dref}}$	$\overline{C_D}$	St_{ref}	St
Stationary	150	0	0	0	[46]	1.334	1.355	0.186	0.189
Rotating	100	1	0	0	[83]	1.108	1.143	0.166	0.170
Oscillating	185	0	0.8	0.2	[44]	1.200	1.239	N/A	0.194

Table B.1: Numerical test cases for flow over static, rotating or vertically oscillating cylinders. The mean drag coefficient and Strouhal number (St) are compared with numerical simulations documented in the literature.

We find that the relative error of our simulation result is within 3.25% for all 2D test cases.

To validate the 3D numerical solver, we simulate flow over a sphere for Reynolds numbers between 20 and 200 in steps of 20. The sphere has a diameter of 1. The upstream length, downstream length and radius of the cylindrical channel are 5, 15 and 5 respectively. Figure B.1d-f show the x , y , and z components of the flow field for the case of $Re = 200$. Figure B.1g compares our simulated mean drag coefficients

with the ones reported in Jones & Clarke [53]. In all test cases, our simulation results slightly overpredict mean drag coefficients by approximately 1.5%. We believe that this small error is due to a blockage effect (the ratio between sphere diameter and channel diameter) because our mesh dimensions are smaller than the mesh dimensions used in Jones & Clarke (2008).

We further show convergence of the 2D and 3D solvers. To avoid meshing discretization error and to reduce computational cost, we perform simulations in rectangular channel flow with non-slip boundary conditions. For the 2D simulation, the length and width of the channel are 20 and 4 respectively. The Reynolds number is 160. For the 3D simulation, the length, width and height of the rectangular channel are 20, 4 and 10 respectively. The Reynolds number is also 160.

Figure B.2 shows the convergence rate of the solver on log–log scales. The solver convergence rate can be approximated as the slope of the plots in figure B.2. Figure B.2a, b show that the 2D and 3D spatial convergence rates are 4.95 and 2.40. The 2D solver uses a fifth-order interpolation polynomial, hence it agrees with the expected convergence rate. The 3D solver uses a first-order interpolation polynomial but we observe second-order convergence. We observe a higher than expected convergence rate because this particular test case possesses geometric symmetry. (The flow field solution is symmetric in the plane orthogonal to the incoming flow.) Figure B.2c, d show that the 2D and 3D temporal convergences are 1.39 and 1.35 respectively. We observe that the convergence rate is slightly lower than expected because the Adams–Bashforth method is not self-starting at the first time step. Details of the Adams–Bashforth method are explained in Hesthaven & Warburton [47].

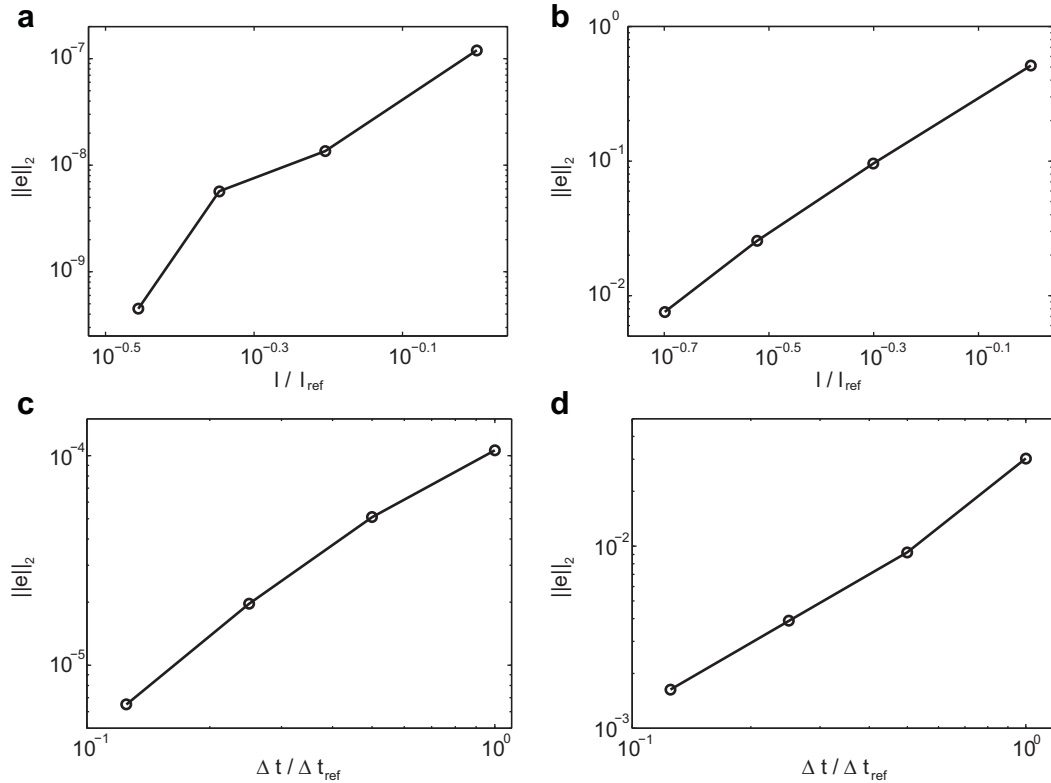


Figure B.2: The convergence rates of the 2D and 3D solvers. All graphs show the two norm relative errors as functions of mesh element length or time step size on log–log scales. (a) The spatial and (c) the temporal convergence rate of the 2D CFD solver. We simulate flow in a rectangular channel with non-slip boundary conditions. The Reynolds number is 160. It is shown in (a) that the spatial convergence rate is 4.95 and in (c) that the temporal convergence rate is 1.39. (b) The spatial and (d) the temporal convergence rate of the 3D solver. We simulate flow in a 3D rectangular channel with non-slip boundary conditions. The Reynolds number is 160. It is shown in (b) that the spatial convergence rate is 2.40 and in (d) that the temporal convergence rate is 1.35.